SIMULATION, ESTIMATION, AND EXPERIMENTATION OF VEHICLE LONGITUDINAL DYNAMICS THAT EFFECT FUEL ECONOMY

Except where reference is made to work of others, the work described in this thesis is my own or was done in collaboration with my advisory committee. This thesis does not include proprietary or classified information

Matthew Evan Heffernan

Certificate of Approval:

George T. Flowers Professor Mechanical Engineering	David M. Bevly, Chair Assistant Professor Mechanical Engineering
Thomas E. Burch Visiting Assistant Professor Mechanical Engineering	Stephen L. McFarland Dean Graduate School

SIMULATION, ESTIMATION, AND EXPERIMENTATION OF VEHICLE LONGITUDINAL DYNAMICS THAT EFFECT FUEL ECONOMY

Matthew Evan Heffernan

A Thesis

Submitted to

the Graduate Faculty of

Auburn University

in Partial Fulfillment of the

Requirements for the

Degree of

Masters of Science

Auburn, Alabama
August 7, 2006

SIMULATION, ESTIMATION, AND EXPERIMENTATION OF VEHICLE LONGITUDINAL DYNAMICS THAT EFFECT FUEL ECONOMY

Matthew Evan Heffernan

_____
Signature of the Author

_____
Date of Graduation

THESIS ABSTRACT

SIMULATION, ESTIMATION, AND EXPERIMENTATION OF VEHICLE LONGITUDINAL DYNAMICS THAT EFFECT FUEL ECONOMY

Matthew Evan Heffernan

Master of Science, August 7, 2006
(B.M.E., Auburn University, 2003)

144 Typed Pages

Directed by David M. Bevly

In this thesis, longitudinal vehicle dynamics are researched with an emphasis on heavy trucks and fuel economy. Commercial vehicles display large variations in their parameters, and due to many current trends in transportation systems, estimating these parameters has been the subject of much research. Additionally, fuel economy enhancement has become a major issue due to man-kind's reliance on oil. In this research a longitudinal truck model is developed and the longitudinal dynamics are simulated in various conditions. Algorithms are developed to estimate vehicle parameters and are used in simulation to perform an analysis of their accuracy. Simulated results show the difficulty of estimating individual vehicle parameters in the presence of sensor noise and low levels of vehicle excitation, such as with the heavy trucks at the Auburn University National Center for Asphalt Technology facility. Finally, a class 8 commercial vehicle is instrumented as a test-bed. Estimation results from the test bed support the simulation,

while simple parameters are shown to be identified with reasonable accuracy. Road load data for fuel economy evaluation was also collected on the trucks and variations over the asphalt sections are shown.

ACKNOWLEDGEMENTS

I would like to thank the National Center for Asphalt Technology for allowing me this research opportunity. Special thanks go to Buzz Powell, the NCAT test track manager, who has always been helpful and gone the extra mile for me. I'd also like to thank Dr. Ray Brown, the NCAT director, and Ronald and Margaret Kenyon for providing the support for this research.

Special thanks to my faulty advisor Dr. David Bevly for guiding me through this process and I thank you for the opportunity to further my education. Thanks to Dr. Tom Burch and Dr. George Flowers for serving on my advisory committee.

To all the folks in the GPS and Vehicle Dynamics Lab, thank you for the technical expertise, advice, and laughter. Special thanks to Rob Daily who has answered a ton of questions and given me a lot of help and knowledge in my years here.

I'd also like to thank Dr. Larry Benefield, Dean of Engineering, for such strong support of the engineering programs at Auburn University. Your efforts have enriched my education and experience at Auburn University.

Without love and support, my college career would not have been possible. I would like to thank my mother and father, Vickie and Alan Heffernan, and my entire family for constantly encouraging me. I love you all and dedicate this to you…

Style of Journal Used:

ASME Journal of Dynamic Systems, Measurement, and Control

Computer Software Used:

Microsoft Word 2003

TABLE OF CONTENTS

LIST OF FIGURES

LIST OF TABLES

CHAPTER 1

INTRODUCTION

1.1 Motivation

This research was first motivated by the National Center for Asphalt Technology (NCAT), at Auburn University. The test facility operates a trucking fleet, whose main goal is to perform accelerated asphalt wear experiments. The test bed includes a 1.7 mile oval test track located in Opelika, Alabama, on which 5 trucks drive the track approximately 16 hours per day, over a two year test period. During the inaugural construction of the NCAT pavement test track, fuel consumption of the trucks was measured as the two year period elapsed. A decrease in fuel consumption was seen as the asphalt degraded, as shown in Figure 1.1. This sparked an interested in studying the effect of asphalt on fuel economy.

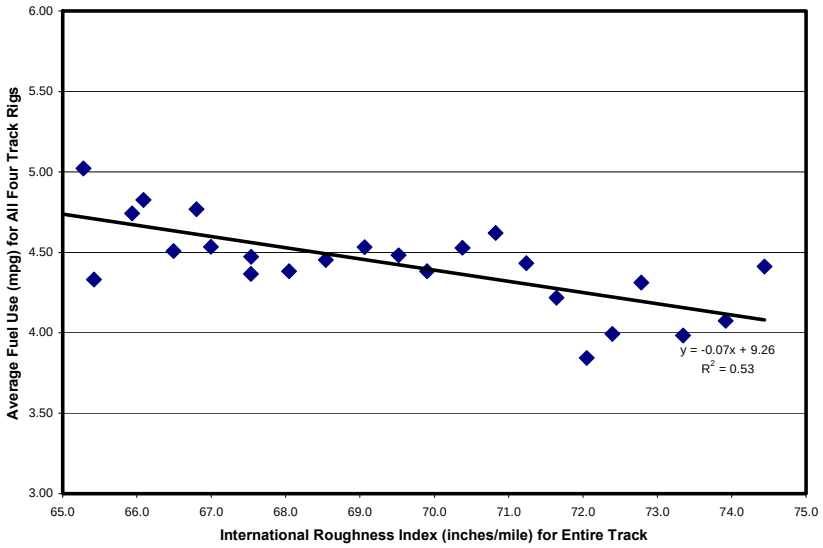

Figure 1.1. NCAT Fuel Economy Vs. Pavement Roughness (Courtesy Buzz Powell @NCAT)

During the 1970's and 1980's, fuel economy research took much priority due to widespread oil and fuel shortages. Today, emphasis is again being put on researching measures to reduce man-kind's overall consumption of oil products and make use of alternative fuels. Vehicle researchers and manufacturers strive to increase efficiency and develop new technologies to reduce fuel consumption in vehicles, especially heavy highway transport vehicles. Approximately 28% of the energy consumed today is in the transportation sector, where heavy trucks consume approximately 15 to 20% of the nation's highway fuel usage [EIA, 2004]. This represents a significant amount of energy and there is the potential to have a dramatic effect on the nation's fuel usage by even small improvements.

Much of this research to improve vehicle fuel economy is based around improving the tires rolling efficiency, or rolling resistance which, along with many other facets of vehicle research, is purely based on improving the vehicle. The motivation for

this thesis however, is to determine the effect of pavement types and construction to improve efficiency. This study was performed using the heavy trucks as a test bed to analyze the asphalt's influence on fuel consumption. This opportunity provides a unique experimental test environment as it involves measuring the truck's vehicle dynamics to develop information about the longitudinal dynamics and losses.

1.2 Back Ground and Literature Review

Many factors effect fuel economy, such as engine efficiency, rolling resistance, air drag, and friction from various components. Much research has studied the reduction of these effects as they all promise increases in vehicle efficiency and corresponding increases in fuel economy. Because the interest for this research is relating the road to fuel economy, the direct connection to vehicle performance is through reductions in rolling resistance.

Research has been produced to both measure and simulate rolling resistance coefficients and fuel economy effects. It has been shown that experimental tests can give rolling resistance coefficients that match laboratory tests by using corrections derived from fuel economy measurements [Knight, 1982]. The force applied to overcome rolling resistance losses comes from the engine which thereby affects the fuel consumption behavior of the powertrain. Studies have developed a relation between fuel economy and rolling resistance values and were validated with various road experiments [Schuring, 1982]. Other long term studies have been performed on heavy trucks to capture the

engine and drive cycle behaviors for simulating the long term fuel economy benefits of reducing rolling resistance of heavy truck tires [LaClair, 2005].

Much research has been done on tire behavior and the mechanisms that contribute to rolling resistance and the modeling of those effects. Tire parameters that effect rolling resistance behavior have been accurately quantified and used to predict their effect on fuel economy [Glemming, 1975; Knight 1979]. More complex tire models have been developed to analyze the heat generation in a rolling tire with the intention of simulating tire temperatures and temperature gradients [Song, 1999]. Models have also been developed to include new parameters such as expanding the Society of Automotive Engineers (SAE) mathematical specification for rolling resistance forces [Grover, 1999], or including tire velocity transients and tire temperature effects into the rolling resistance coefficient [Nielsen, 2002].

The majority of rolling resistance research is focused on examining and improving the tire for the benefit of fuel economy. The motivation for this research however, is to discover a relationship between the asphalt and fuel economy by examining the asphalts effect on rolling resistance. Research has provided conclusive results showing that asphalt indeed has a realizable impact on vehicle fuel consumption. Experiments using coast down tests on various road surfaces show that even with a simple energy based engine model, road surface had up to a 20% effect on fuel consumption [duPlessis, 1990]. Similar research using coast down experiments shows an 18% effect in fuel economy between the best and worst case surfaces tested [Bester, 1984]. Other research utilized a towed implement to measure rolling resistance forces and showed very distinct trends of increasing rolling resistance with increases in surface

texture and roughness of both micro and macro-texture. Rolling resistance coefficients in that research showed variations of 38%, which would yield fuel economy variations of 9% [Descornet, 1990].

The available research studying the effect asphalt has on rolling resistance and fuel economy is somewhat limited compared to that of tire behavior research. Most research tests only limited numbers of asphalt types that have large variations their properties. The NCAT facility is an opportune test facility to do such research due to the controlled environment and forty-five varieties of asphalts on the track. The fuel economy research in this thesis had to be unobtrusive to the current pavement testing. This necessitates different techniques for studying rolling resistance and required the use of the moving truck as the measurement test bed. The research, therefore, investigated the estimation of rolling resistance and truck longitudinal force as the trucks are driving, a technique new to studying fuel economy and rolling resistance.

Due the constraints on the test bed, the project becomes heavily reliant on the understanding of longitudinal vehicle dynamics and the ability to perform parameter estimation. Accurately identifying parameters such as vehicle mass, longitudinal losses, and road information, such as road grade and road friction, has been shown to provide useful information for systems such as intelligent cruise control, automated vehicle platooning, and advanced stability control systems for commercial vehicles [Bae, 2000; Bae, 2001; Bevly, 2000; Anderson, 2004; Peterson, 1998]. Therefore, this research uses such techniques, which have been shown capable for other systems, to perform road load, fuel economy, and rolling resistance studies.

1.3 Purpose of Thesis and Contribution

The purpose of this thesis to provide a fundamental background and understanding of vehicle longitudinal dynamics with the intent on using such knowledge to perform fuel economy studies. Such a study relies on the understanding of the vehicle's behavior, the vehicle's longitudinal losses, and estimation techniques suitable for identifying parameter variations effected by varying rolling losses.

This thesis presents two longitudinal vehicle dynamic models and evaluates these models for accuracy in an original simulation. The results are used to investigate the various losses and fuel economy effects that would be experienced in various dynamic conditions. This model is validated against commercial software and also used with a sensor simulation to simulate expected signals. The model is then used to perform sensitivity analysis on an estimation model to predict estimation errors as a function of sensor noise. A data acquisition system was constructed for use on the vehicles at NCAT and other vehicle dynamics testing. Data taken on the system was used to perform real world estimation schemes and provide results for the fuel economy/road load research.

1.4 Outline of Thesis

This thesis begins by presenting an overview of vehicle longitudinal dynamics with emphasis on the longitudinal losses such as rolling resistance and air drag. The effects are then numerically simulated in a longitudinal model. Chapter 3 presents a more advanced vehicle model that includes the effects of inertial losses on the vehicle. Various simulations are performed where the vehicle is accelerating, decelerating, and driving the

NCAT track. Variations in longitudinal load around the track are examined by simulating asphalts that would theoretically have varying levels of rolling resistance.

After the fundamentals and analyses of the vehicle's longitudinal dynamics are laid out, Chapter 4 presents a background on parameter estimation and sets out to perform such estimations in simulation. Various vehicle parameters are estimated and an in depth treatment of sensor noise is performed. Chapter 5 continues with parameter estimation results which are performed on the real world test-bed at the NCAT facility. Finally, overall conclusions and recommendations are provided in Chapter 6. Additionally, an overview of the vehicle properties, data acquisition system, and a discussion of the cruise control system can be found in the Appendices.

CHAPTER 2

VEHICLE MODEL

2.1 Introduction

In this chapter a longitudinal model of a rolling vehicle is developed to provide an introduction to longitudinal vehicle dynamics. This model is used to describe longitudinal dynamics of vehicle and contains the most significant longitudinal losses that affect the vehicle. These losses are then mathematically and physically described in detail to outline the mechanisms involved in each loss. Simulations are provided to show the magnitude of each loss and their power requirements and how they affect overall vehicle efficiency and fuel economy. Finally simulations are performed on the longitudinal model to show vehicle motion.

2.2 Longitudinal Model

To describe the longitudinal motion of a vehicle, the dynamics are derived from the loads on the vehicle, from which position, velocity, and acceleration of the vehicle can be determined. Longitudinal vehicle dynamics typically include many losses such as rolling resistance, air drag, and road grade or slope as shown. The developed model has

one degree of freedom and was derived using the equations of motion for the free body diagram shown in Figure 2.1.

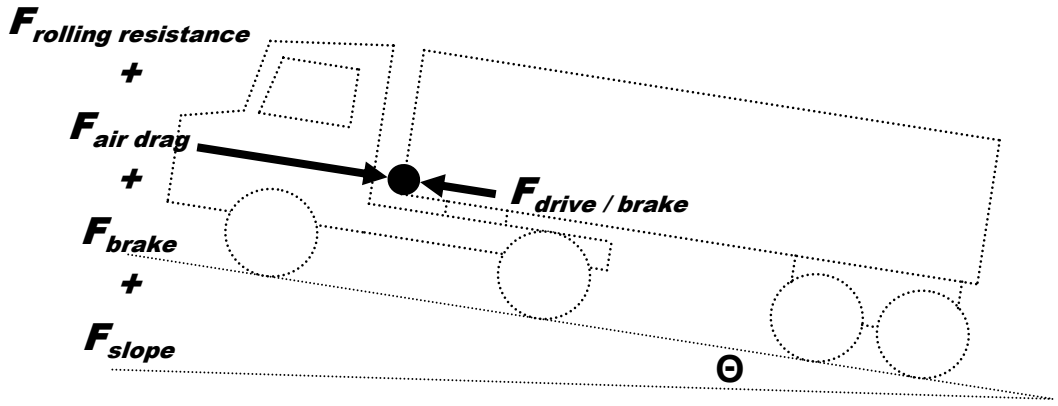

Figure 2.1. Longitudinal FBD

The governing equation of motion is derived from Newtonian dynamics and is shown in Equation 2.1.

$$\sum F = F_{Drive} - F_{Brake} - F_{Slope} - F_{Rolling\,Resistance} - F_{AirDrag} = m\ddot{x} \qquad 2.1$$

where:

F_{Drive} = Drive force provided by engine

F_{Brake} = Vehicle braking force

F_{Slope} = Longitudinal force due to road grade

$F_{Rolling\,Resistance}$ = Rolling resistance force

$F_{AirDrag}$ = Force due to air drag

m = Vehicle mass

$\ddot{x}$ = Longitudinal Acceleration

This model is widely accepted as a standard longitudinal vehicle dynamics model for modeling losses and vehicle drive behavior and is used for simulating vehicles in the longitudinal vehicle coordinate frame [Gillespie, 1992].

2.3 Loss Components

The major losses of the moving vehicle are air drag, rolling resistance, and road grade or slope. The following equations (2.1 through 2.5) mathematically describe each of these components.

$$\mathrm{F}_{\text{Air Drag}} = \frac{1}{2}\rho_{air} C_d A_{fr} V^2 = C_{df} V^2 \tag{2.2}$$

$$\mathrm{F}_{\text{Slope}} = mg\sin\phi \tag{2.3}$$

$$\mathrm{F}_{\text{Rolling Resistance}} = C_{rr} mg \tag{2.4}$$

$$\mathrm{F}_{\text{engine}} = \frac{\tau_{\text{engine}} \mathrm{N}_{\text{transmission}} \mathrm{N}_{\text{final drive}} \varepsilon_{\text{mechanical}}}{R_{tire}} \tag{2.5}$$

where:

ρ_{air} = Air density

C_d = Aerodynamic drag coefficient

A_{fr} = Vehicle frontal area

V = Vehicle speed

C_{df} = Vehicle air drag coefficient

C_{rr} = Rolling resistance coefficient

g = Gravity

τ_{engine} = Engine torque

$\text{N}_{\text{transmission}}$ = Transmission reduction ratio

$\text{N}_{\text{final drive}}$ = Final gear reduction ratio

$\varepsilon_{\text{mechanical}}$ = Overall mechanical efficiency

R_{tire} = Rear tire radius

2.3.1 Air Drag

Air drag force arises from two sources, form drag and viscous friction, which result from fluid flow around the vehicle. Air drag forces are quite significant in long haul truck and trailers due to their high frontal areas and poor aerodynamics [Wood, 2003]. Air drag is a function of the vehicle's velocity squared which is due to the dynamic pressure, or form drag, shown in Equation 2.6.

$$P_{dynamic} = \frac{1}{2}\rho_{air}V^2 \qquad 2.6$$

This dynamic pressure, multiplied by the vehicle aerodynamic drag coefficient and frontal area, yields an aerodynamic drag force, as shown previously in Equation 2.2. For convenience, air drag force on a specific vehicle is often simplified to an air drag coefficient, which is the vehicle's drag coefficient standardized with frontal area and

fluid properties. This results in a coefficient that can be used to easily compare the aerodynamic efficiencies of different vehicles.

Power can be described as energy per time or force times distance per time. Equations 2.7 and 2.8 describe the power consumed for a give force in the longitudinal dynamics.

$$Energy = Force * dist \tag{2.7}$$

$$Power = \frac{energy}{time} = (Force)(V) \tag{2.8}$$

Figure 2.2 shows a calculated road load of air drag for a constant vehicle mass and frontal area as a function of vehicle speed and air drag coefficient. The plot shows the non-linear velocity relationship and the significant power that can be necessary to overcome air drag forces in a vehicle such as a class 8 truck.

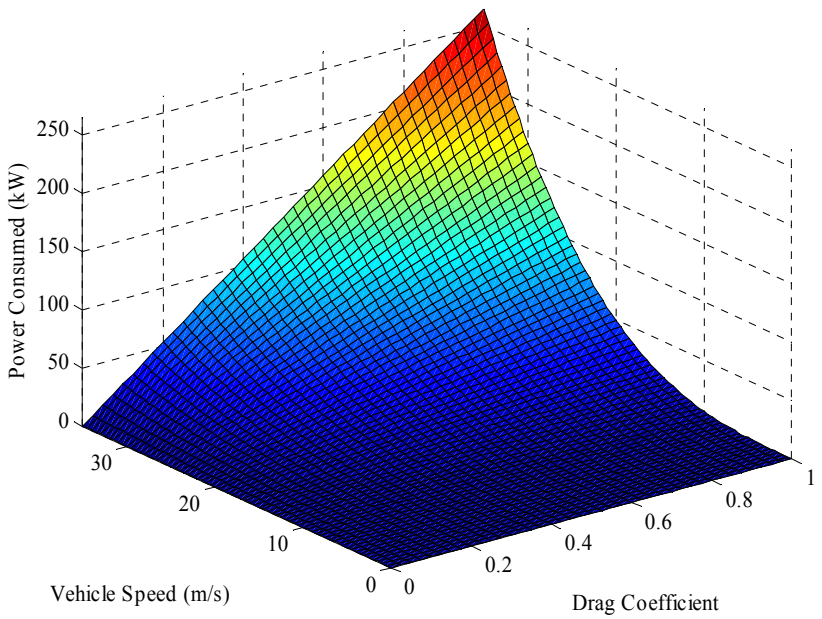

Figure 2.2. Model of Power Losses Involved In Air Drag

2.3.2 Road Grade

Road grade contributes to the longitudinal dynamics by adding a component of the vehicle mass (on which gravity acts) in the longitudinal direction. These forces can be significant especially in heavy vehicles such as long haul trucks. The force from road grade is proportional to the vehicle mass and the sine of the road angle, as expressed previously in Equation 2.3. Figure 2.3 shows the magnitude of the power consumed driving over different road grades at various speeds for a constant vehicle mass of 68,000kg.

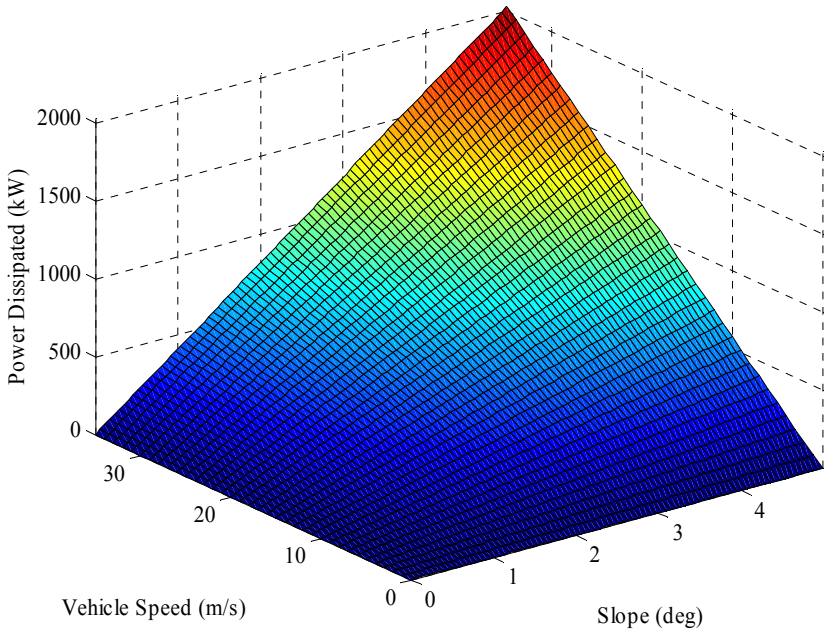

Figure 2.3. Model of Power Losses Involved In Road Grade

2.3.3 Rolling Resistance

Rolling resistance losses occur due to phenomenon of a rolling tire and comes from many different sources of losses within the tire. Rolling resistance is of primary concern due to its direct effect on vehicle longitudinal losses, and is the primary effect roads have on fuel consumption. Much research has been done on rolling resistance as a function of tire properties and asphalt composition as described in Section 1.2. An understanding of rolling resistance can be obtained by examining the free body diagram of the free rolling tire is shown in Figure 2.4.

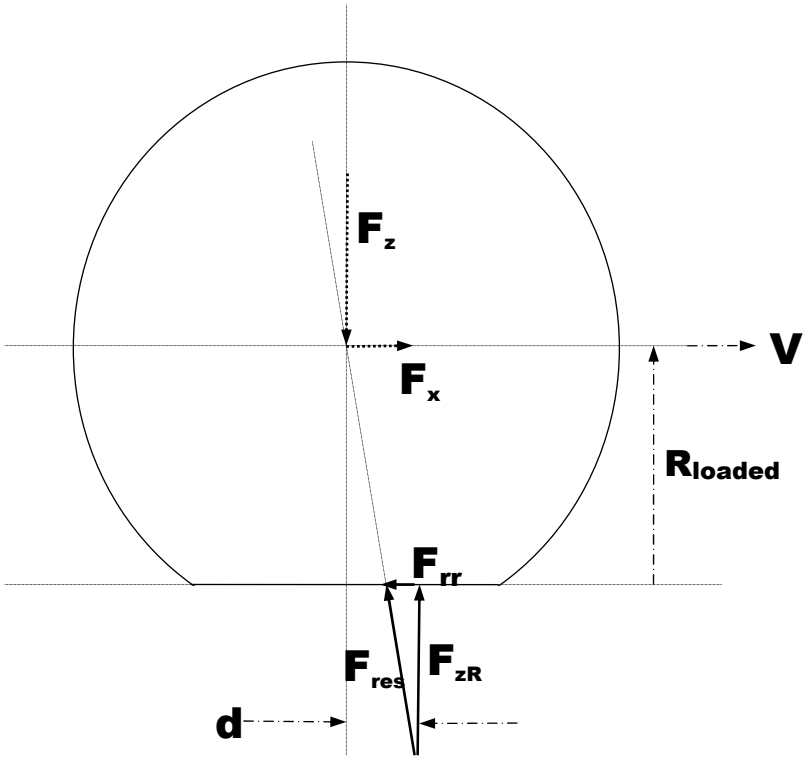

Figure 2.4. Rolling Tire FBD

where:

F_z = Normal force or weight

F_{rr} = Rolling resistance force

F_{res} = Reaction force of road

d = Distance to centroid of contact pressure

F_x = Force of tow

F_{zr} = Reaction of normal force

V = Velocity

R_{loaded} = Loaded tire radius

The free body diagram is representative of a free rolling tire, defined as "one that is towed (or pushed) straight ahead in an upright position with all applied moments (internal and external) about the wheel spin axis to be nearly zero and longitudinal wheel slip to be negligible" [Gillespie, 1992]. Because the center of pressure of the tire's contact patch is forward of the wheel centerline, a phenomenon of a rolling tire, the rolling resistance force and normal force also act in front of the wheel's centerline. This creates a resultant force that points to the center line of the wheel, with both horizontal and vertical components. The horizontal component of the force denoted Fx, is the rolling resistance fore that is required to tow the wheel due to rolling resistance losses.

It is important to note that different variations of this free body diagram can be shown where rolling resistance is a pure couple about the wheels centerline as a product of the force, Fz and distance, d. This would indicate that the rolling resistance couple increases linearly with either an increase in Fz, or vehicle weight, mg. Figure 2.5 shows a calculation of power losses due to rolling resistance as a function of vehicle mass and speed, where the rolling resistance force is increased linearly with mass.

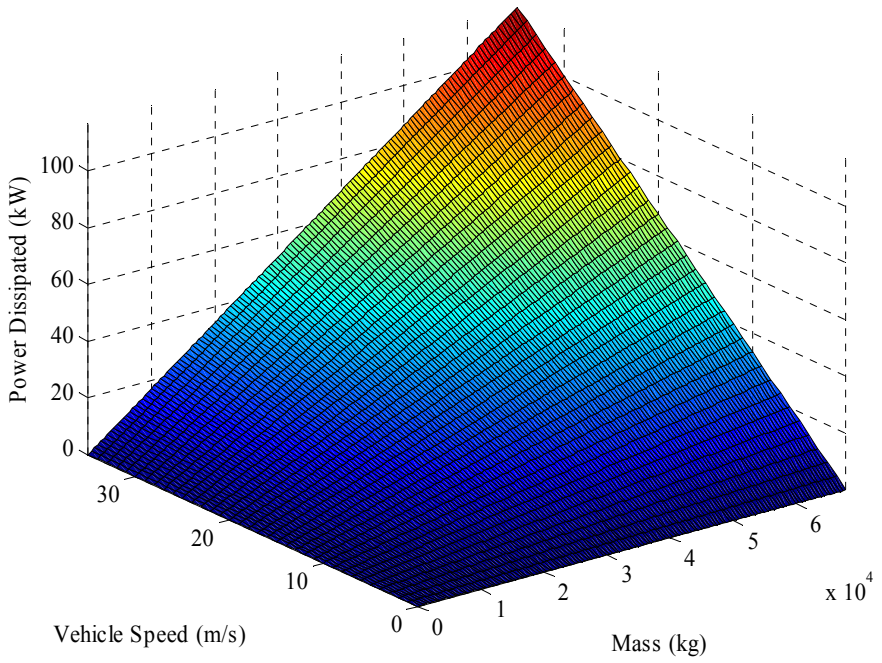

Figure 2.5. Model of Power Losses Involved In Rolling Resistance

Generally, rolling resistance is caused by many complicated mechanisms within the tire itself. Primary energy losses occur in the tire sidewall or contact area and tread elements as the tread travels through the contact patch with energy being dissipated in the hysteretic and viscoelastic friction of the rubber and carcass elements. Rubber exhibits viscoelastic behavior, where stress is a function of strain rate, and thus dissipates energy which accounts for 80-95% of total rolling resistance [LaClair, 2005]. Other losses occur due to tire slip in the lateral and longitudinal directions, energy loss from bumps, deflection of the road surface, tire temperatures, tire inflation pressure, tire design, and other sources [Milliken, 1995]. Because the tire construction materials are strain rate sensitive, meaning the materials exhibit some damping, the rolling resistance coefficient is usually a function of the tires rolling speed. The most common model that accounts for

more external parameters is described in the SAE specification J2452 that gives the rolling resistance force to be a function of tire inflation pressure, normal load, and velocity in a second order relationship, as shown in Equation 2.9.

$$F_{RR} = P_{tire}^{\alpha} F_Z^{\beta} \left[a + bV + cV^2 \right] \qquad 2.9$$

Figure 2.6 shows the power consumed by rolling resistance using the SAE J2452 rolling resistance models and sample heavy truck steer tire parameters.

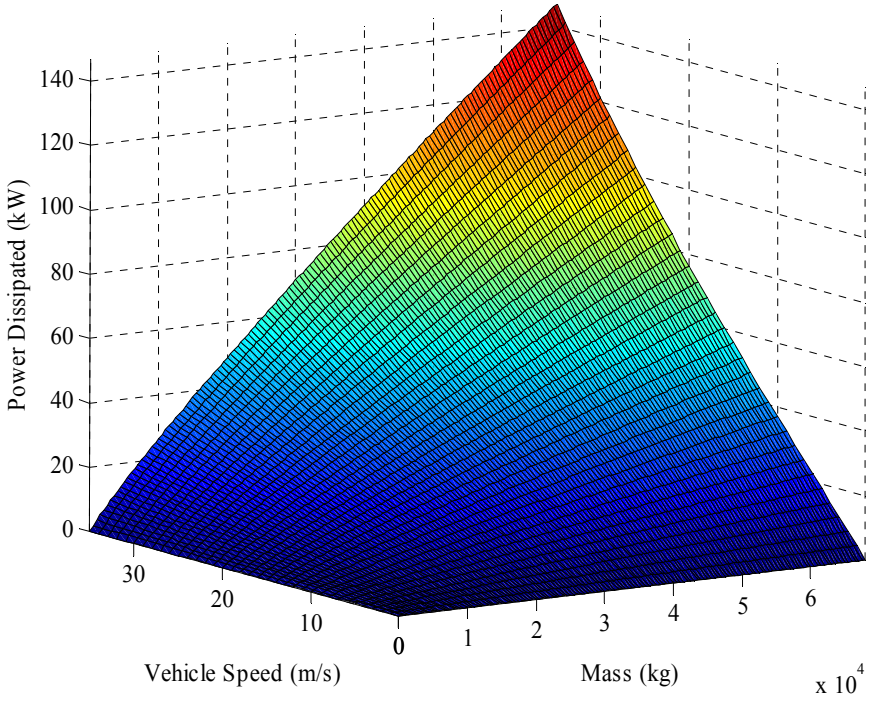

Figure 2.6. Model of Non-Linear Power Losses Involved In Rolling Resistance

2.4 Longitudinal Turning Losses

The generation of lateral force with a pneumatic tire produces a longitudinal drag force [Dixon, 1996].

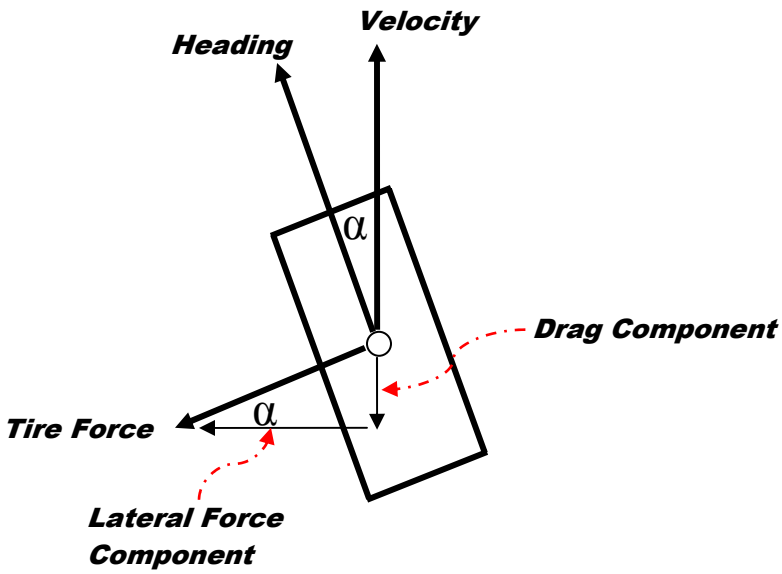

Figure 2.7. Tire Force FBD

The tire diagram in Figure 2.7, shows a tire heading vector and a tire velocity vector, or actual path the tire is traveling. The angle between these two vectors is called the tire slip angle, α, and is necessary to generate lateral force. The lateral force generated by the tire is produced perpendicular to the tire's carcass or heading which results in a component that acts as drag force. This drag component arises due to the slip angle and is therefore a function of that tire's slip angle, as shown in Equation 2.10.

$$Drag_{force} = Force_{lateral} \sin(\alpha) \qquad 2.10$$

This equation can be examined to show how much energy is being put into the tire, or lost from longitudinal forces in order to quantify how much longitudinal drive force from the engine has to be applied in cornering to maintain constant speed. The total

energy consumed and power consumed by tire cornering forces and slip angle is shown in Equations 2.11 and 2.12.

$$Energy = Force * dist = (Force_{lateral} \sin(\alpha))(V(dt)) \quad 2.11$$

$$Power = \frac{energy}{time} = (Force_{lateral} \sin(\alpha))(V) \quad 2.12$$

Figure 2.8 shows a plot of power consumed when a class 8 truck goes around the corner of the National Center for Asphalt Technology. As shown in the figure, power losses due to lateral force can be very significant, especially at high velocities or high slip angles.

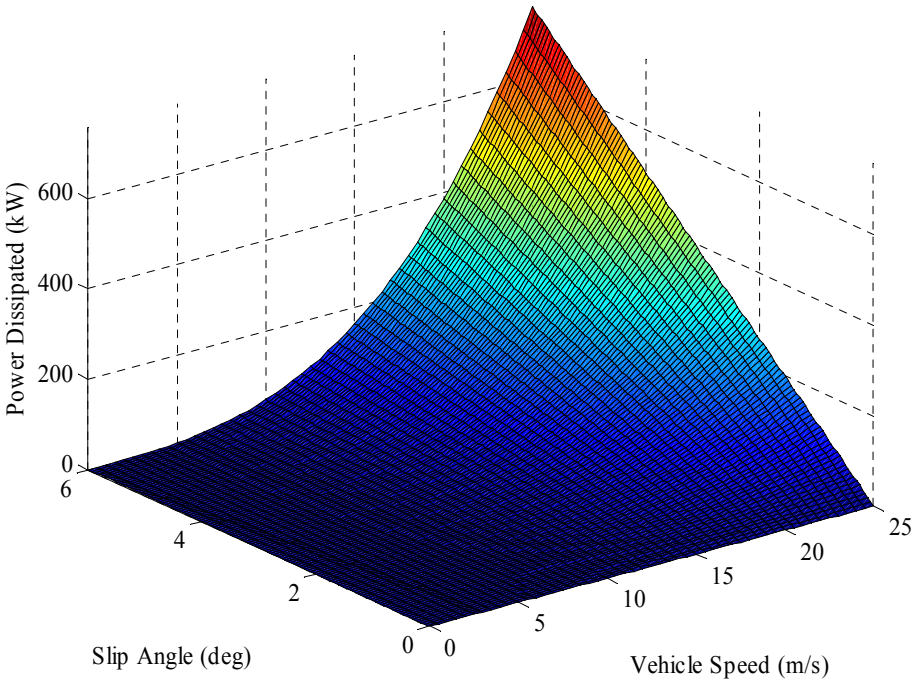

Figure 2.8. Tire Cornering Losses on a Constant Radius Turn

2.5 Fuel Economy Effects

Because the losses described in this chapter contribute to longitudinal drive inefficiency, the engine must provide some force to overcome these forces. This force comes at some expense, mainly fuel consumption. The fuel consumed by an engine goes not only to drive forces but to many different inefficiencies, which include engine inefficiencies, friction and pumping losses, vehicle losses, and the losses described in the model developed in the chapter. The relative magnitudes of these losses are described in Fig 2.9.

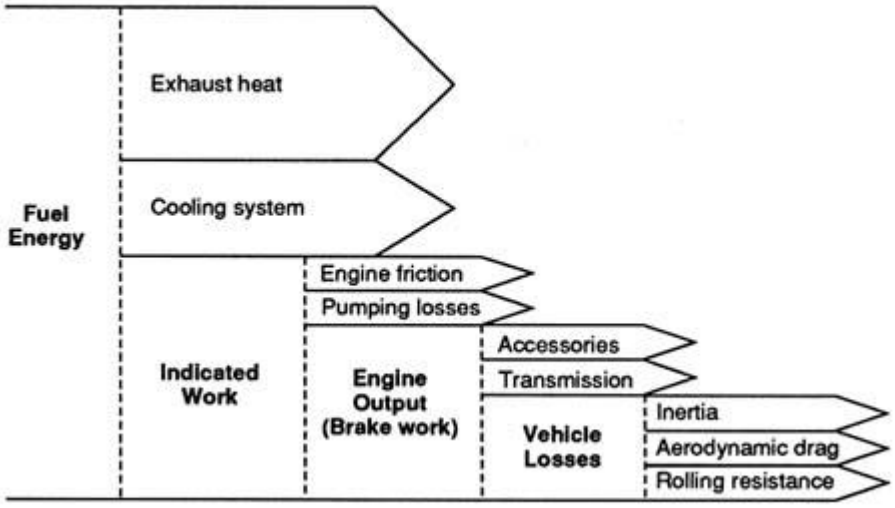

Figure 2.9. Magnitude of Energy Losses in a Vehicle (Reprinted from [LaClair, 2005])

Fuel economy effects from losses are significant. Fuel consumed can be approximated as being proportional to power necessary to overcome these losses which has been shown for each individual loss in Figures 2.2 through 2.5. Figure 2.10 shows the magnitudes of power consumed due to rolling resistance and air drag losses for a Class 8

truck at the NCAT facility, assuming pure longitudinal motion, ie: no turning, and no road grade.

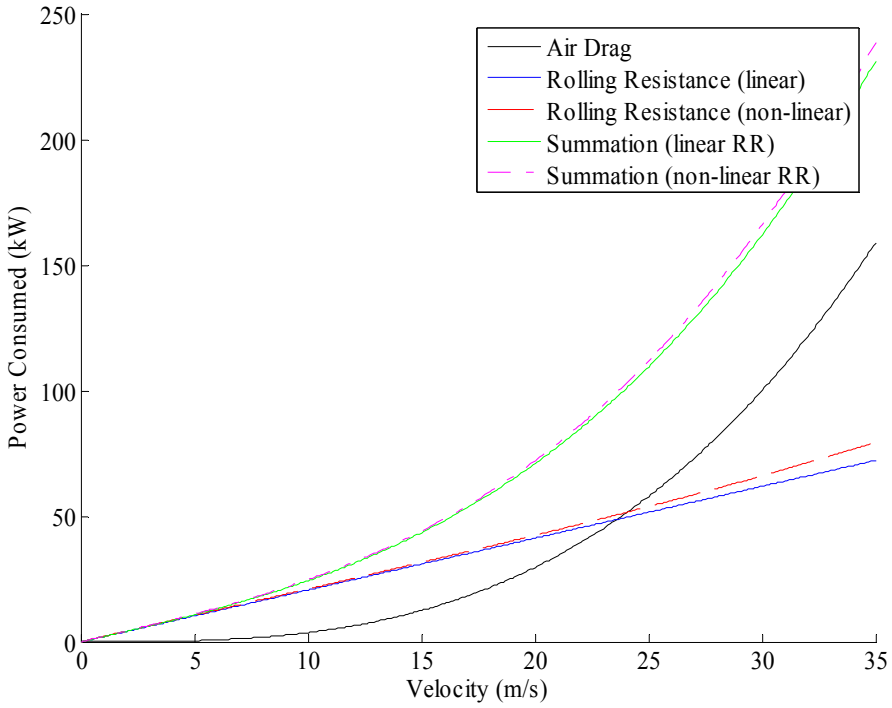

Figure 2.10. Magnitude of Power Losses in a Class 8 Truck

Research has been done to show the realizable effect of improving rolling resistance has on fuel economy. Trends clearly show that an increase in road texture yields an increase in fuel consumption [DeRaad, 1978]. Most research assumes a linear energy based fuel consumption map. However, work has been done to develop an actual engine map to quantify engine fuel usage as a function of engine speed and load (brake mean effective pressure) [LaClair, 2005]. This works shows the ability to quantity fuel usage and the results show that the economy improvements are indeed proportional, with some scale factor, to the rolling resistance for a given drive cycle. For example in a

highway drive cycle, the most common cycle, LeClair shows a decrease of 2.3% fuel consumption with a decrease of 10% rolling resistance coefficient.

2.6 Truck Simulations

Numerically integrating the equation of motion shown in Equation 2.1, a simulation of longitudinal vehicle motion can be performed using known vehicle parameters. Figure 2.11 shows a Freightliner truck as equipped and loaded as the NCAT vehicles, accelerating from a standstill under full power.

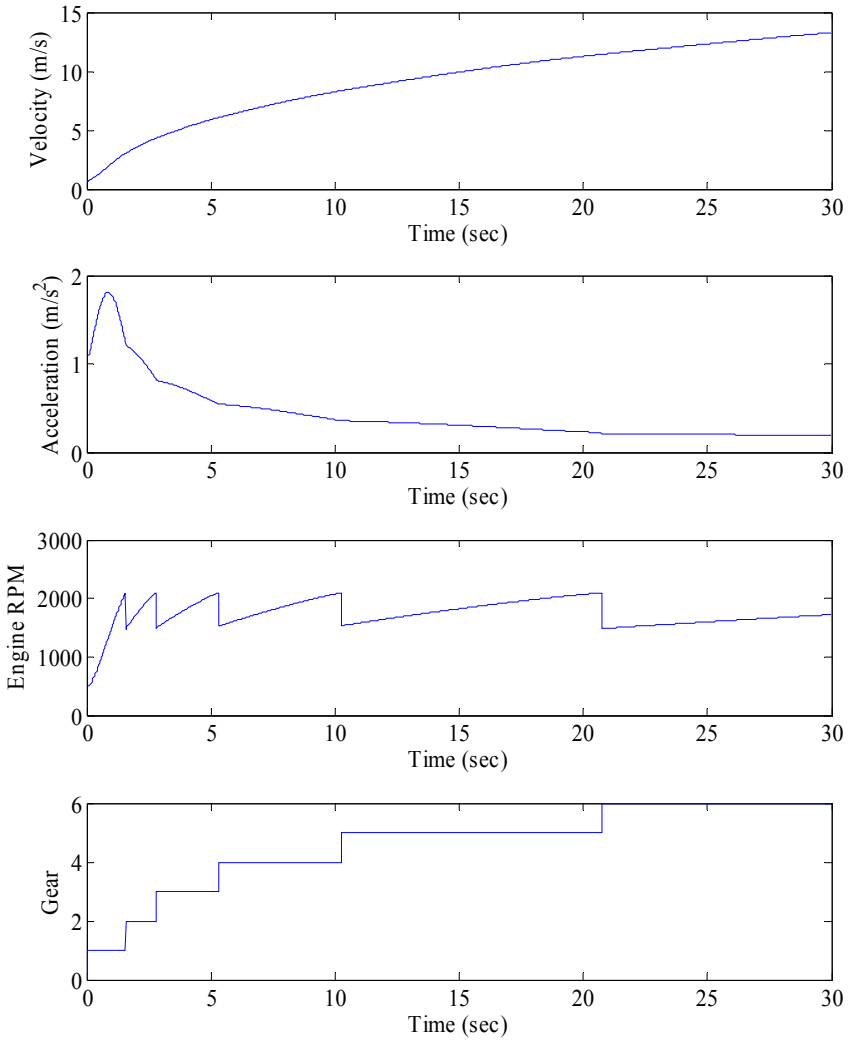

Figure 2.11. Longitudinal Simulation Results

To analyze road load at the NCAT test track in more detail, track elevation data was taken. Vertical survey measurements for inside and outside truck wheel-paths were taken at specific locations on the track. The inside and outside wheel paths were averaged to get an average road height as the vehicles center of gravity will tend to be positioned about the center of the road. The resulting surface elevation as a function of track position

is shown in Figure 2.12. Then a high order polynomial was fit to the data to yield a function representing the track surface.

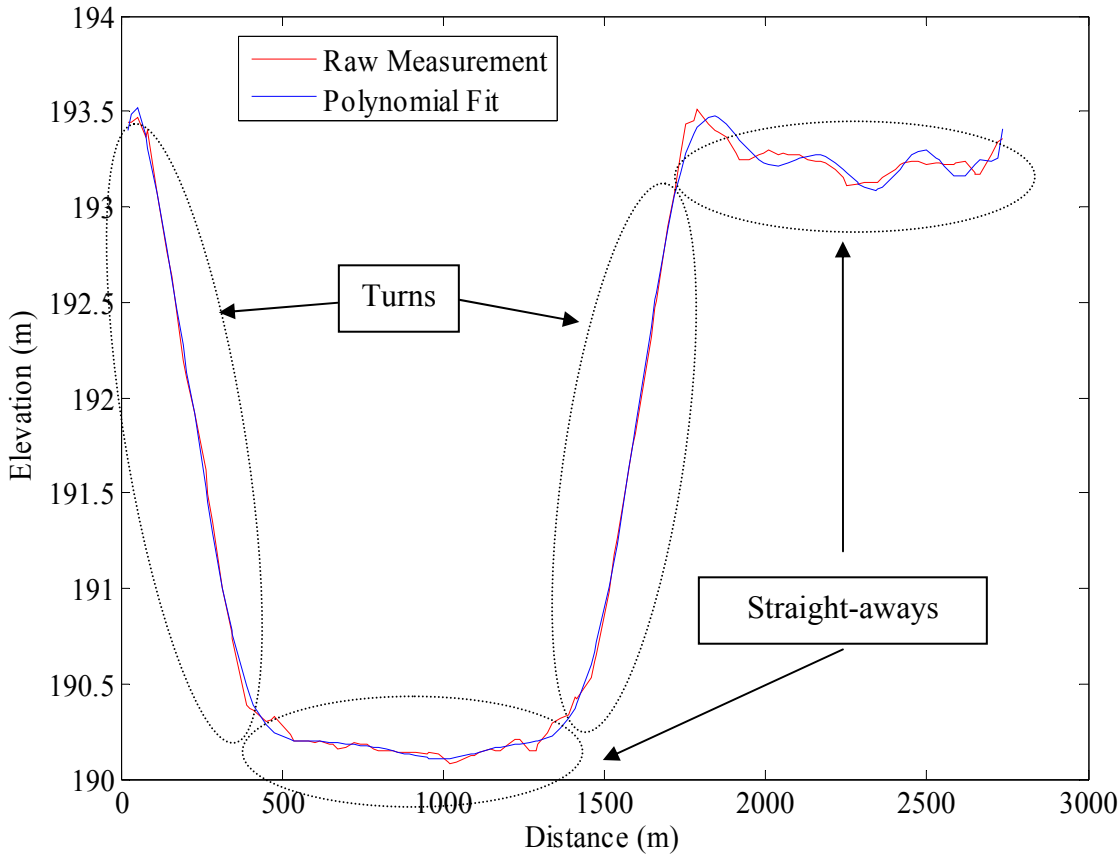

Figure 2.12. Measured NCAT Test Track Elevation Data

To calculate road load due to elevation changes, it is necessary to know the road slope. Discretely calculating slope between data points can produce noisy results, so an analytical polynomial fit was applied to the data. Both this analytical fit, and the original raw data, were differentiated to achieve a road slope measurement, as shown in Figure 2.13.

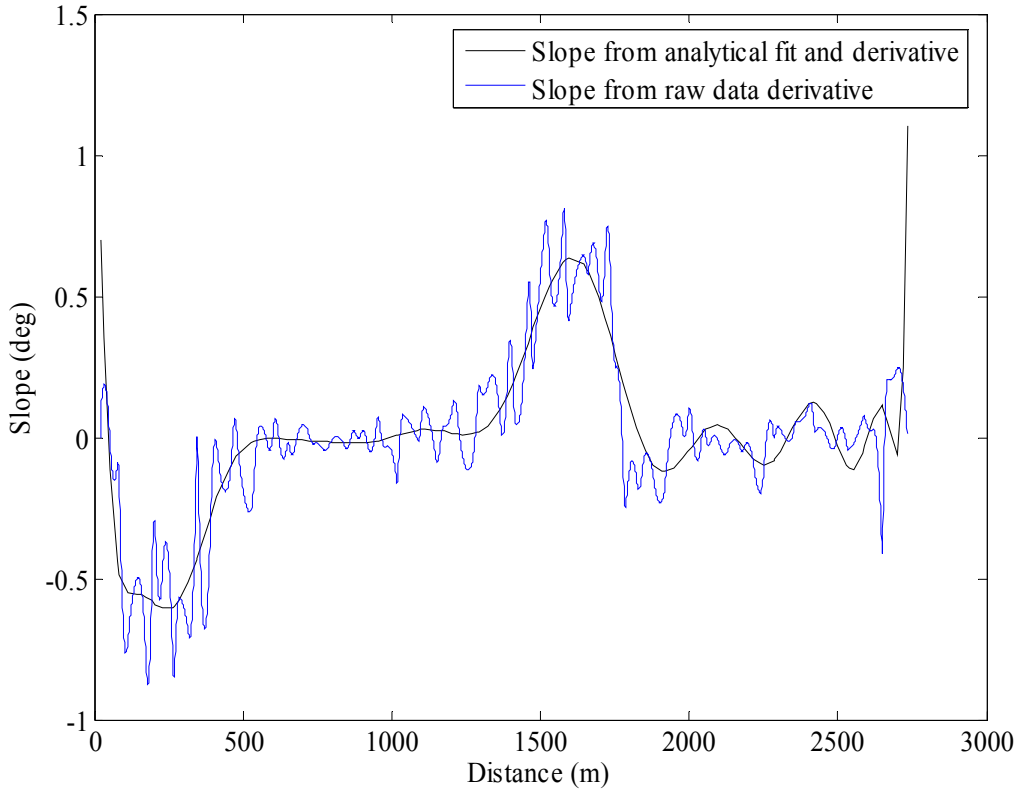

Figure 2.13. NCAT Test Track Slope

This road grade calculation was used to perform a road load analysis for the NCAT track, calculating the individual losses as described earlier in this chapter. Figure 2.14 shows the magnitudes of each loss for a constant speed simulation of 20.11 m/s (45 mph). Air drag force and rolling resistance force are almost equal at the simulated speed, where the road grade induced longitudinal force around the track causes large swings in the overall vehicle longitudinal loading.

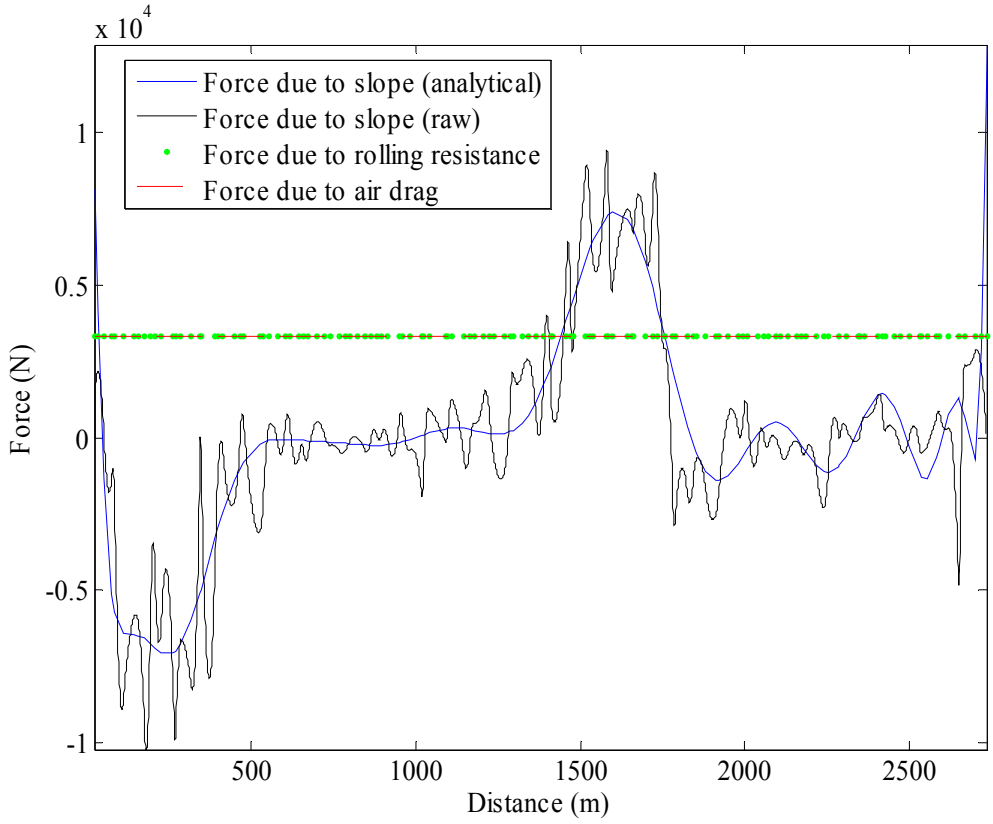

Figure 2.14. Magnitude of Loss Components at NCAT Track

The elevation data can be used to further simulate vehicle performance at the track. A non-constant velocity simulation was performed of an accelerating vehicle, as in Section 2.6, where the road grade of the test track was introduced. Figure 2.15 shows the vehicle's acceleration and the influence the small elevations changes can have on the vehicle's performance. It is shown to loose acceleration in the steepest section of the track at about 25 m/s even while under full power.

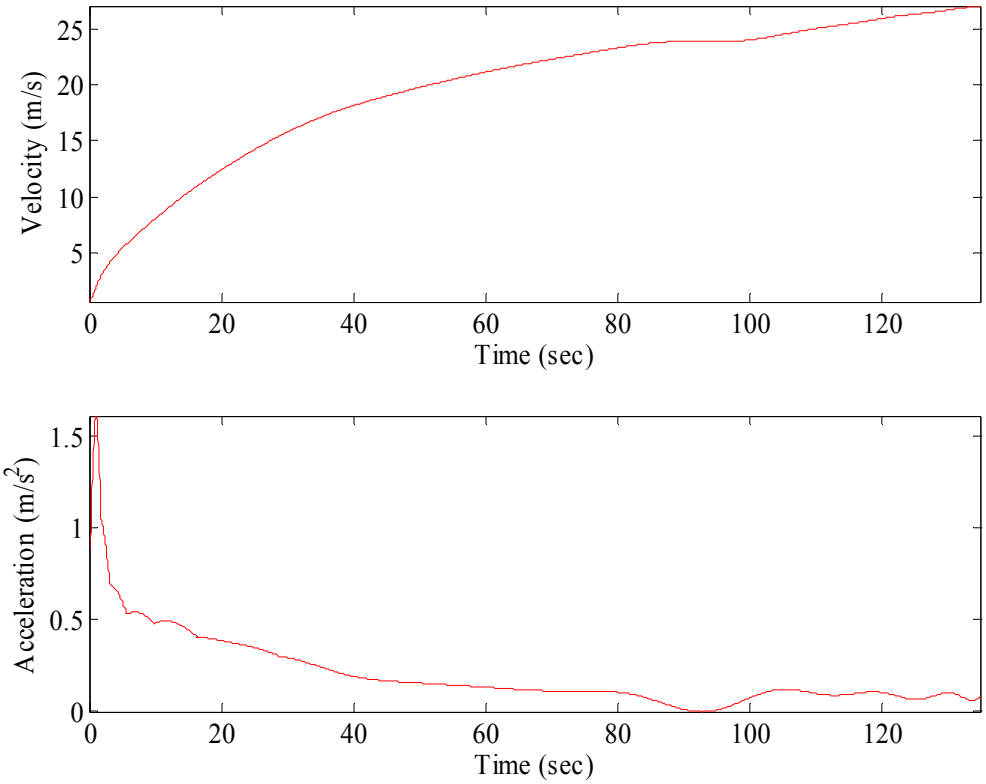

Figure 2.15. Class 8 Truck Acceleration Performance with NCAT Track Road Profile

2.7 Conclusions

A mathematical model representing the longitudinal dynamics of vehicles has been developed and simulated. This model includes loss terms that have been described individually and mathematically modeled to understand their relative magnitudes and impact on longitudinal vehicle dynamics. Inefficiencies and losses are shown to have significant impact on fuel economy and their magnitudes are simulated. The model is then numerically simulated to show heavy truck longitudinal behavior and performance.

Further simulations of road load are applied specifically to the NCAT test track and are shown to have significant performance effects.

CHAPTER 3

ADVANCED MODELING

3.1 Introduction

In this chapter, more advanced topics of longitudinal vehicle dynamics are discussed. A more complex longitudinal model of a rolling vehicle that includes inertias is developed and simulated. This chapter also includes models for sensors that are included in the vehicle simulations to predict sensor outputs when measuring the longitudinal vehicle dynamics. These models are then used to predict longitudinal truck behaviors in various environments, including those at the NCAT test track.

3.2 Advanced Longitudinal Model

The advanced longitudinal model developed in this chapter has one degree of freedom and was derived using the equations of motion for the free body diagrams shown in Figure 3.1. This figure is similar to that in Chapter 2, except Figure 3.1 includes an additional inertia force.

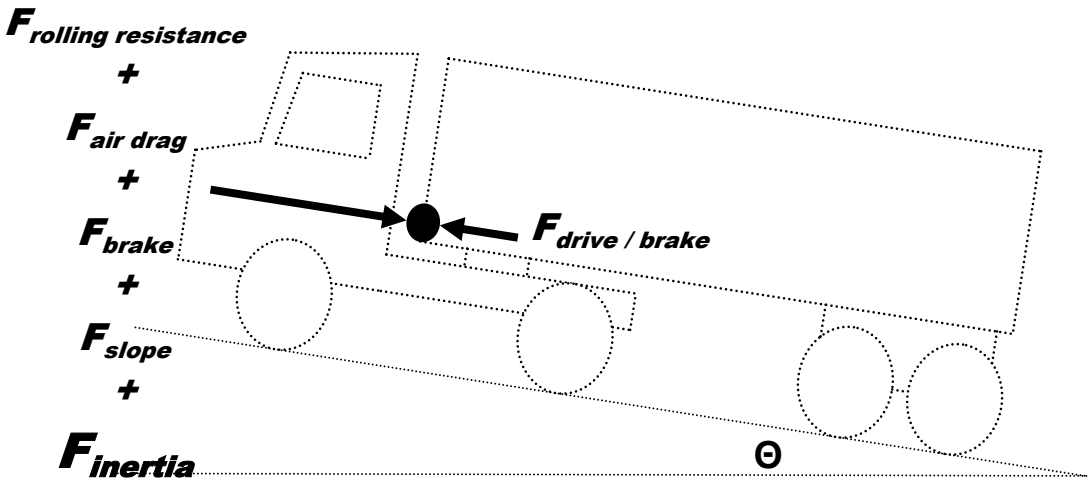

Figure 3.1. Advanced Longitudinal FBD

To increase the model's fidelity and more accurately simulate the longitudinal dynamics, the mechanical systems through which the engines power is transmitted must be modeled. The amount of torque delivered to the wheels in a system which is accelerating/decelerating is reduced by inertial losses in addition to the viscous and friction losses in the drivetrain. The previous model accounts for these by using an efficiency term, but here a more advanced model is developed.

The advanced model which contains driveline dynamics due to inertia effects consists of three distinct stages, the engine (I_E), transmission (I_T), and final drive assembly (I_D), as shown in Figure 3.2.

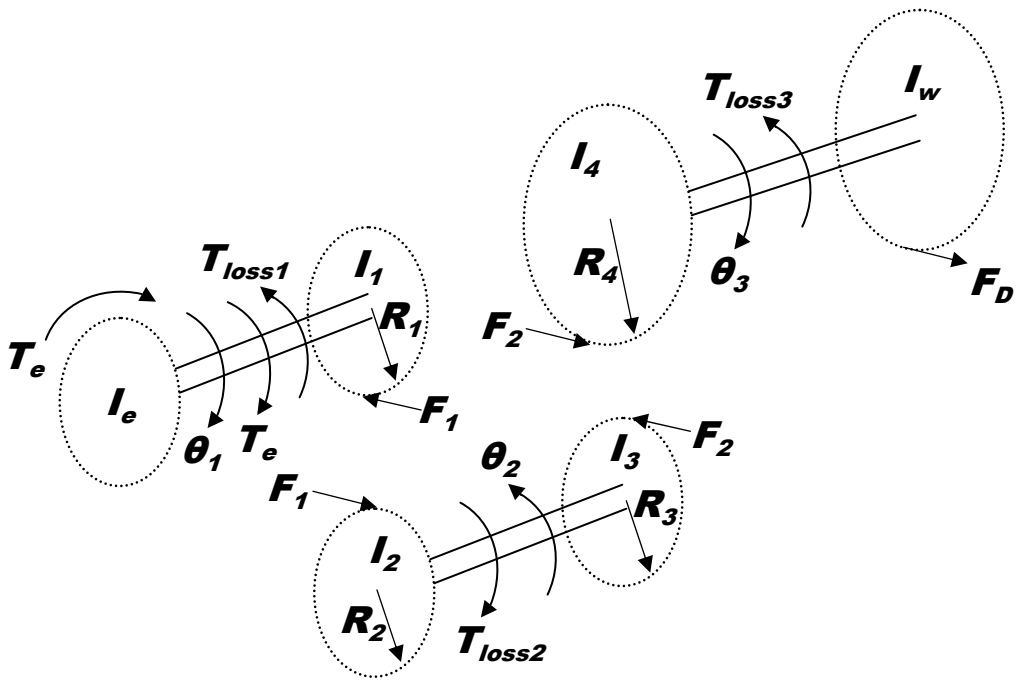

Figure 3.2. Drivetrain FBD

The engine stage includes the vehicle's engine, clutch, and first driving gear of the transmission. The transmission includes all internal gearing and equivalent inertias which drive the final drive and wheel axle assembly.

Deriving the equations of motion for the three stages, including loss terms as a constant and function of rotational velocity, results in Equation 3.1.

$$m_{eff}\,\ddot{x} = \left[\frac{\tau_e N_T N_D}{R_w}\right] - b_{eff}\,\dot{x} - \mathrm{F}_{\mathrm{Loss}} - \mathrm{F}_{\mathrm{Air\ Drag}} - \mathrm{F}_{\mathrm{Rolling\ \ Resistance}} - \mathrm{F}_{\mathrm{Slope}} \tag{3.1}$$

$$N_T = \frac{R_2}{R_1} \tag{3.2}$$

$$N_D = \frac{R_4}{R_3} \tag{3.3}$$

This equation of motion contains new terms for effective mass, effective damping, and forces from losses. These additional mass, damping, and loss coefficients are described in Equations 3.4 through 3.5.

$$m_{eff} = \left[m + \frac{I_E N_T^2 N_D^2}{R_w^2} + \frac{I_T N_D^2}{R_w^2} + \frac{I_D}{R_w^2} \right] \tag{3.4}$$

$$b_{eff} = \left[\frac{b_1 N_T^2 N_D^2}{R_w^2} + \frac{b_2 N_D^2}{R_w^2} + \frac{b_3}{R_w} \right] \tag{3.5}$$

$$\mathrm{F_{loss}} = \left[\frac{\tau_{loss1} N_T N_D}{R_w} + \frac{\tau_{loss2} N_D}{R_w} + \frac{\tau_{loss3}}{R_w} \right] \tag{3.6}$$

where:

$$I_E = I_e + I_1 \tag{3.7}$$

$$I_T = I_2 + I_3 \tag{3.8}$$

$$I_D = I_4 + I_w \tag{3.9}$$

The effective mass term includes the effects of the various inertias in the driveline relating to vehicle longitudinal motion (i.e.: acceleration). Viscous losses, which act as a function of velocity, and constant losses are included for each stage as well. This model is more accurate as it will be shown that the effective mass can be significant in the longitudinal performance.

3.3 Simulations of Vehicle Models, Simple and Complex

3.3.1 Acceleration Simulations

Continuing the simulations performed in Section 2.6 (mass model), a longitudinal simulation with the model described in Section 3.2 (inertia model) is shown in Figure 3.3.

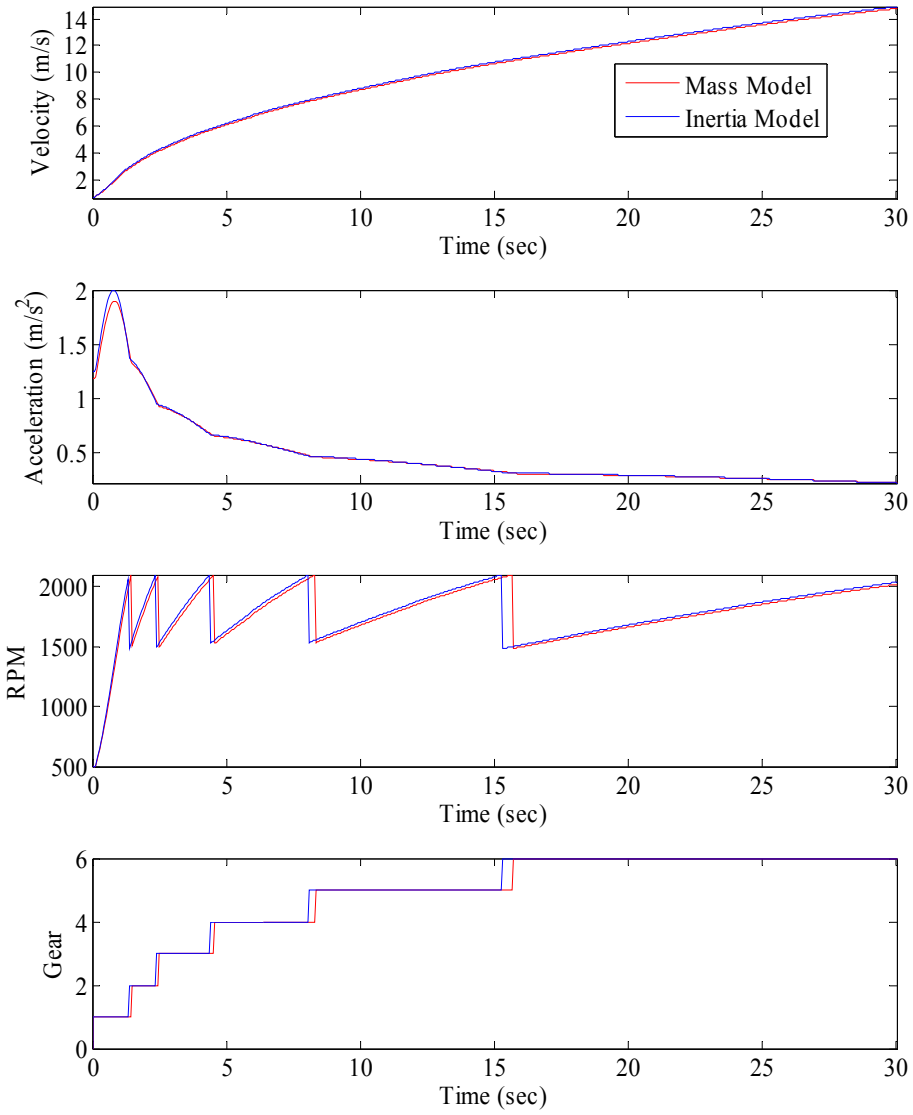

Figure 3.3. Advanced Longitudinal Model Simulation, Acceleration Case

The model that includes inertias and losses shows a small difference in the behavior of an accelerating truck from the model in the previous chapter. Velocities reached after thirty seconds were approximately 2% lower than that of the model that ignores these additional components. However, the new model does capture dynamics in

the drivetrain components that contribute to slowing the vehicle's acceleration, especially at lower speeds when the angular accelerations of these components are higher than later in the run. This behavior can also be described by examining the values of m_{eff} throughout the run. In lower gears, the values of m_{eff} are the highest and therefore have the largest effect on acceleration performance, which is shown in Figure 3.4.

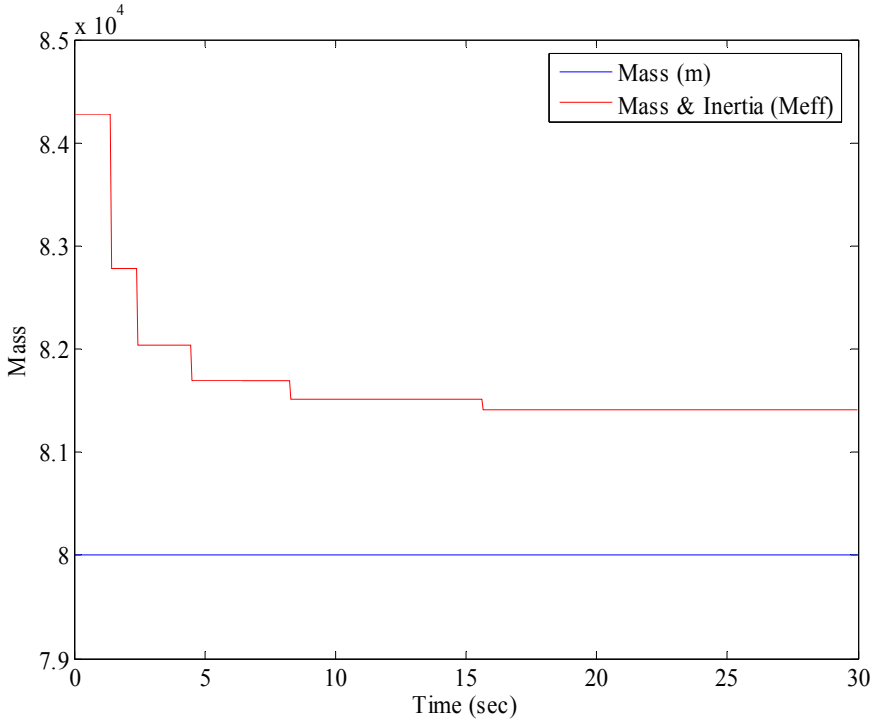

Figure 3.4. Equivalent Masses Modeled During Acceleration Case

3.3.2 Deceleration Simulations

Inertias and losses can have a similar effect on vehicle deceleration. Figure 3.5 shows a simulated truck coast-down with no drive force and only longitudinal vehicle

losses. The simulation assumes the transmission is in the neutral position and the only inertia that effects the dynamics are those of the last stage, including the wheels, rear-end/differential, drive shaft, and the driven transmission shaft.

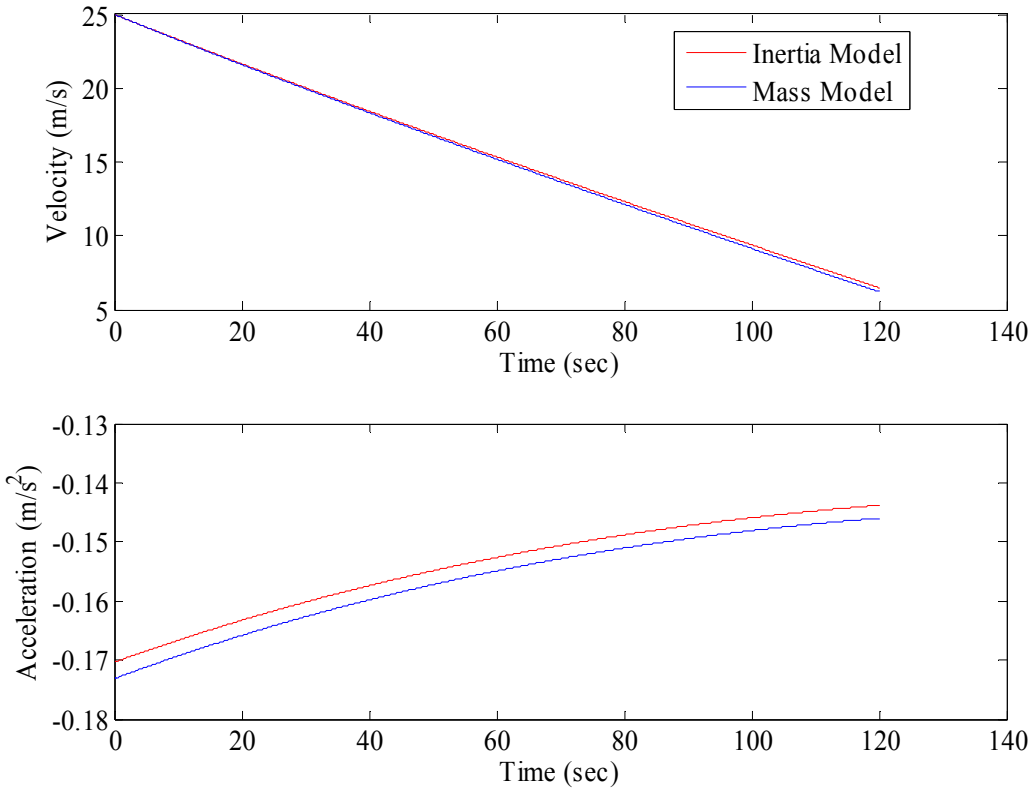

Figure 3.5. Advanced Longitudinal Model Simulation, Coast Down Case

The plot shows that the vehicle decelerates slower with the inertias included in the model due to the increase in the m_{eff} term. In the above analysis the slopes of Figure 3.5 are representative of the m and m_{eff} terms, where the non-linearities are caused by losses, which are functions of velocity.

3.3.3 NCAT Track Simulations

Vehicle simulations were performed to simulate a heavy truck traveling around the 1.7 mile oval test track at the NCAT facility. The NCAT track surface is paved with 45 discrete sections of asphalt which are simulated by producing a matrix of 45 varying rolling resistance values. The values are chosen to be +/- 5% of nominal values given in Appendix A. The vehicles dynamics shown in Equation 3.1 were simulated using a constant drive force provided by the engine. This constant force is the equivalent road load associated with a velocity of 20.11m/s (45mph) and an average of the rolling resistance values for the asphalt sections.

Figure 3.6 shows a plot of vehicle velocity around the NCAT facility. The mass and inertia models are shown, with variations occurring due to the increased effective mass component in the inertia model. The modeled inertia acts to decrease the high vehicle speeds and increase the lower vehicle speeds, much like a filter.

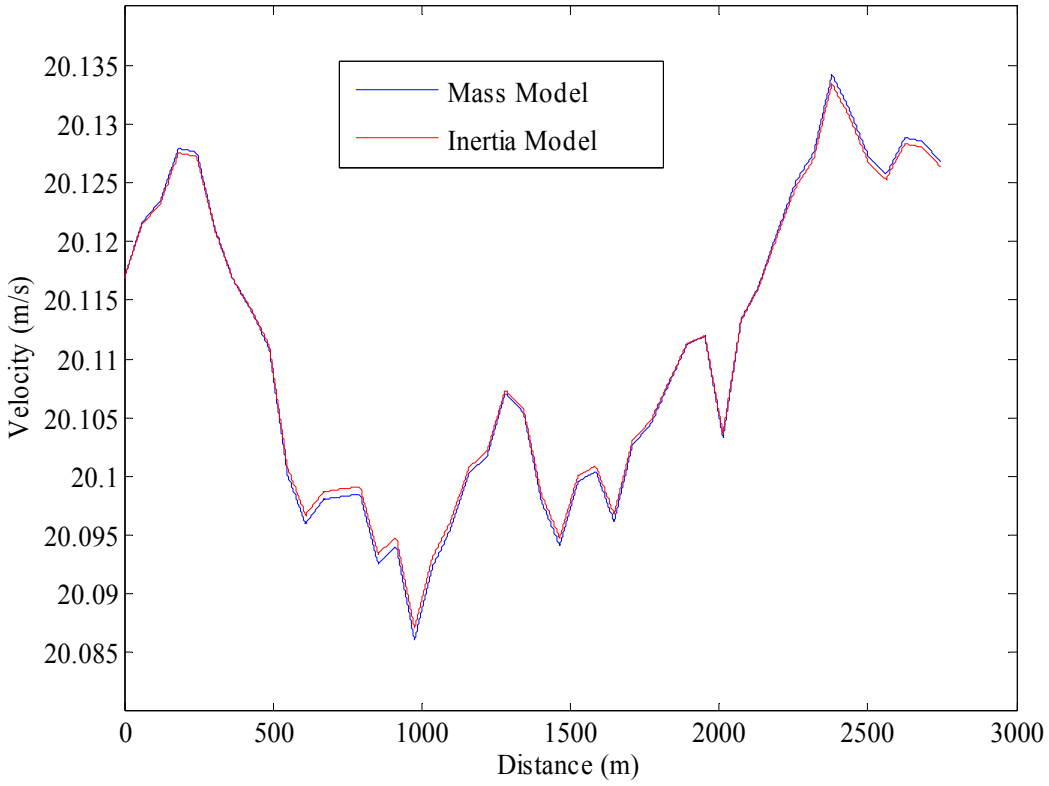

Figure 3.6. Advanced Longitudinal Model Simulation, NCAT Track Velocities

Figure 3.7 shows the vehicle's acceleration behavior in the two models, and more clearly shows that peak accelerations are decreased in the inertia model, as decelerations are also reduced.

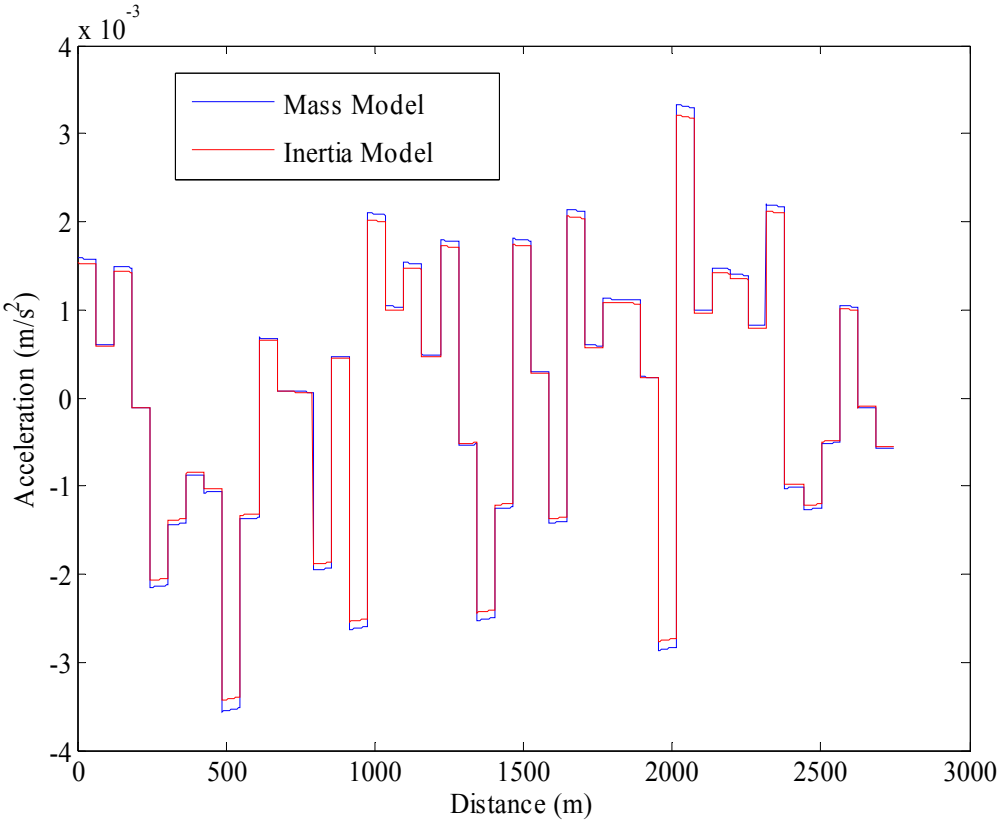

Figure 3.7. Longitudinal Advanced Model Simulation, NCAT Track Longitudinal Accelerations

3.3.4 Model Validation

To validate the model presented in this chapter, simulations were performed using the commercial software package *TruckSim*. This provides a comparison to a source that is accepted as accurate without doing experiments that would disturb existing experiments at the NCAT test track and provide too much wear and tear on the vehicles due to their aggressive nature. A *TruckSim* model was developed using the same engine, transmission, and vehicle parameters used previously and the vehicle dynamics were

simulated in a full acceleration run. Figure 3.8 shows the results of this simulation plotted against those of the model in this chapter.

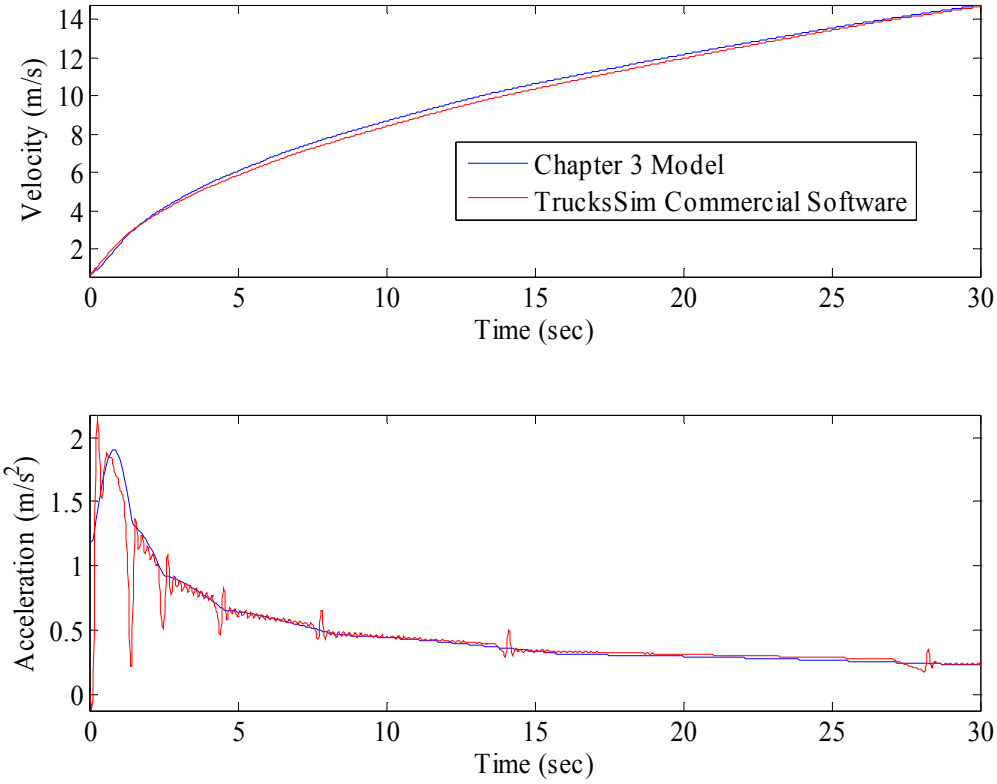

Figure 3.8. Longitudinal Advanced Model Simulation Validation with *TruckSim*

The simulations show very good agreement, with the largest error sources due to the algorithms used during gear shifts. The higher degree of freedom model of *TruckSim* shows additional dynamics in the gear changes which is most likely due to the very quick shifts that were simulated and modeling the dynamics involved. There are also additional dynamics during the acceleration portions that may be due to unmodeled drivetrain

dynamics from elasticity of components and tires. Overall, the differences between the models are small and of an acceptable magnitude.

3.3.5 Model Variations

Figure 3.9 shows the variations between the two models are small when simulating the NCAT test track. Looking at the magnitude of the velocity differences, the velocity result does not vary more that 1 millimeter/second. This variance remains very small for low dynamic situations.

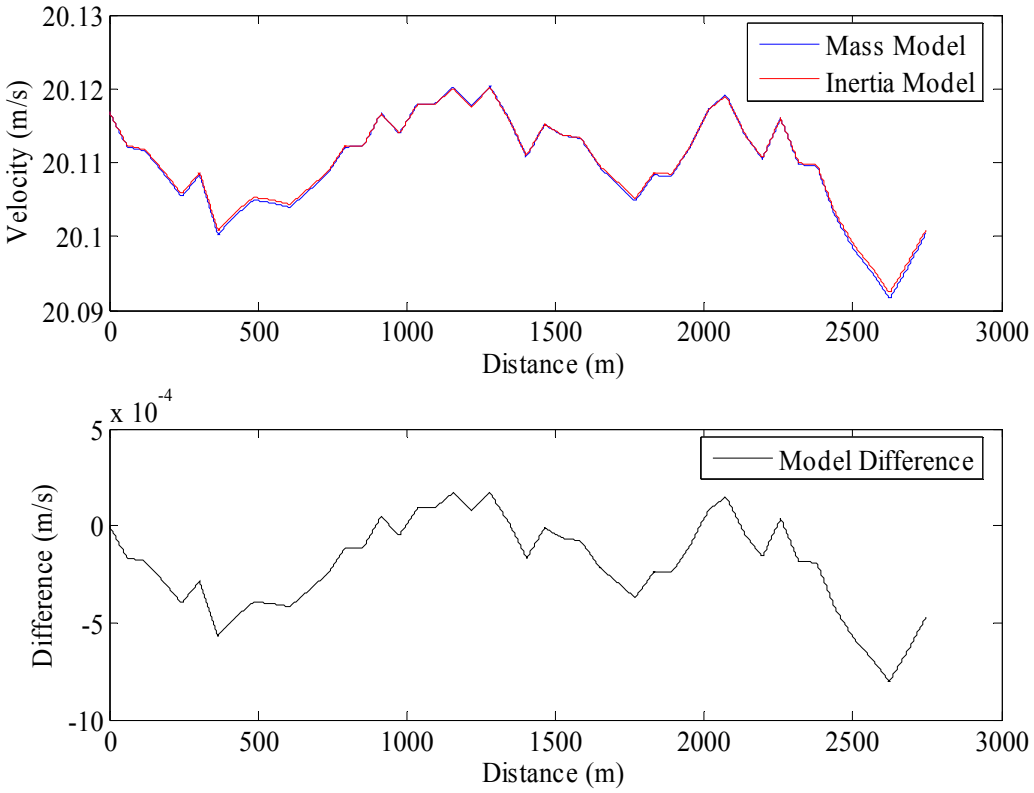

Figure 3.9. Model Differences, NCAT Track Simulation

Considering the acceleration simulation case, the variance between model results is significantly larger than that of the NCAT track. It is quite evident that larger inertia, or smaller mass, results in a more significant difference between the models. To quantify this effect, the mass can be varied in simulation while looking at the RMS difference between the two models' velocities. Figure 3.10 shows a plot of increased vehicle mass, holding the total inertia constant, and the difference produced by the two models.

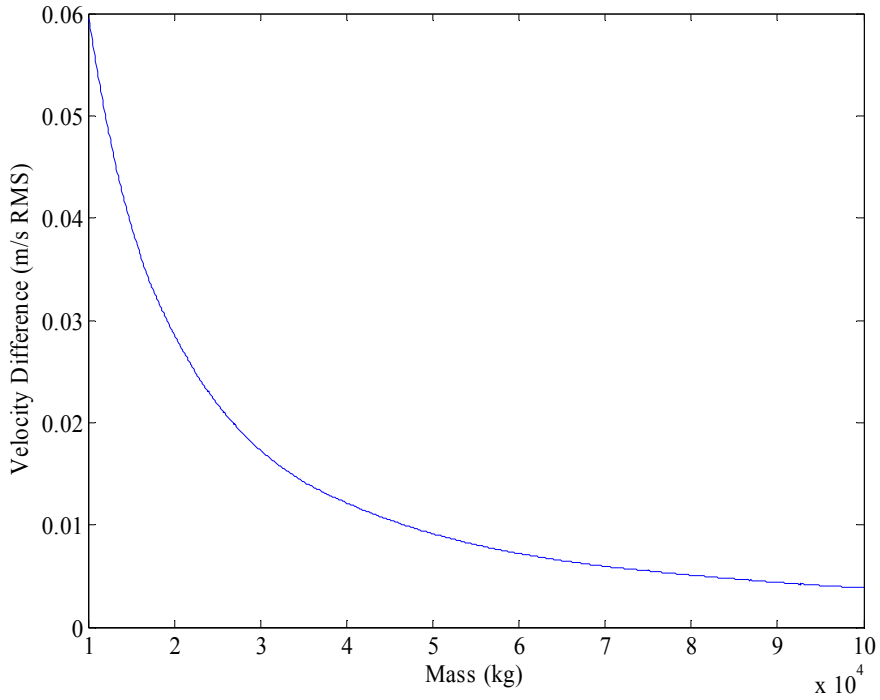

Figure 3.10. Comparison of Velocity Differences Between Models While Varying Mass

Figure 3.11 shows similar results with the values of inertia represented as a ratio to mass ($(m_{eff} - m)/m$). Again, the trends show increasing model differences with the increase in inertia. In simulating and experimenting with the trucks at NCAT these

simulations give an indication of how much error can be expected from a model based on either inertia or mass errors.

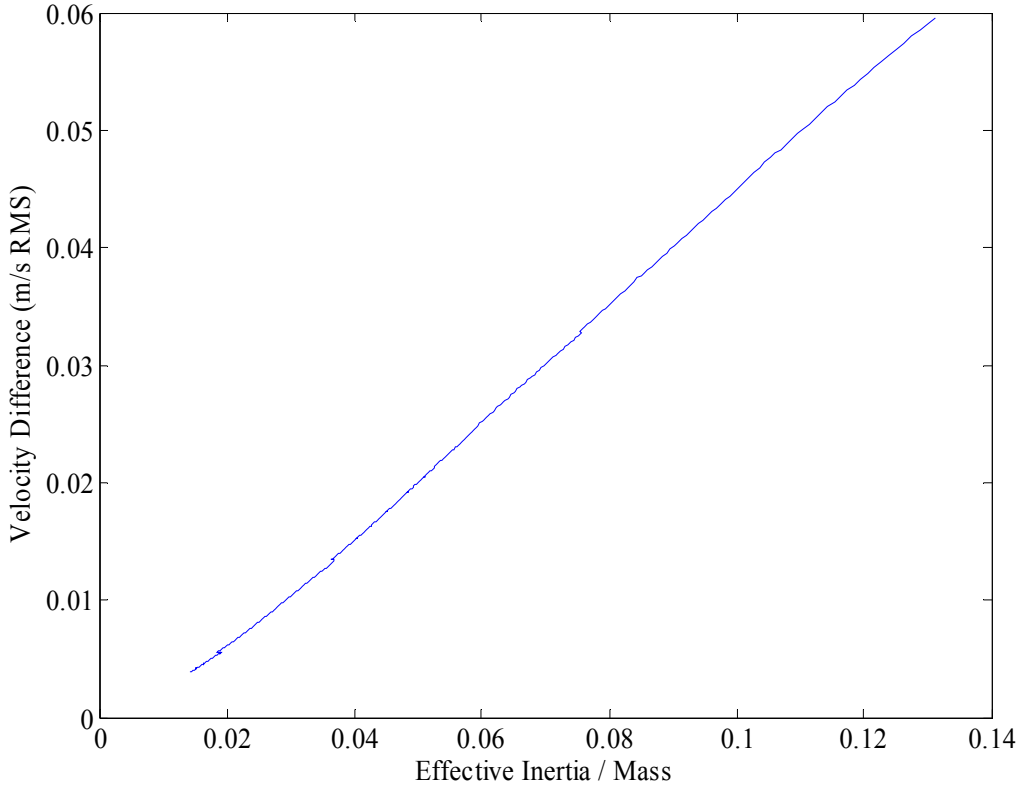

Figure 3.11. Model Velocity Differences as a Function of Effective Mass Ratio

3.4 Noisy Sensor Models and Vehicle Sensor Simulations

In order to analyze truck dynamics at the NCAT facility, modeling and simulating sensor signals is necessary. Using the simulation results of the advanced vehicle model, sensor signals can be simulated by adding noise characteristics of the sensors. A simple

sensor model contains terms that include a scale factor (SF), constant bias or offset (c), moving bias (b), and noise (w), as shown in Equation 3.10 [Flenniken, 2005].

$$y = SFx + c + b + w \tag{3.10}$$

Sensor scale factor is the linear component that relates the scale of the input to output. Sensor noise, often called wide band noise, is of particular interest because it degrades the accuracy of the sensor by some magnitude. The sensor noise is typically modeled as a random zero-mean fashion with a standard deviation that can be found in sensor specifications.

$$E\left[w^2\right] = \sigma^2 f_s \tag{3.11}$$

It should be noted that the noise variance increases with the sample rate (f_s) [Demoz, 2003]. Sensor bias is typically composed of constant (stationary) and walking (non-stationary) components. Sensor quality affects the magnitude and stability of these biases. The non-stationary, or moving bias is often modeled as a first order Markov Process, which simulates first order filtered noise with values for noise and a time constant.

Figure 3.12 shows an example of a signal corrupted by the major sensor inaccuracies. Each noise effect is modeled and added on a linear signal to show their effects on corrupting the original signal or true state. These sensor effects are important for accurately simulating the measurements obtained on the trucks.

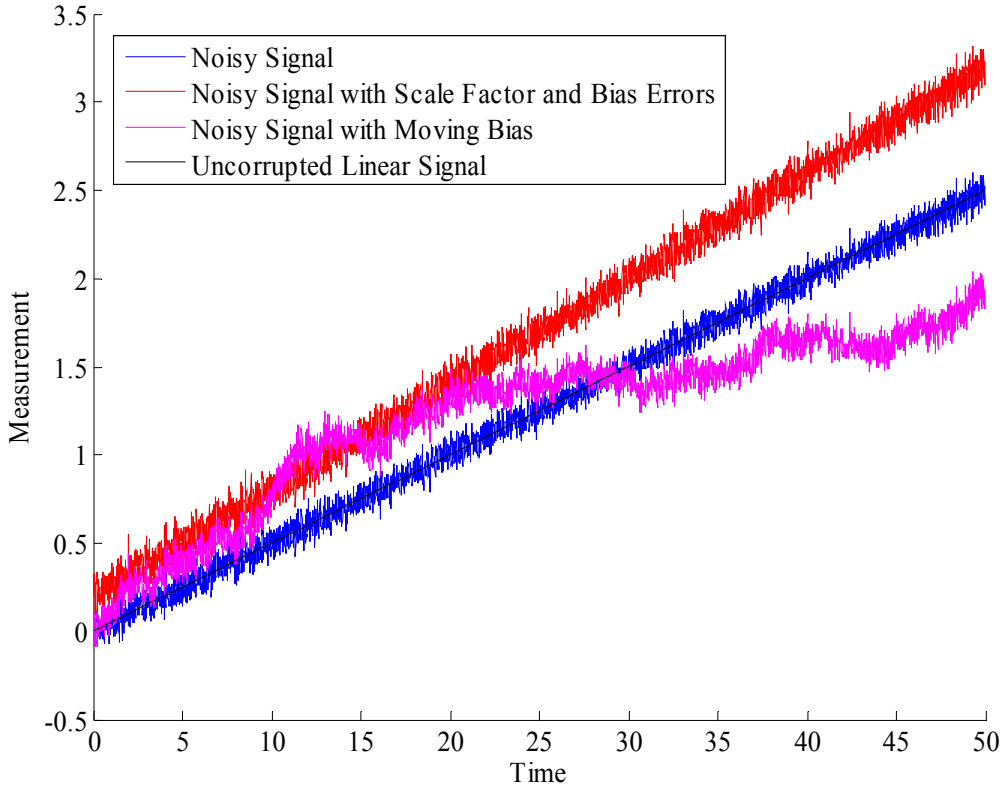

Figure 3.12. Representative Sensor Simulation

This sensor model can be included to the truck simulations to predict sensor outputs. Using noise statistics provided by sensor manufactures, random white noise can be generated and added to the true vehicle states to simulate what a sensor's output would be if used in the vehicle. This simplification to the sensor model assumes a bias free and calibrated sensor and one that is stable enough that the moving bias errors are small.

Figure 3.13 shows simulated velocity and acceleration measurements from the longitudinal acceleration simulation, using the advanced model. Using sensor specs for the Navcomm "Starfire" GPS, velocity noise for the measurement is modeled as 1σ = 0.05m/s and for the Crossbow IMU the accelerometer noise is $1\sigma = 0.00687$ m/s^2.

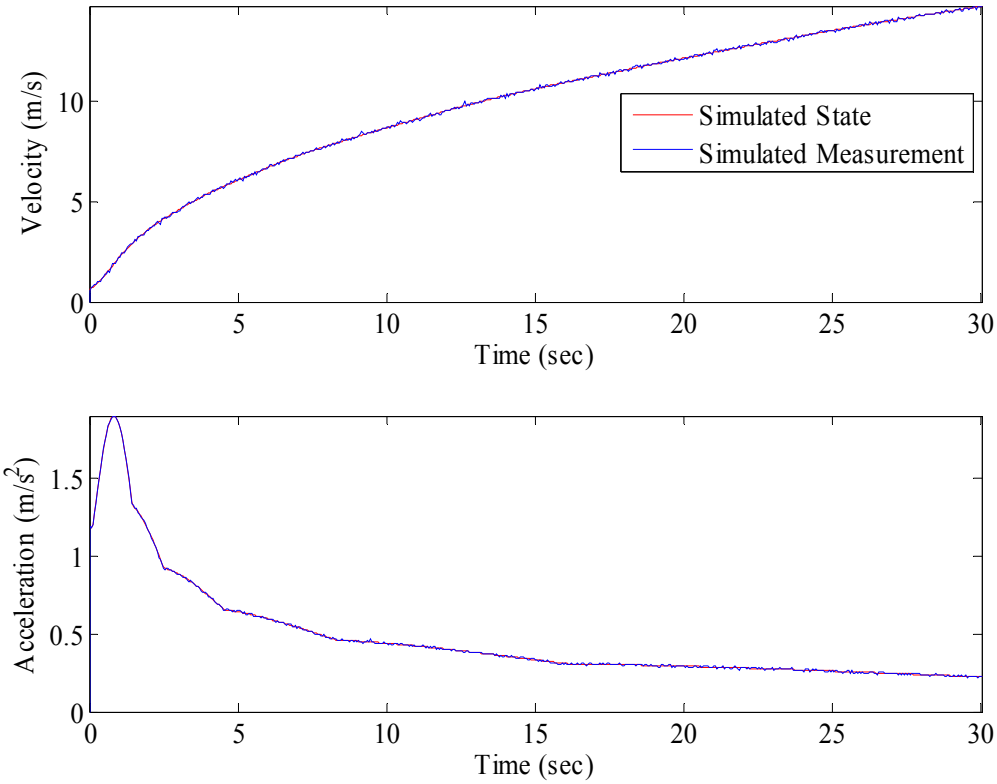

Figure 3.13. Noisy Advanced Longitudinal Model, Acceleration Simulation

Applying the same sensor models to the NCAT track simulation shows the larger influence noise has on the smaller dynamic variations involved in circling the track. Figure 3.14 shows that, due to the small relative velocity differences between asphalt sections, the noise is very dominant over the true signals.

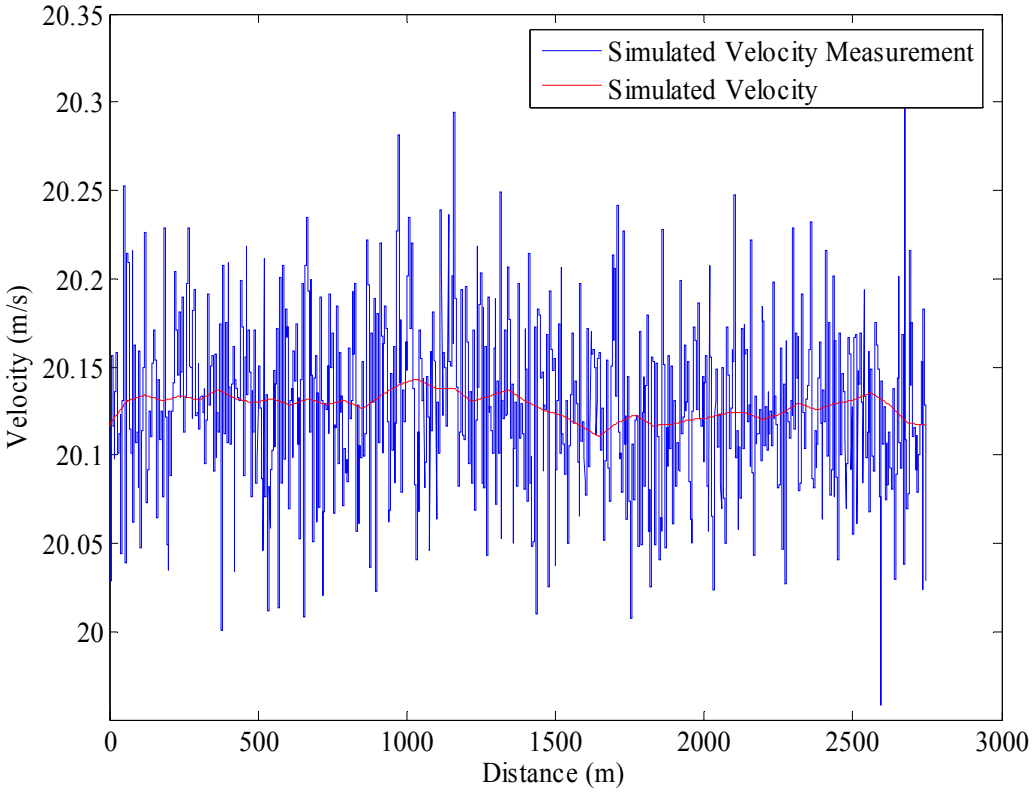

Figure 3.14. Noisy Advanced Longitudinal Model Simulation, NCAT Track Velocities

Additionally, Figure 3.15 shows the small changes in acceleration between the asphalt sections because rolling resistance changes are overwhelmed by accelerometer noise.

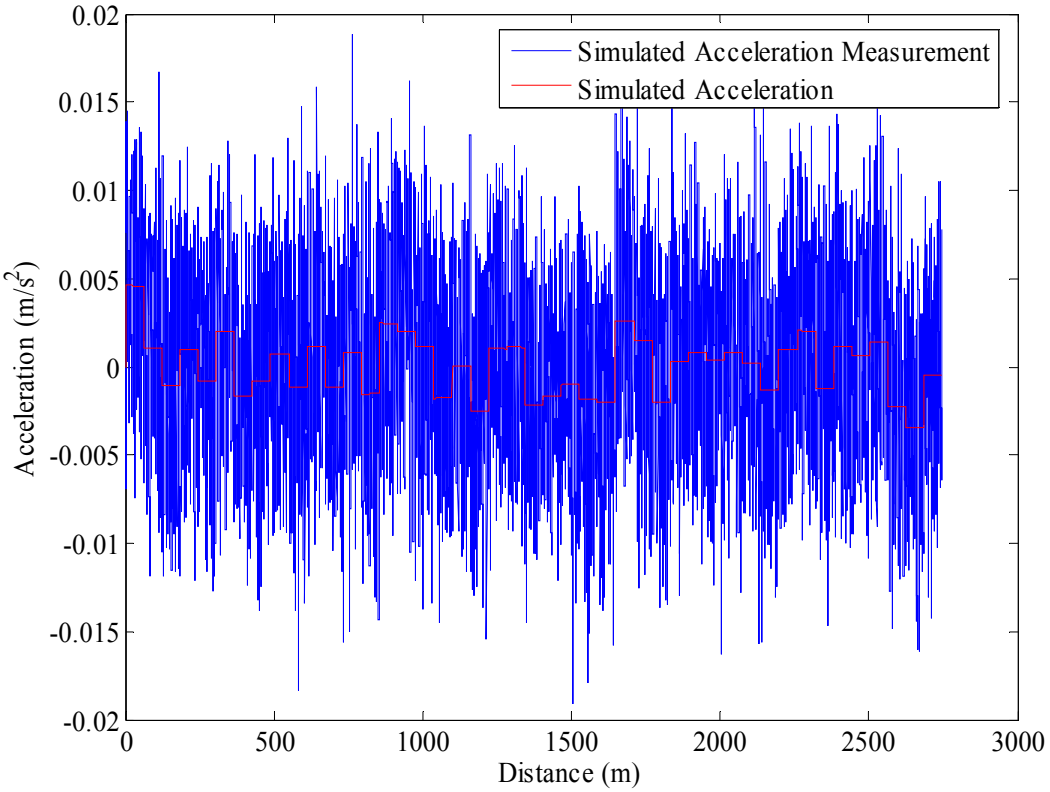

Figure 3.15. Noisy Longitudinal Advanced Model Simulation, NCAT Track Accelerations

Static sensor data was taken to verify the bounds on the random noise the sensors' outputs. GPS and accelerometer data was taken in the cab of the NCAT truck and analyzed for the one sigma bounds. Figure 3.16 shows static GPS velocity noise taken with the truck's engine running. The noise on the "Starfire" velocity had a standard deviation of 0.0411 m/s.

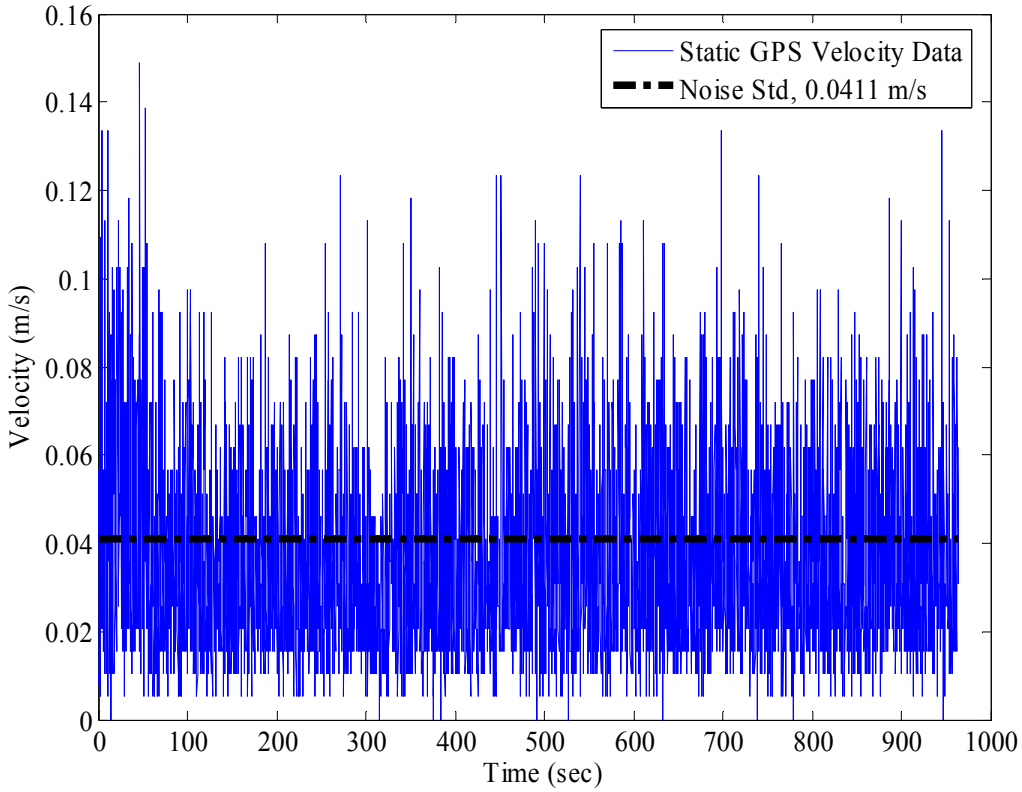

Figure 3.16. Static GPS Velocity, Analyzed for One σ Bounds

Static accelerometer data was taken using the Crossbow manufactured IMU mounted on the trucks, as shown in Appendix A. Figure 3.17 shows the data that was taken and its standard deviation on what should be a static signal. It is important to note that the noise values shown, 0.2118 m/s^2, are higher than the values printed in the sensor data sheets. This is primarily due to the inclusion of process noise which is inserted into the measurement from unknown dynamics, which in this case, is primarily cab vibrations from the vehicle's running engine.

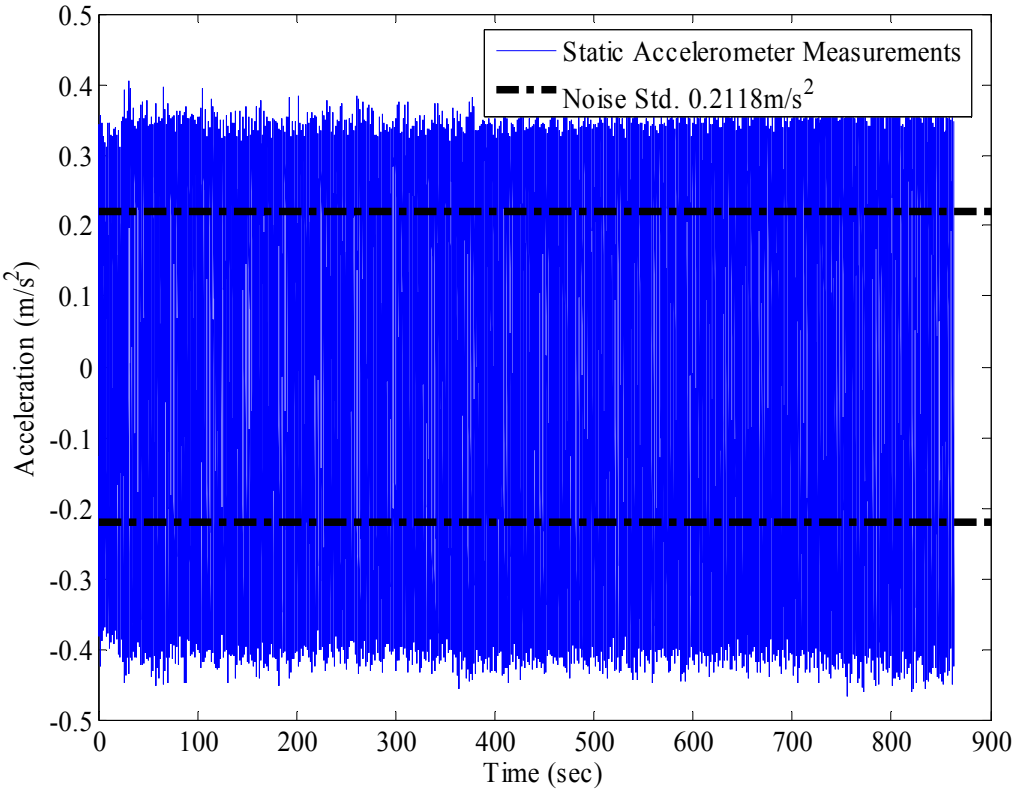

Figure 3.17. Static Accelerometer Data, Analyzed for One σ Bounds

Purely static data was taken with the accelerometer and is shown in Figure 3.18. Looking at the plot, the data is so clean that most error is discritization error and the noise standard deviation is approximately seventy times smaller than when mounted in the trucks, at 0.002975 m/s^2.

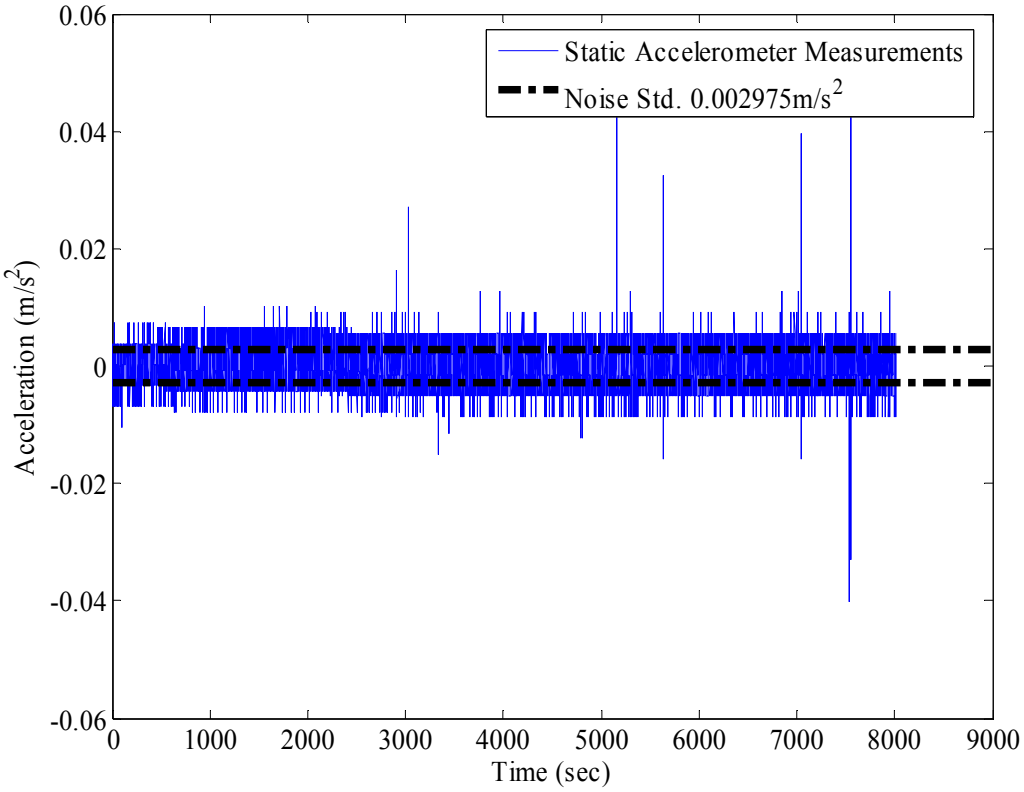

Figure 3.18. Static Accelerometer Data, Analyzed for One σ Bounds

Because such a large amount of noise is injected into the accelerometer measurement when mounted on the trucks, another alternative measurement can be used by differentiating GPS velocity. This results in an estimate of acceleration which is actually slightly cleaner than that shown in Figure 3.17, with a standard deviation on the noise of $0.1416\ \text{m/s}^2$.

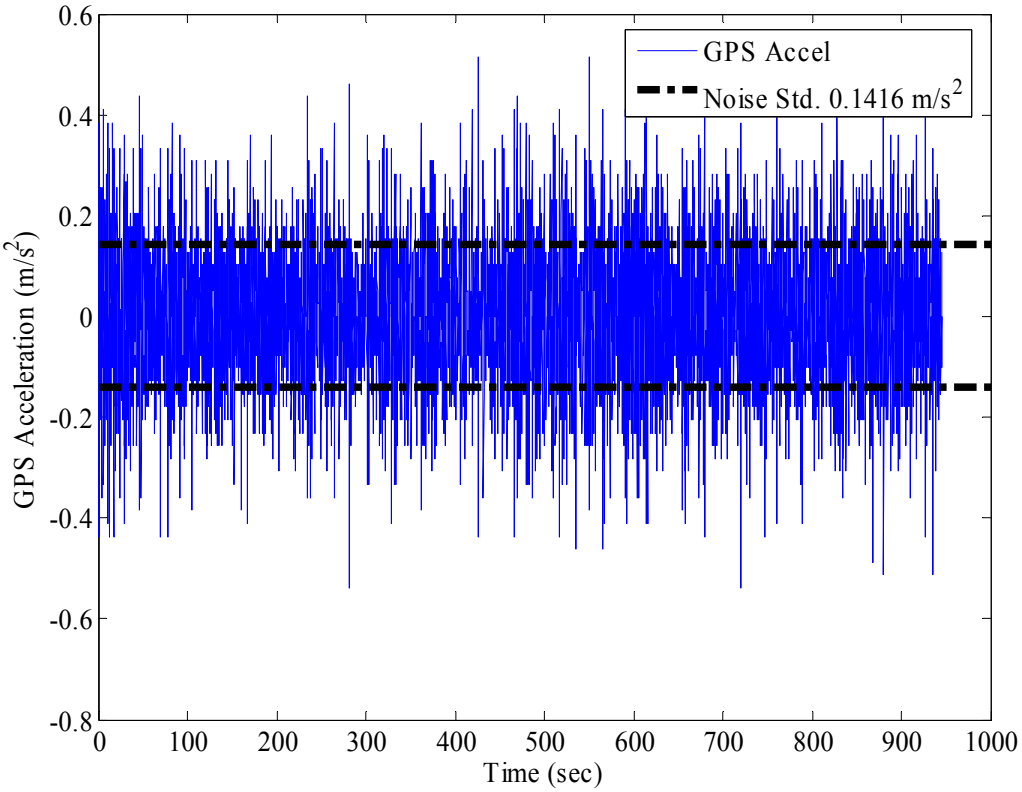

Figure 3.19. Static GPS Acceleration, Analyzed for One σ Bounds

This increase in noise characteristics will have an effect on the vehicle measurements and will be analyzed in more detail in the following chapter.

3.5 Modeling Conclusions

This chapter presents a more extensive and slightly more accurate longitudinal vehicle dynamic model compared to what was presented in Chapter 2. This new model contains additional dynamic effects that act on the vehicle, mainly inertias. The model is shown in simulation and a discussion of the differences between the model presented in

Chapter 2. The model is also compared to that in a commercial vehicle dynamics modeling package and showed good agreement. Analytical sensor models are presented and then applied to the vehicle simulations. Sensor noise was small when looking at high dynamic truck measurements but the noise had a large impact when analyzing small variations in velocity and acceleration.

The vehicle models presented capture similar dynamics with small differences in the overall vehicle behavior, with the most significant difference occurring in high dynamic situations. Sensor noise is shown to have a significant effect on what can be expected of measurements in real world tests, especially those which experience low dynamic excitation and will be analyzed more in depth in Chapter 4.

CHAPTER 4

IDENTIFICATION IN SIMULATION

4.1 Introduction

This chapter investigates, in simulation, the feasibility of identifying various vehicle parameters in the presence of sensor noise. First, identification algorithms are presented mathematically and are then applied to the vehicle models shown in Chapters 2&3. Simulated data is presented in a unique way to show the parameters to be identified and the noise on the measurements for two different models. Estimations are performed on the simulations with and without sensor noise. Finally, a sensitivity analysis of how noise affects the estimation accuracy is performed and conclusions are drawn based on the results.

4.2 Identification Background

There are several methods that can be used for identifying parameters such as Least Squares, Recursive Least Squares, and the Kalman Filter. These numerical techniques are based on determining the states that minimize a cost function [Stengel,

1994]. When the states are parameters of a mathematical model, this technique is commonly called parameter estimation.

Parameter estimation frequently uses a method that is based on the minimization of a quadratic cost function, known as Least Squares. This technique gets its name from the linear system defined by Equation 4.1.

$$z = Hx + n \qquad 4.1$$
$$= y + n$$

where:

z = Measurements

H = Observation matrix

x = Constant state vector

y = Error-free output vector

n = Error

The goal is to compute estimates of the states, contained in the vector denoted $\hat{x}$, from the measurements in z. This leads to Equation 4.2 below that describes the estimate of the output.

$$\hat{y} = H\hat{x} + v \qquad 4.2$$

where:

$\hat{y}$ = Estimates of the output

$\hat{x}$ = State estimate vector

v = Measurement Noise

The state residual error is defined by Equation 4.3 below.

$$\in_x = x - \hat{x} \tag{4.3}$$

The measurement residual error is defined by the following equation.

$$\in_z = z - \hat{z} \tag{4.4}$$

The state residual error, $\in_x$, represents the difference between the actual state and the estimated state, while the measurement residual, $\in_z$, represents the difference between the measured (ie: noisy) state and the (calculated) output. As previously mentioned, the least squares technique requires the minimization of a quadratic cost function. Ideally, a cost function would be defined such that the state residual error, $\in_x$, is minimized. However, this is not feasible as the true states are unknown, hence the need for an estimation algorithm. This cost function is therefore defined to contain terms of the measurements and the output vector, as shown in Equation 4.5. This equation can be solved without prior knowledge of the systems true states or noise values. Assuming that the noise is zero mean, minimizing the cost function in z also minimizes the state residual error.

$$\begin{aligned} J(z) &= \frac{1}{2} \in_z^T \in_z = \frac{1}{2}(z - \hat{y})^T (z - \hat{y}) \\ &= \frac{1}{2}(z - H\hat{x})^T (z - H\hat{x}) \end{aligned} \tag{4.5}$$

Equation 4.5 above can be simplified to the following shown in Equation 4.6.

$$J(z) = \frac{1}{2}(z^T z - z^T H\hat{x} - \hat{x}^T H^T z + \hat{x}^T H^T H\hat{x}) \tag{4.6}$$

To solve $J(z)$ for its minimum, the gradient of the cost function is set to equal zero, as in Equation 4.7.

$$\frac{\partial J(z)}{\partial \hat{x}} = (H^T H\hat{x} - H^T z)^T = 0 \tag{4.7}$$

This can be solved for $\hat{x}$ to result in the least square estimator, as shown below in Equation 4.8.

$$\hat{x} = (H^T H)^{-1} H^T z \tag{4.8}$$

In the solution for $\hat{x}$, the term $\left[H^T H\right]^{-1} H^T$ is called the pseudoinverse, which reduces to H^L as shown in Equation 4.9.

$$\hat{x} = H^L z \tag{4.9}$$

The derivation above is typically called Batch Least Squares which refers to the process being performed on a complete set of data. However on real systems, it becomes beneficial to perform real time estimates. The recursive least squares (RLS) algorithm is one that propagates, or calculates the estimates, through discrete time steps. It is possible

to append measurements to the measurement matrix as they are received and recalculate the least squares estimates. However, recursive least squares uses a more computationally efficient algorithm that uses the previous estimates as its starting point and propagates the estimates through time. The RLS equations are [Stengel, 1994]:

$$\hat{x}_k = \hat{x}_{k+1} + K_k(z_k - H_k\hat{x}_{k-1}) \tag{4.10}$$

$$K_k = P_{k-1}H_k^T(H_kP_{k-1}H_k^T + R_k)^{-1} \tag{4.11}$$

$$P_k = (P_{k-1}^{-1} + H_k^T R_k^{-1} H_k)^{-1} \tag{4.12}$$

Where:

$\hat{x}$ = State estimates

K_k = Recursive least squares gain matrix

P_k = State estimate covariance matrix

4.3 Estimation Modeling

It has been shown that least squares is a suitable and practical method to provide estimates for simple vehicle parameters [Bae, 2001]. Applying the longitudinal model from Chapter 3 to a least squares structure (Equation 4.13) results in the following model:

$$F_{Drive} = \begin{bmatrix} \ddot{x} & V^2 & 1 \end{bmatrix} \begin{bmatrix} \hat{m} \\ \hat{C}_{df} \\ \hat{F}_{rr} \end{bmatrix} \tag{4.13}$$

This satisfies the least squares form in Equation 4.2. In estimating the air drag and rolling resistance the individual components cannot be distinguished when the vehicle system is not sufficiently excited (i.e. when the vehicle travels at constant speed, which is similar to the operations performed by the trucks at NCAT). Therefore this necessitates a different estimation model form if the air drag and rolling resistance components are not distinguishable, which is shown in Equation 4.14 below.

$$F_{Drive} = \begin{bmatrix} \ddot{x} & 1 \end{bmatrix} \begin{bmatrix} \hat{m} \\ loss_{const} \end{bmatrix} \tag{4.14}$$

As the vehicle travels around the NCAT test track, it travels through turns at the east and west ends of the track. This correspondingly increases the longitudinal force on the trucks proportional to that of the slip angle and lateral forces generated by the tires as described in Section 2.4. This force is neglected in the estimation algorithm and will be lumped into the total losses. Thus, this force is not distinguished from the rolling resistance and air drag losses of the vehicle in the turns on the track.

Because system Model 1 contains three parameters to be estimated, plotting a 3-D representation of these parameters shows a planar spread of data, as shown in Figure 4.1.

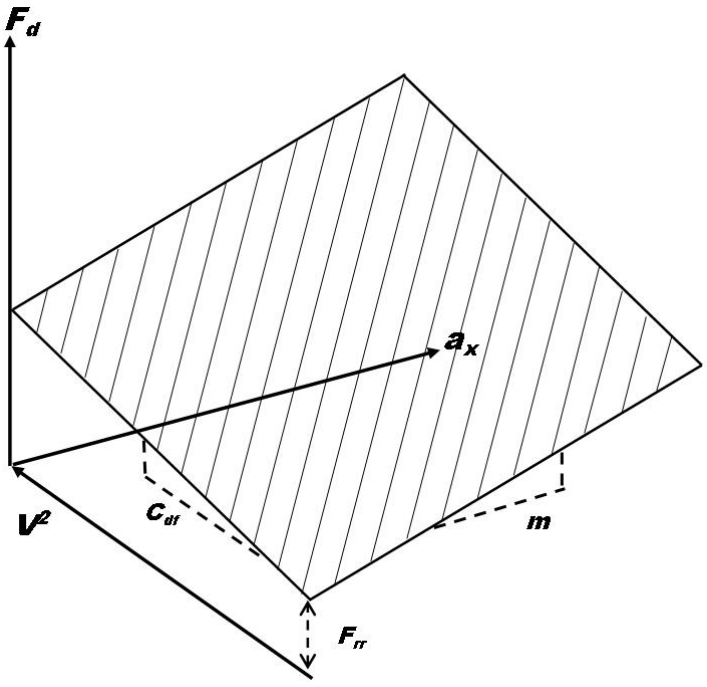

Figure 4.1. Representation of 3-D Data Plane (Model 1), Indicating of Mass, Air Drag, and Rolling Resistance Coefficients

The data for Model 2 can also be represented in a plot that reduced the plane of Model 1 to a line as shown in Figure 4.2.

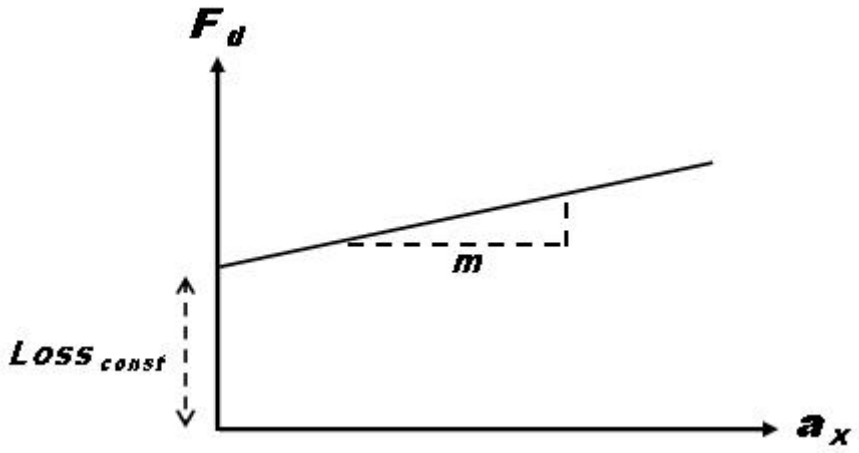

Figure 4.2. Representation of 2-D Data Line (Model 2), Indicating Coefficients of Mass and Losses

4.4 Mass and Loss Estimation In Simulation

4.4.1 Simulations and Data Treatment

Further investigation of system excitation and sensor accuracies were performed using a longitudinal tractor trailer simulation. Trucks were simulated accelerating from a stand-still as in Chapter 3.

Parameter estimates were performed using the simulation data to verify the ability to estimate parameters in simulation. Estimates of mass, air-drag, and rolling resistance values were obtained using the least squares technique and were accurate to the values used to produce the simulation data, given the noise free states. The following figure, 4.3, represents the three dimensional planar view of the simulated data without noise, showing the distinct forces in each gear as the vehicle speed increases and drive force decreases.

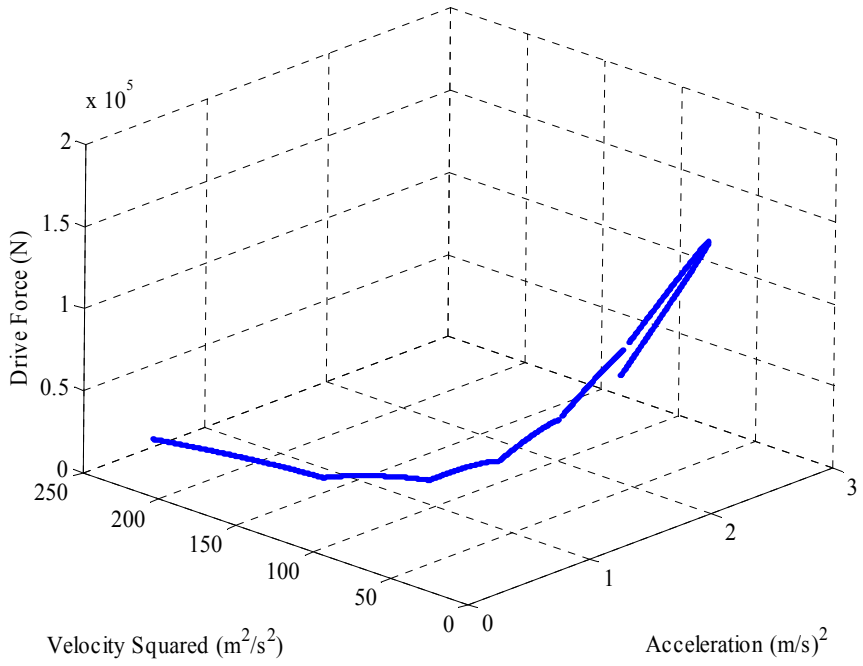

Figure 4.3. Longitudinal Acceleration Simulation in 3-D Format

The vehicle acceleration simulation provides a good range of drive forces, velocities, and accelerations on which to perform identification. Noisy signals were generated based on noise statistics found from static data tests performed in the trucks, as shown in Section 3.4. Using these noise values a simulation of the vehicle is performed with results shown in Figure 4.4.

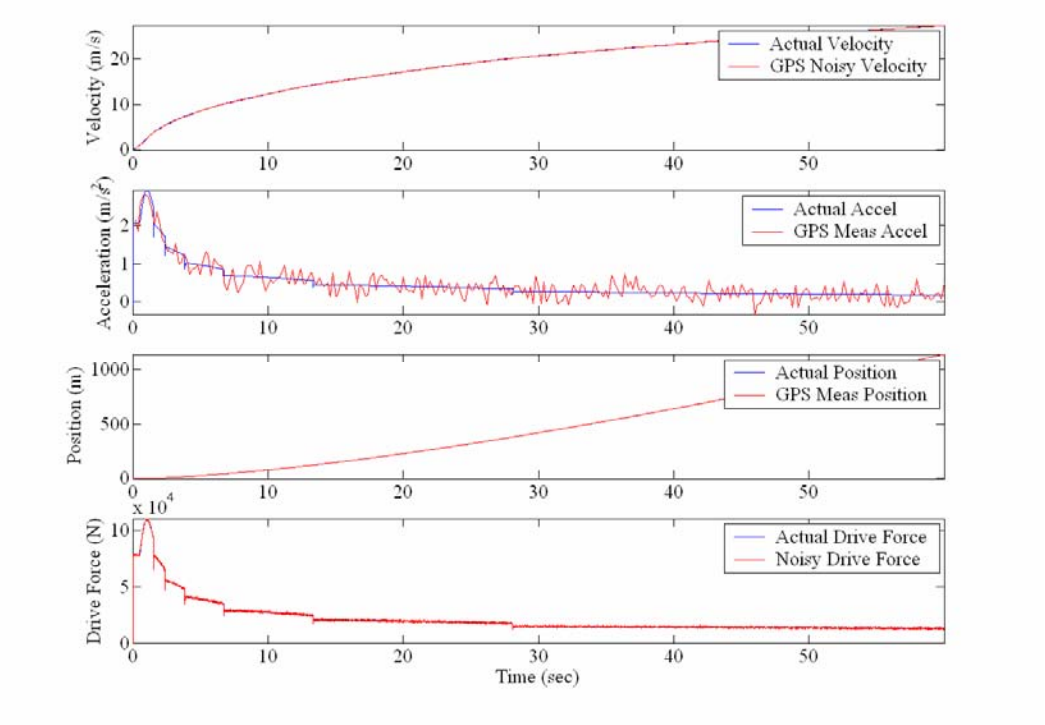

Figure 4.4. Noisy Longitudinal Acceleration Simulation Data for Identification

Reapplying the 3-view technique to the simulated noisy data in Figure 4.4 results in the plots shown in Figure 4.5. The background planes shown in the figure represent the planes upon which clean data would lie. This gives an indication in each view how the noise effects the measurement of each vehicle state.

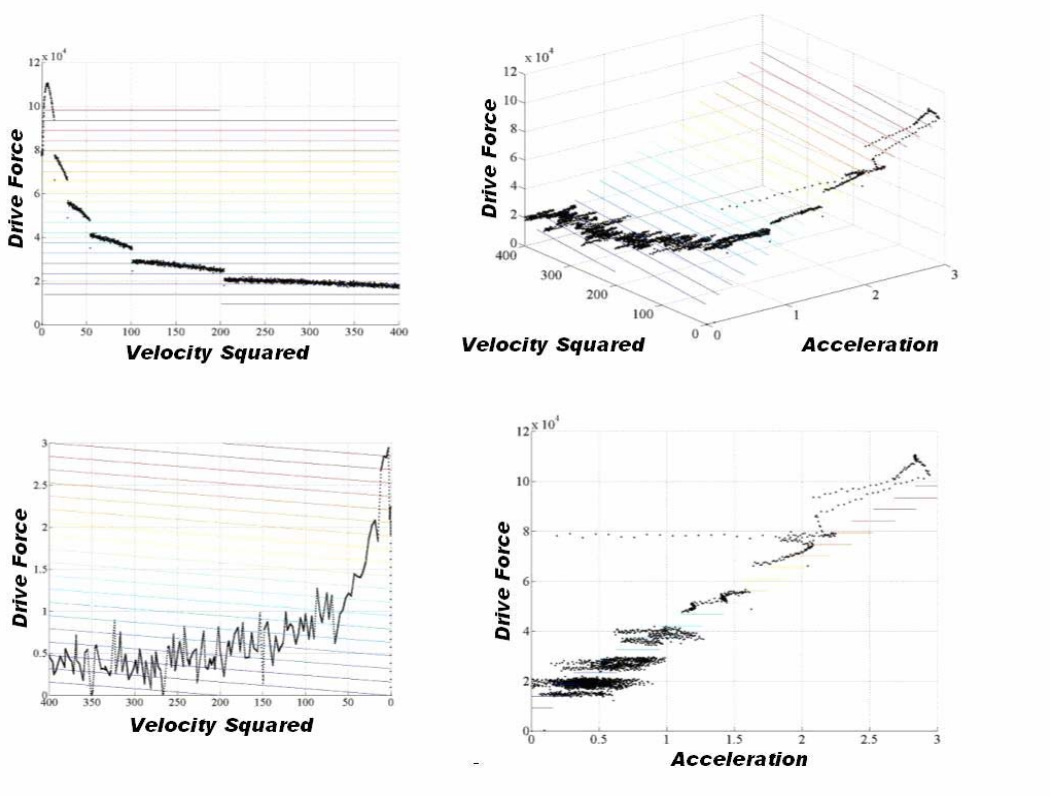

Figure 4.5. Noisy Longitudinal Acceleration Simulation, 3-D with Theoretical Data Plane Background

Re-plotting this data with background planes that represent the fits of Model 1 and Model 2 allows visualization of the effect the velocity squared term has on losses, as shown in Figure 4.6. The velocity squared term in Model 1 represents a significant slope difference in these planes and, therefore, model 2 is not valid for this condition where velocity contains significant excitation.

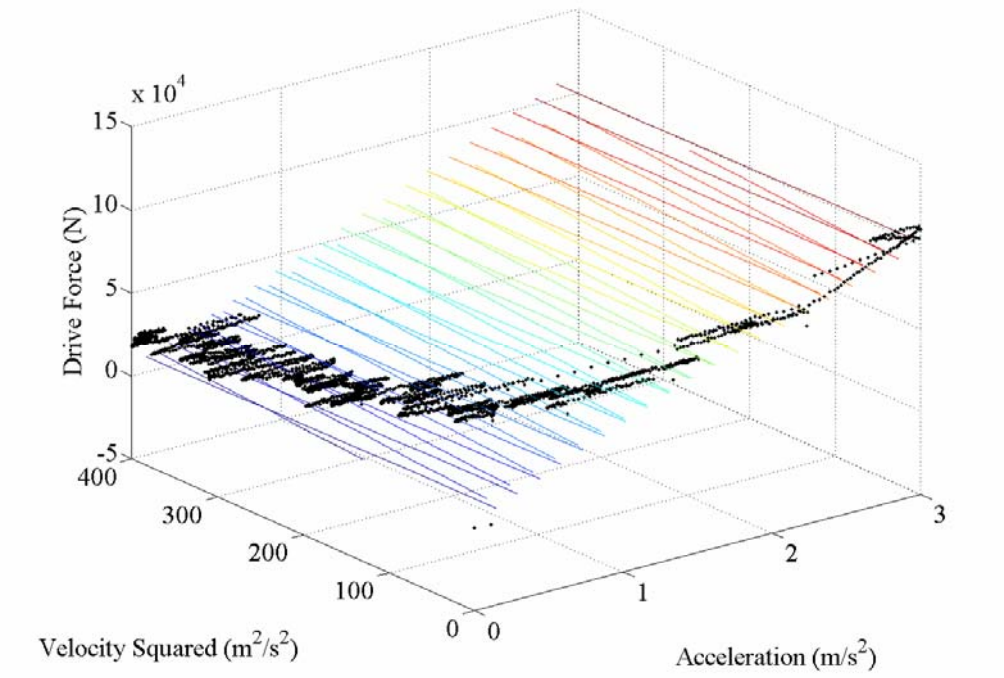

Figure 4.6. 3-D Planar Data Showing Background Planes Representing Model 1 and Model 2.

4.4.2 Investigating Sensor Noise in Estimations

Sensor noise was shown in Chapter 3 and in the previous section to have a significant effect on expected measurements in real world tests, especially those which experience low dynamic excitation. The heavy trucks at the NCAT facility drive repeated laps for extended periods which can present an opportunity to increase measurement accuracy by reducing noise through averaging repetitive measurements. This technique uses simulated vehicle measurements of a heavy truck driving repeated laps around the NCAT facility. This simulated noisy data of velocity and acceleration is taken at specific points on the track. These repeated data points can then be averaged, effectively reducing the random noise content. This creates a cleaner signal through averaging the random

noise at each point due to the characteristic that the noise is zero mean. Taking the data points from each lap and lining them up as a function of distance around the track removes process noise that would otherwise be introduced if averaging data that occurred at different points on the track.

Figure 4.7 and 4.8 show these simulated vehicle measurements in blue and the vehicle's true state in black. These noisy sensor signals can then be averaged at the points on the track to reduce noise level, as shown in red.

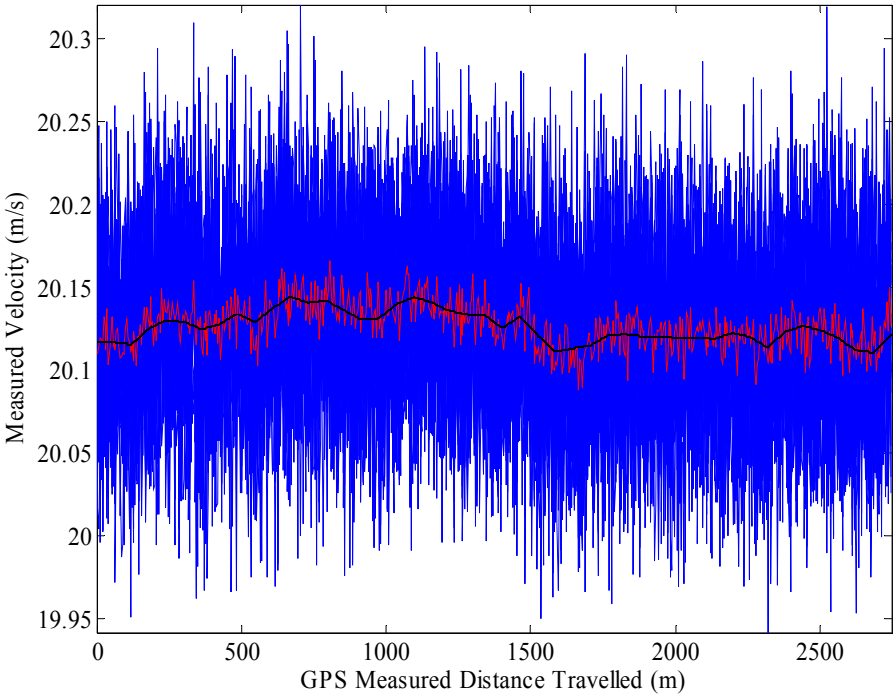

Figure 4.7. Averaging of GPS Measured Velocity

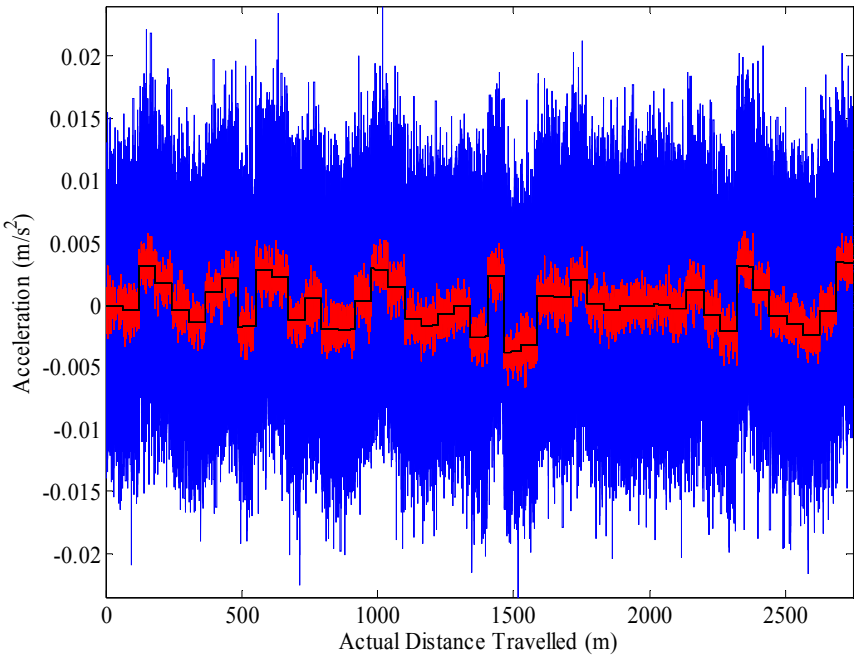

Figure 4.8. Averaging of Measured Acceleration

These averaged signals represent the confidence that can be had if repeated runs are created and measurements are averaged to filter noise. A specific analysis was performed to show the reduction in noise as more laps were repeated and averaged to reduce noise. Track simulations were performed to generate noisy data. This data was then averaged and a noise value over the true state was calculated. This noise value is plotted against the number of laps, or simulation loops, in Figure 4.9.

There is a clear trend reducing the noise as a function of laps whose data points were averaged. This empirical simulation has an analytical fit described in Equation 4.21 which is derived by using the propagation of uncertainty, shown in Equation 4.15.

$$\sigma_y = \sqrt{\left(\sum_{i=1}^{I} \frac{\partial y}{\partial x_i} \sigma_{xi} \right)^2} \qquad 4.15$$

The average signal is defined by Equation 4.16.

$$x_{ave} = \frac{1}{N} \sum_{i=1}^{N} x_i \qquad 4.16$$

Expanding the signal's average to include noise is shown in Equation 4.17.

$$x_{ave} = x_{true} + v_{ave} \qquad 4.17$$

The average noise is defined as follows.

$$v_{avg} = \sqrt{\left(\sum_{j=1}^{N} \frac{\partial x_{ave}}{\partial x_j} \sigma_x \right)^2} \qquad 4.18$$

The partial derivative of the average signal with respect to the signal is shown in Equation 4.19.

$$\frac{\partial x_{ave}}{\partial x_j} = \frac{1}{N} \qquad 4.19$$

Finally, the propagation or uncertainty is simplified to Equation 4.20.

$$v_{avg} = \sqrt{\sum_{j=1}^{N}\left(\frac{1}{N}\sigma_x\right)^2} = \sqrt{\frac{\sigma_x^{\,2}}{N}} \qquad 4.20$$

Equation 4.21 shows the analytical solutions that represents the decrease in the original noise, σ, as a function of number of laps.

$$\sigma_{ave} = \sqrt{\frac{\sigma^2}{\#\,laps}} \qquad 4.21$$

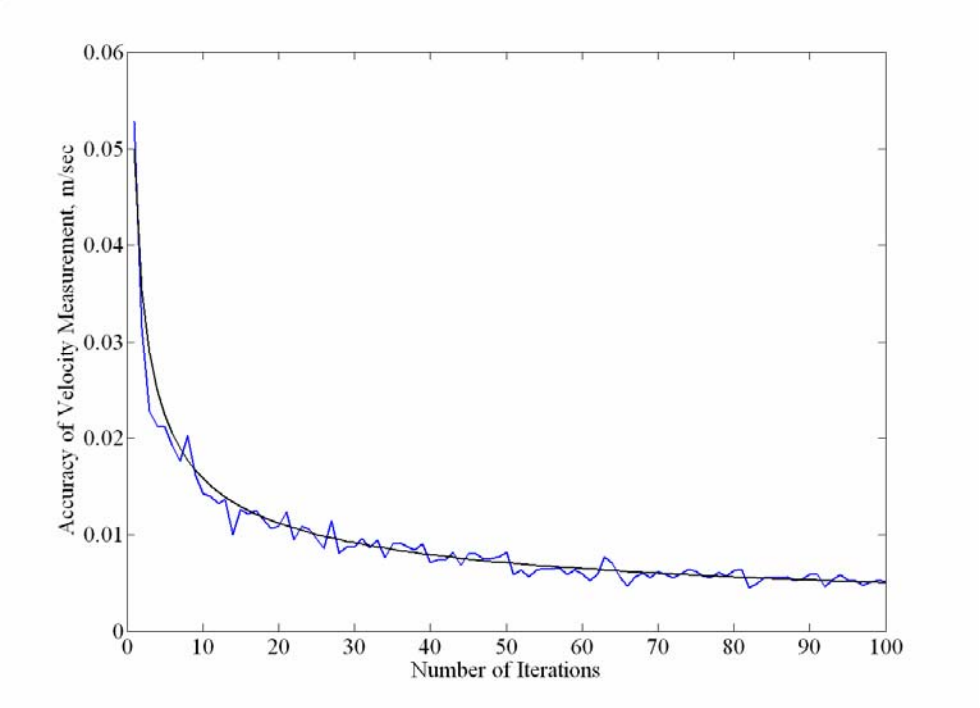

Figure 4.9. Plot of Accuracy vs. Number of Iterations, or Loops Performed

In the truck acceleration simulation, various levels of GPS velocity noise statistics can be injected into the system and estimations can be performed to evaluate how the

noise effects the estimation accuracy. The longitudinal simulation was looped many times, each time increasing the GPS velocity noise statistics. Errors on the state estimates were calculated and plotted for each loop so that accuracy as a function of noise can be analyzed. The results from estimating the three parameters of Model 1 are shown in Figure 4.10. These plots show a very distinct trend of a decrease in estimation accuracy with increasing noise in the velocity measurement. With perfect measurements, near perfect estimates can be obtained with slight inaccuracies due to the aliasing effect a 5Hz GPS measurement can have on the dynamics during the vehicle's gear changes. However, this effect could be reduced in with the inclusion of a Kalman filter technique using additional measurements or a recursive least squares with a forgetting factor [Vahidi, 2003]. Increasing the noise statistics just beyond the point of our known GPS accuracies, it is shown that estimate errors become large very quickly. The mass estimate shows the best performance of all three terms, and shows promise as it is of the most interest in vehicle estimation scheme.

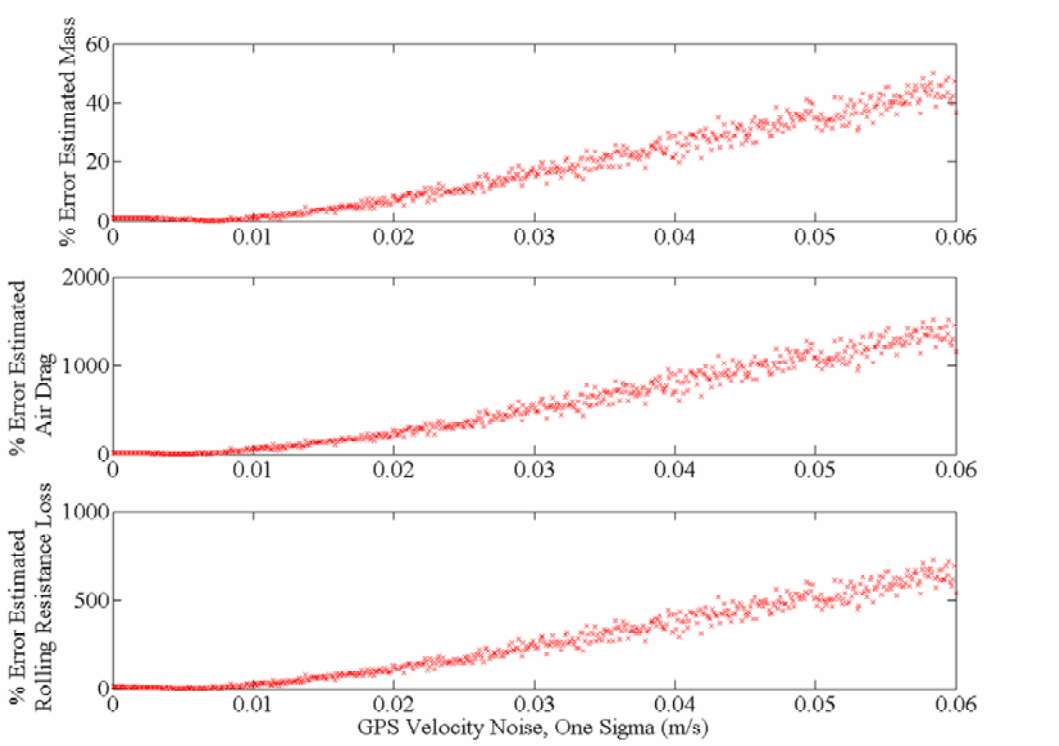

Figure 4.10. Estimation Accuracy as a Function of GPS Sensor Noise

A similar analysis can be performed using the longitudinal simulation without adding velocity noise but with noise on the drive force from the CAN data. Figure 4.11 shows how the noise on the force measurements affects errors in the state estimates. Again, the mass estimate is the most accurate and overall these estimates are less affected by noise on the force measurement than that on the other inertial sensors.

Figure 4.10 showed biased estimates with the inclusion of GPS noise. However, Figure 4.11 shows a zero-mean error is produced in the estimates with the inclusion of noise on the force measurement. The trends shown in Figure 4.11 also show that increasing the standard deviation on the drive force noise increases the standard deviation on the estimate error. Recalling the Equation 4.2, the GPS noise enters into the H

matrix, resulting in the growing errors in the state estimate matrix, $\hat{x}$. However, drive force noise enters into the systems estimate of the output, $\hat{y}$, which produces the zero mean error on the system, hence the zero mean trend in the state estimates $\hat{x}$.

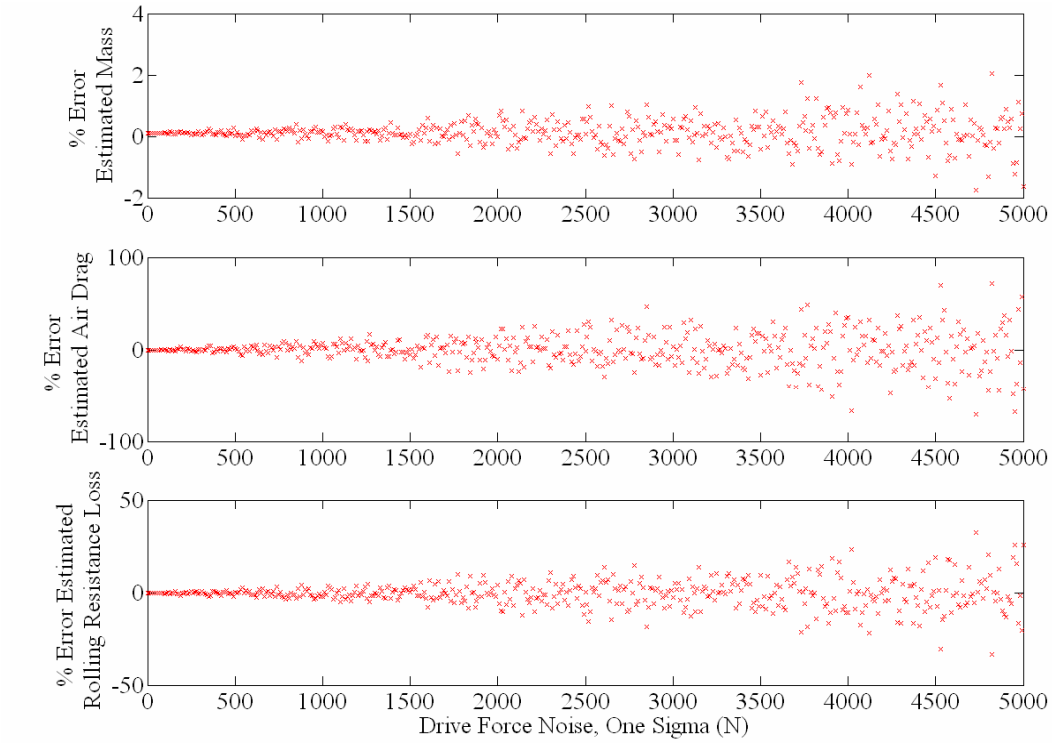

Figure 4.11. Estimation Accuracy as a Function of Longitudinal Force Noise

4.5 Conclusions

This chapter provides a foundation for performing estimation techniques in real vehicles by analyzing these techniques' performance in simulation. A background was given on various estimation techniques and these techniques were applied to the mathematical longitudinal vehicle dynamics models shown in the previous chapters. A unique visual data treatment was provided to show the effects of sensor noise and

modeling differences. Simulations results provide estimation results for longitudinal vehicle estimate techniques and simulate the expectations of their accuracy. Estimates were shown to vary significantly depending on the excitation of the system and the quality of measurements taken. This shows that the estimation variability should be taken into consideration for any long term vehicle estimation schemes.

CHAPTER 5

IDENTIFICATION ON TRACK

5.1 Introduction

This chapter investigates, using real experiments, the feasibility of identifying various vehicle parameters in the presence of sensor noise. A background on the test facility is given and road grade estimation around the facility is performed for future use in the parameter estimation data. Another technique for parameter estimation, known as Kalman Filtering, is presented and used to validate measurements from the on-board vehicle computer. Test data is presented in the format shown in previous chapters and parameter estimation is performed on driving, accelerating, and coasting data sets. Results are discussed regarding parameter estimation quality and further longitudinal loading data is analyzed for the benefit of studying road load and its effects at the NCAT facility.

5.2 NCAT Facility

The test bed for this research is an instrumented class 8 truck on Auburn University's National Center for Asphalt Technology (NCAT) oval test track. The NCAT

facility is a civil engineering research facility whose primary function is to perform accelerated asphalt testing and wear studies. This is accomplished on a 1.7 mile oval test track on which there are various types of asphalt test mixes and constructions. Five Freightliner trucks travel the track 16 hours per day in two shifts, five days a week. Historically the track has had two year test sessions with a small downtime between them for track reconstruction. These trucks give an opportunity to validate the accuracy, performance, and practicality of various estimation methods in heavy vehicles.

The track is broken into 200-foot sections of different pavement types and has near zero-grade through the straight-aways. This gives many different asphalt varieties to test on and also allows the verification, if necessary, of rolling resistance estimations using the straight-aways. Detailed information on each section of the track is monitored including rut depth and coefficient of friction. Additionally, influence of temperature and humidity on the data can be can be minimized by comparing data collected under similar testing conditions and/or analyzing existing weather station data.

Data collection hardware was installed on the trucks and is outlined in Appendix A. Figure 5.1 below shows GPS data recorded on the 1.7 mile oval test track and Figure 5.2 outlines the asphalt section layout.

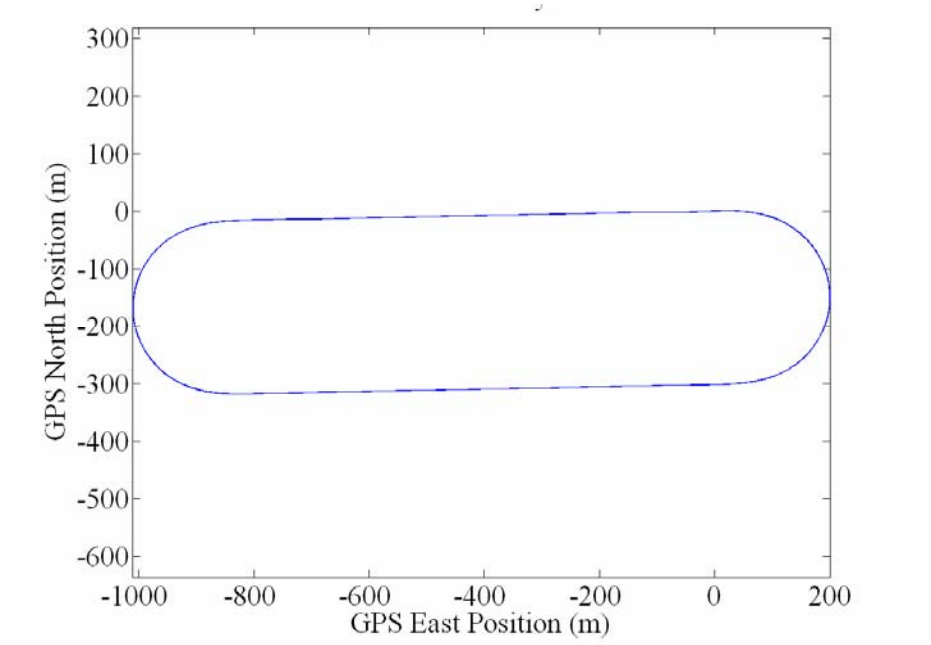

Figure 5.1. NCAT Test Track Layout from GPS

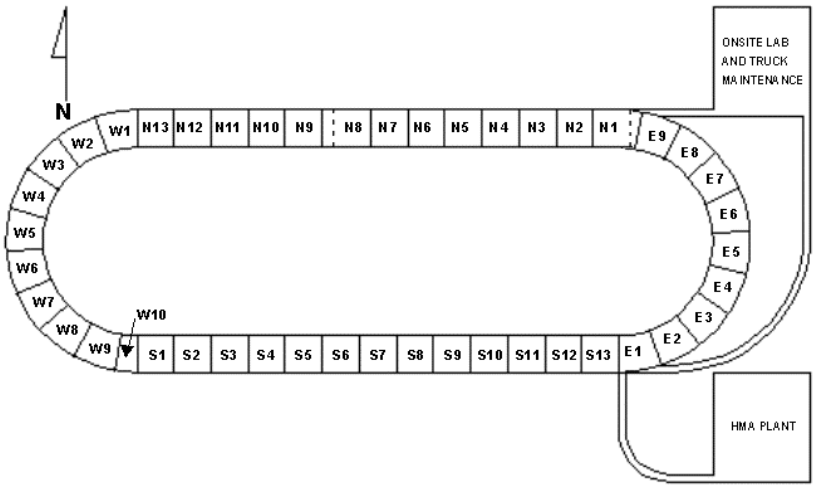

Figure 5.2. NCAT Test Track Asphalt Section Layout

5.3 Road Grade Estimation

It has been shown that a bias free estimate of road grade can be obtained by comparing the vertical and heading velocities measured by a single GPS unit [Bae, 2001;

Ryu, 2004]. This method is favorable over a dual antenna unit because it does not contain biases from vehicle pitch and it has no initialization bias. Vehicle bounce motions can however, be a factor in this type of measurement. Because the road grade dynamics are typically much slower than road dynamics that effect the vehicle's vertical suspension dynamics, vehicle bounce motions can be reasonably filtered using simple low pass filters or more complex techniques such as a Kalman Filter [Bae, 2001].

Using a single GPS antenna, a track profile can be generated using the lateral, longitudinal, and vertical measurements. The test track was designed and constructed with the goal of minimizing road grade. Results from test track elevation data in Section 2.6 shows that the track is quite level in the straight-aways, with approximately a 3 meter elevation difference between the north and south straight-aways, which results in a small slope through the turns. The estimation results using vertical and heading velocities are shown in Figure 5.3. Due to a relatively small data set and the type of GPS receiver used, a single antenna non-differential unit, the data is noisy and inaccurate during the straight-aways. The GPS unit's velocity accuracy is approximately 10 cm/s vertically and 5 cm/s horizontally. Because the slope estimation is a function of the inverse tangent of the ratio of vertical and horizontal velocities, the overall accuracy becomes a function of the magnitude of the heading velocity. Based on other research, more accurate receivers are needed for precise vehicle state measurements using GPS [Bevly, 2001]. Therefore, for this research, the elevation data provided by NCAT was deemed more accurate and therefore used later to remove road grade effects from the road load.

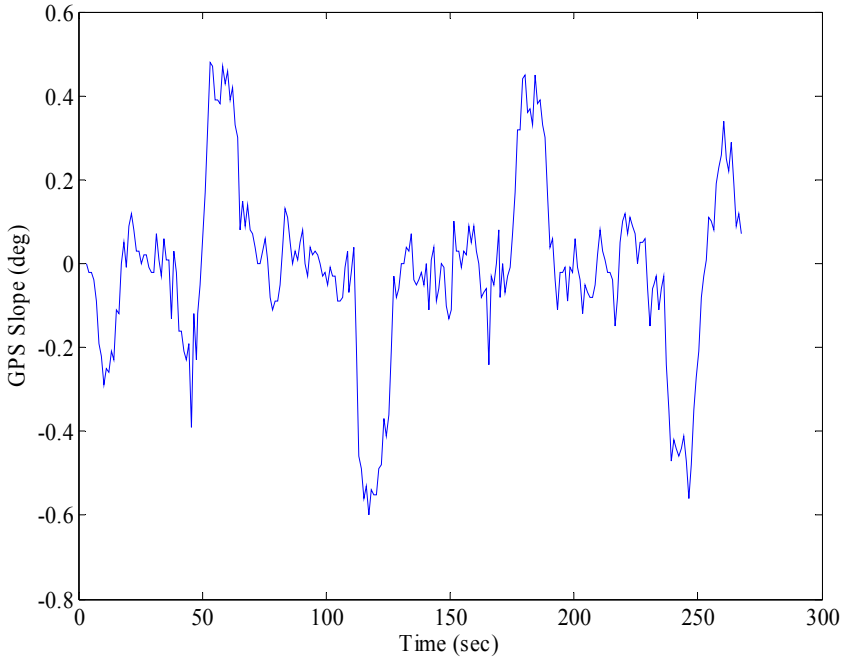

Figure 5.3. Road Grade Estimation

5.4 Kalman Filter Background

The Kalman Filter is a set of equations used in estimation, to provide an estimate of the states of a system by minimizing a quadratic cost function, like least squares presented in the previous chapter. A Kalman Filter minimizes the estimate error probability density which is a cost function subject to dynamic constraints [Stengel, 1994].

The Kalman Filter estimates the states of a system that are defined by the following discretized state-space dynamic equation, shown in Equation 5.1.

$$x_k = A_d x_{x-1} + B_d u_{k-1} + w_{k-1} \qquad 5.1$$

The system's output, y_k is as shown in Equation 5.2.

$$y_k = C_d x_k + v_k \tag{5.2}$$

The variables w and v represent process and measurement noise respectively. Their noise statistics are assumed to be zero mean, white, normally distributed, and uncorrelated as shown in Equations 5.3 through 5.9.

$$E[wv] = 0 \tag{5.3}$$

$$E[w] = 0 \tag{5.4}$$

$$E[v] = 0 \tag{5.5}$$

$$Q_d = E[ww^T] = \sigma_w^2 \tag{5.6}$$

$$R_d = E[vv^T] = \sigma_v^2 \tag{5.7}$$

$$w \sim N[0, Q_d] \tag{5.8}$$

$$v \sim N[0, R_d] \tag{5.9}$$

There are five distinct steps to the recursive algorithm that makes up the Kalman Filter, which are given in Equations 5.10 through 5.14. The first step of the Kalman Filter is to compute the state estimate extrapolation shown in Equation 5.10.

$$\hat{x}_{k+1}^{(-)} = A_d \hat{x}_k^{(+)} + B_d u_k \tag{5.10}$$

Along with the state estimate is the state error covariance matrix extrapolation shown in Equation 5.11.

$$P_{k+1}^{(-)} = A_d P_k^{(+)} A_d^T + Q_k \tag{5.11}$$

The next step of the Kalman Filter is to compute the filter gain, or Kalman gain, using the following equation.

$$L_k = P_k^{(-)} C_d^T \left[C_d P_k^{(-)} C_d^T + R_k \right]^{-1} \tag{5.12}$$

This gain is then used in a linear combination of $\hat{x}_k^{(-)}$ and a weighted difference between the actual measurement and a predicted measurement. This value of $\left(y_k - C_d \hat{x}_k^{(-)}\right)$ is known as the measurement innovation and is multiplied by the Kalman gain calculated in the previous step to produce the state estimate update as shown in Equation 5.13.

$$\hat{x}_k^{(+)} = \hat{x}_k^{(-)} + L_k \left(y_k - C_d \hat{x}_k^{(-)} \right) \tag{5.13}$$

Finally, the state error covariance matrix is updated using Equation 5.14.

$$P_k^{(+)} = \left(I - L_k C_d \right) P_k^{(-)} \tag{5.14}$$

If the measurement noise covariance matrix, R, goes to zero the Kalman Gain, L_k, approaches values of C_d^{-1}. In this limit, the actual measurement is trusted completely and the predicted measurement thrown out. If the state estimation error covariance, $P_k^{(-)}$,

approaches zero, the Kalman Gain approaches values of zero. If this occurs, the predicted measurement (state estimate) is trusted more.

5.5 Drive Force Estimation/CAN Data Verification

Engine torque is available on the controller area network (CAN) bus of the Freightliner trucks used in this research. It is however, an estimate of torque that is calculated by the engine computer. Because the accuracy of the CAN force data is unknown, adding additional sensors and using a Kalman filter allows the estimation of a clean or more accurate drive force as well as verifying the CAN measurement's quality.

For this more accurate drive force estimation, the CAN drive force, longitudinal acceleration, and vehicle mass must all be known. Because mass is typically unknown or would vary significantly in use, this wouldn't have applications in real world vehicle systems. However, for the sake of this research, using the known mass will allow the quality of the CAN data to be verified using a preliminary data set.

The engine force can be described by Equation 5.15.

$$F_{engine} = \frac{\tau_{engine} N_{transmission} N_{final\ drive} \varepsilon_{mechanical}}{R_{tire}} \quad 5.15$$

Because the trucks have a manual transmission and use only one transmission gear for these verification experiments the reductions, N_{total}, shown in Equation 5.16 can be found from data sheets or empirically.

$$V_{velocity} = \omega_{engine} N_{total} C_{circumfere\ nce} \tag{5.16}$$

The tire radius in the above equation is 0.5311m as equipped from the manufacturer. Therefore using vehicle speed and engine speed from the CAN, the total reduction N_{total} was determined to be 3.904 using Equation 5.16.

Using a Kalman filter, a cleaner, higher fidelity drive force can be estimated for later use in the vehicle parameter estimation schemes. The Kalman filter model used is arranged as shown in Equations 5.17 through 5.18.

$$\begin{aligned} \dot{F} &= 0 + w \\ y &= Cx + v \end{aligned} \tag{5.17}$$

$$\begin{aligned} \left[\dot{F}orce_{long}\right] &= [0]\left[Force_{long}\right] \\ \begin{bmatrix} measured\_Force_{long} \\ mass * accel\_x \end{bmatrix} &= \begin{bmatrix} 1 \\ 1 \end{bmatrix}\left[Force_{long}\right] \end{aligned} \tag{5.18}$$

As shown in Equation 5.17 above, the outputs are measured CAN drive force and measured longitudinal acceleration, and the estimated state is drive force.

The longitudinal acceleration measurement in the system can be first run through a Kinematic Kalman filter to remove the sensor bias using GPS velocity [Bevly, 2001]. An understanding of the noise statistics for both the CAN drive force and the longitudinal

accelerometer are necessary to obtain good force estimates. The CAN drive force noise statistics used for the Kalman Filter are chosen in simulation to obtain good quality estimates and filtering of the signal. The accelerometer noise statistics were obtained from the static tests discussed in Section 3.4.

The Kalman filter noise statistics are normally distrubted zero mean with variance summarized in Equations 5.19 and 5.20.

$$v \rightarrow N\left(\begin{bmatrix}0\\0\end{bmatrix},\begin{bmatrix}\sigma_{force\_meas}^{\ 2} & 0\\ 0 & m^2\sigma_{accel\_x}^{\ 2}\end{bmatrix}\right) \tag{5.19}$$

$$\begin{aligned}\sigma_{force\_meas} &= 100 Newtons\\ \sigma_{accel\_x} &= 0.022g\end{aligned} \tag{5.20}$$

Figure 5.4 shows the results of the Kalman Filter drive force estimate compared with the actual measurement on the CAN bus from the engine computer. The noise covariance for the sensors and initial uncertainties were chosen to give good estimator performance without effecting the higher dynamics of the data. As seen in Figure 5.4 the CAN force estimate does not vary significantly from the measured force, which indicates the force estimate from the engine computer is fairly accurate. It may, however, be possible to increase the accuracy of the force estimate with a higher precision accelerometer. However, from this experiment, the raw force measurement from the engine computer was deemed sufficient for the following estimation schemes in this thesis.

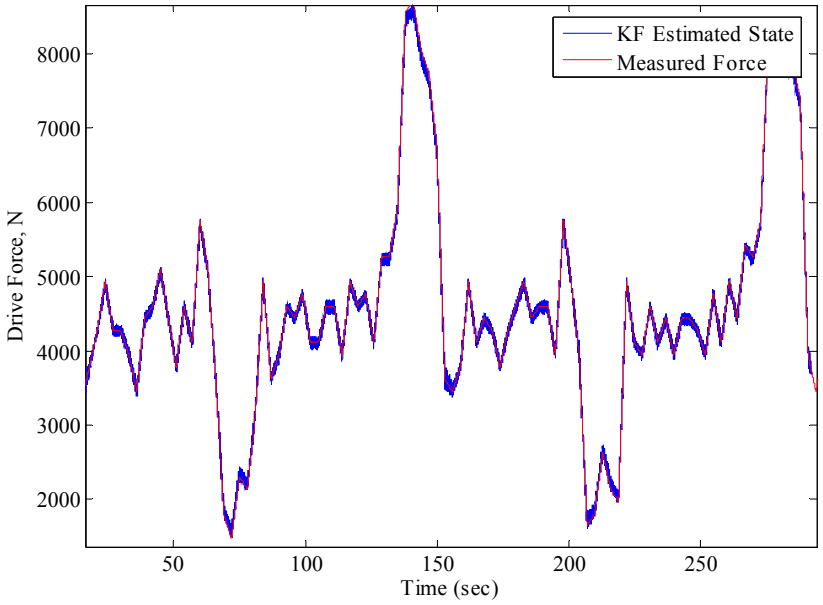

Figure 5.4. Measured and Estimated Longitudinal Drive Force

5.6 Test Data Estimation

5.6.1 Data Treatment

Truck data was sampled during a normal shift, where the trucks drive the track at a 45 mph target speed under the action of the vehicle's cruise controller. Very long sessions of data of up to 24 hours were taken and a sample of this data is shown in Figure 5.5. Lap repetitions are clearly shown by the test data, where approximately fifty laps of the trucks were sampled in this test, shown below.

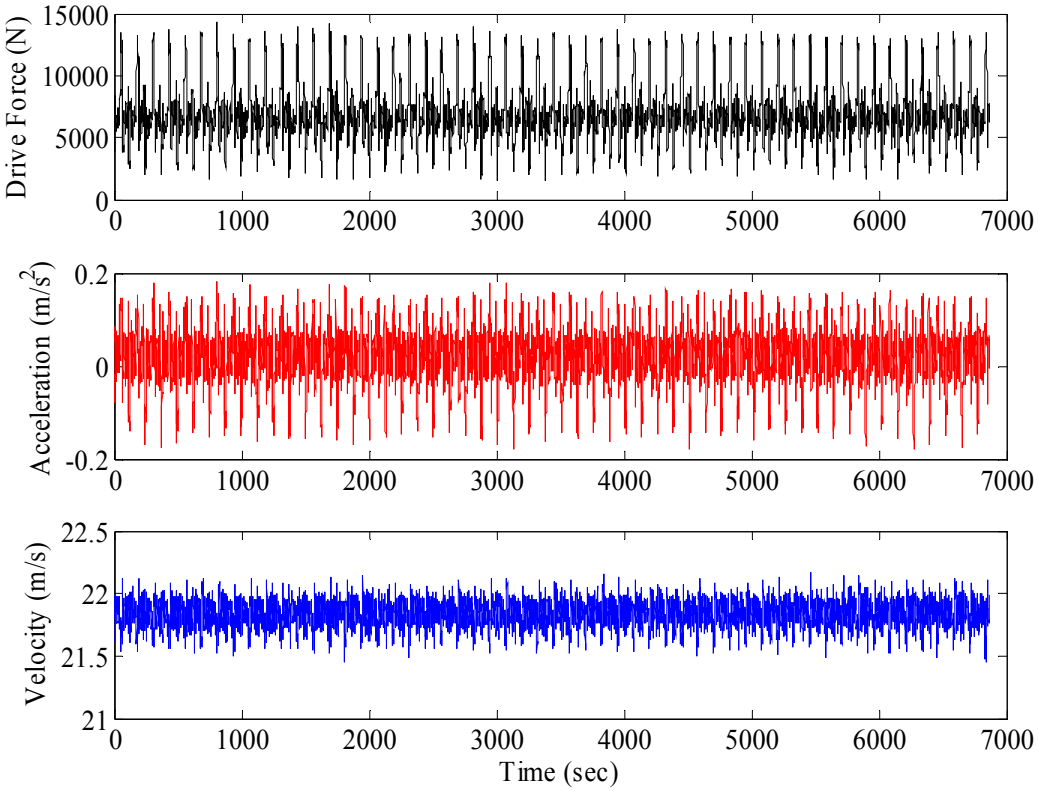

Figure 5.5. Truck Test Data

Applying the data shown above to the 3-view format first presented in Section 4.3, allows for the visualization of the quality of the data. The top right plot of Figure 5.6 shows the extended track session data plotted in 3-view, where the noise free data would lie on a plane. Viewing this three dimensional data from each side of the plot shows specific information about various parameters and the excitation in those parameters. The upper left hand plot shows the excitation in the air drag parameter to be identified. Ideally, this plot would yield a line, given significant excitation in the parameter and noise free measurements. The lower right hand plot shows the excitation and noise in the mass parameter. It too would ideally yield a line, whose slope would be the mass of the

vehicle. Finally the lower left hand plot shows a view of overall excitation in terms of velocity and acceleration and should have a slope of the air drag coefficient divided by the vehicle mass, with an offset of constant losses.

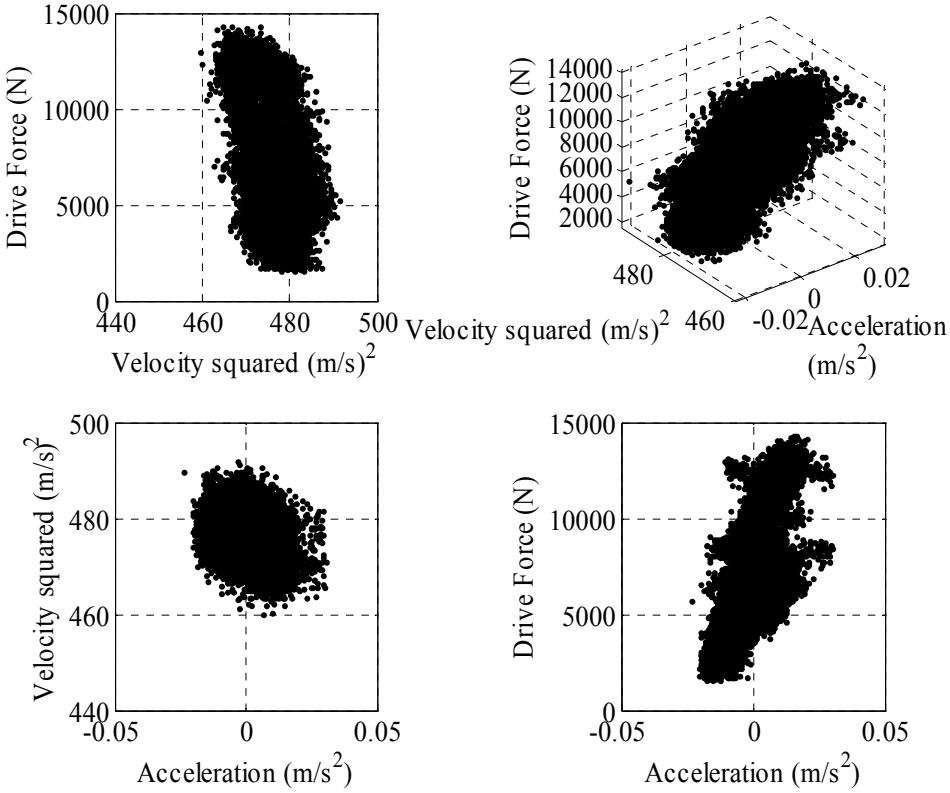

Figure 5.6. Truck Test Data, 3-D Representation

The figure above visually shows the magnitude of the noise on the sensors and how they corrupt the shape of the line to be estimated. Figure 5.7 below shows a closer view of what lies in the lower right hand plot of the figure above. The slope of a linear data fit of this figure would represent the mass of the truck. Again, noise has a distinct effect in the clarity of any linear fit that may be applied to this data, resulting in poor mass estimates.

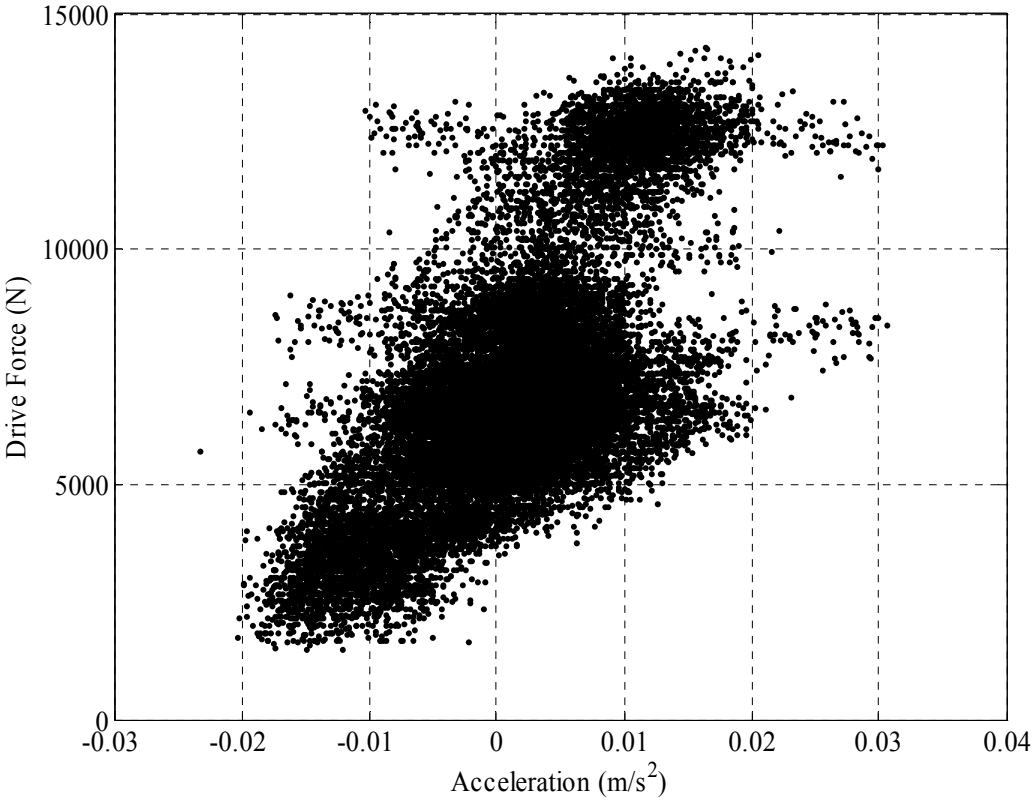

Figure 5.7. Truck Test Data, 2-D Representation

5.6.2 Identification of Sampled Data

Using both Models 1 & 2 as detailed in Section 4.3, least squares parameter identification was performed on the experimental truck data. These models are again shown in Equations 5.21 and 5.22.

$$\text{Model 1:} \qquad F_{Drive} = \begin{bmatrix} \ddot{x} & V^2 & 1 \end{bmatrix} \begin{bmatrix} \hat{m} \\ \hat{C}_{df} \\ \hat{F}_{rr} \end{bmatrix} \tag{5.21}$$

$$\text{Model 2:} \qquad F_{Drive} = \begin{bmatrix} \ddot{x} & 1 \end{bmatrix} \begin{bmatrix} \hat{m} \\ loss_{const} \end{bmatrix} \tag{5.22}$$

The results using model 1 for identification showed very poor estimates (>50%) of mass, air drag, and rolling resistance/constant losses. Performing a fit of Model 2 to the truck data resulted in a reasonable quality fit with approximately 10% error on the mass estimate and 10% error on the constant losses, when compared to known values.

This accuracy can be attributed to the simple linear model and the abundant amounts of data which least squares can average the noise effects. The equivalent results of doing the least squares fit can be plotted as a linear fit of the data shown in Figure 5.7 above. The results are shown in Figure 5.8, where the slope represents the mass parameter and the y intercept represents the constant losses.

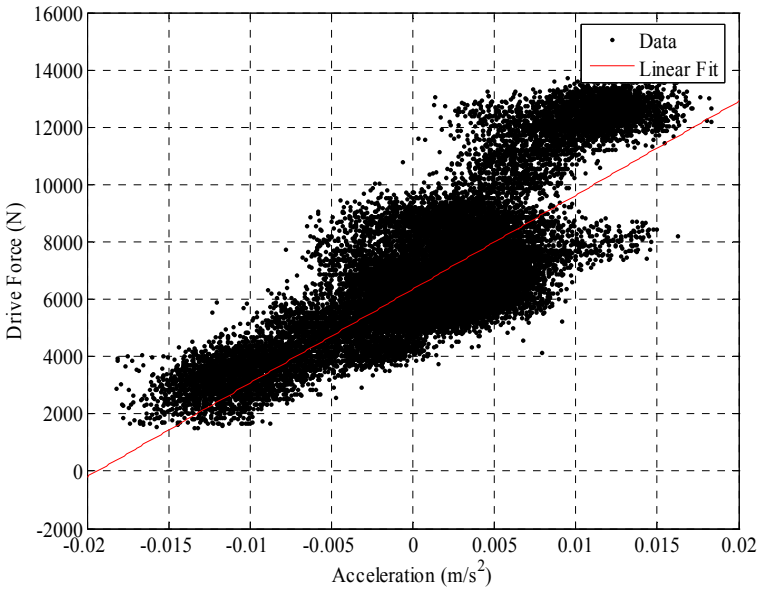

Figure 5.8. Truck Test Data, 2-D Representation with Linear Fit

Similar analysis can be performed on acceleration data taken on the trucks at the NCAT facility. The data shown in Figure 5.9 was taken during a truck accelerating at near full capability to NCAT track speed.

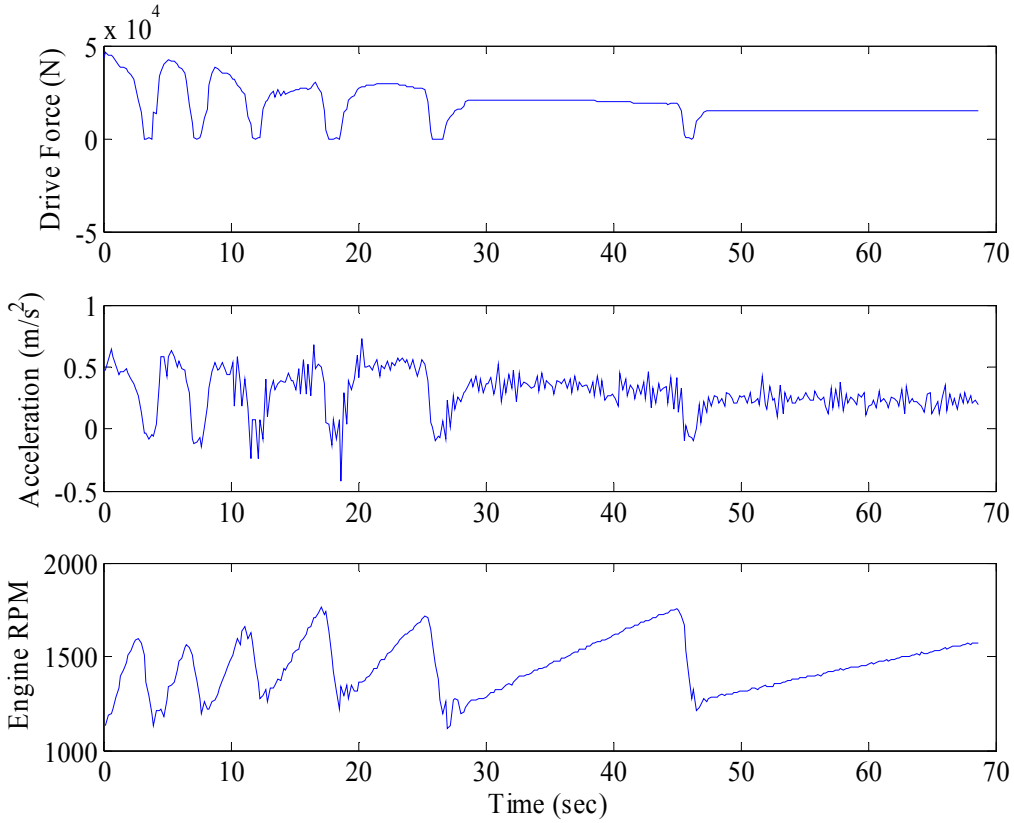

Figure 5.9. Truck Test Data, Acceleration

As with the regular driving data, the results for Model 1 show poor agreement with that of known values. However, Model 2 shows again, reasonable agreement with mass error of 15% and constant loss values of approximately 15%. This again can be attributed to using the simpler model, as shown in Figure 5.10 below.

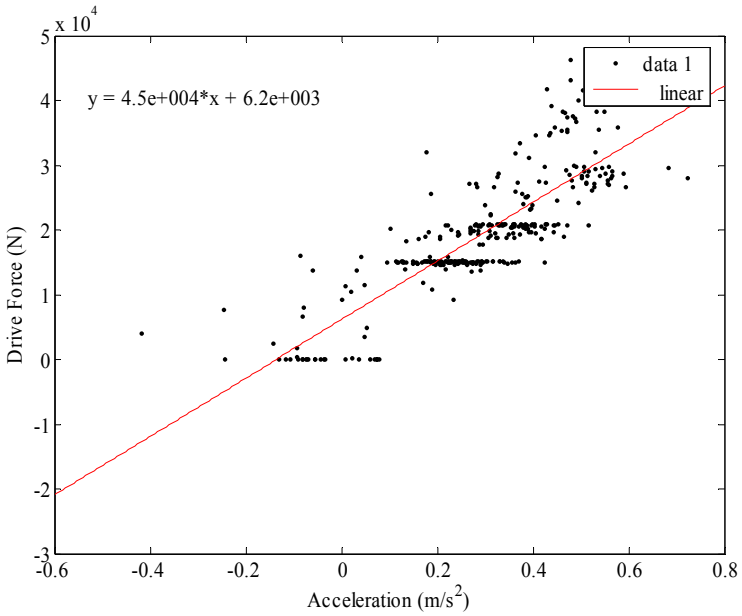

Figure 5.10. Truck Acceleration Test Data with Linear Fit

5.7 Test Data Road Load Results

Data was taken with the intention of analyzing the total road load on the vehicle as they travel the NCAT test track. Interest in studying the individual asphalt sections for their effect on fuel economy has led to the analysis of longitudinal load as a function of track position. Data in Figure 5.11 shows the applied drive force of the trucks in 3-view as a function of track position. The plane indicated in red represents the average percent load, while red circles indicate the location of changes in the asphalt sections.

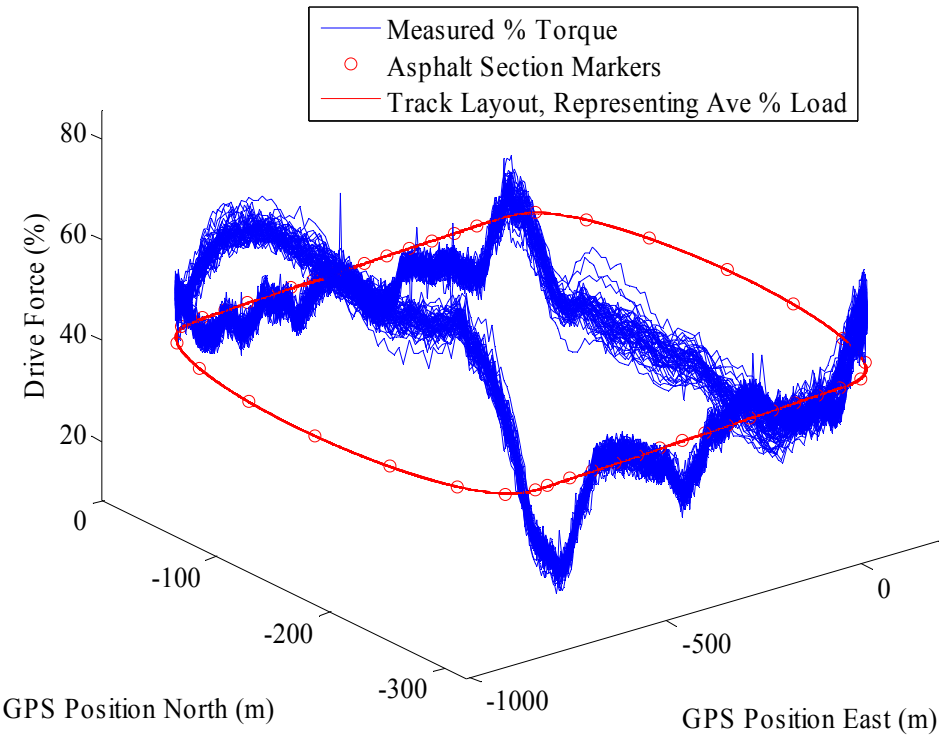

Figure 5.11. Uncorrected Road Load Measurements

To accurately analyze the truck data, the exact location of the GPS antenna must be taken into account. The GPS antenna is mounted just behind the roof of the truck's cab so an algorithm must be written to translate this measurement to the vehicles longitudinal center. It is also necessary to consider the trucks length in any analysis as data is sampled where the truck is passing over asphalt transitions and is therefore on two sections at one time. This data that has truck measurements on two surfaces should not be considered when analyzing average road load per section. Figure 5.12 below compensates for both GPS antenna offset and truck length and calculates an average longitudinal load for each asphalt section, shown in black. Figure 5.13 shows only the averaged road load per section for more clarity.

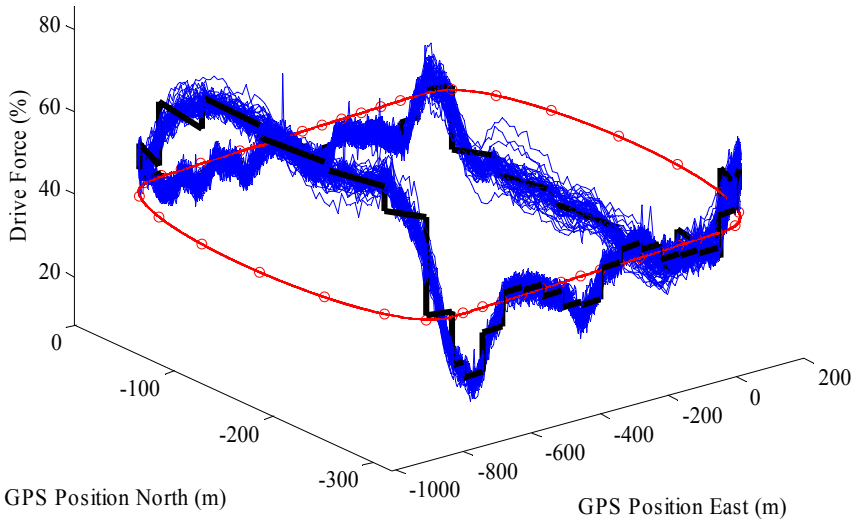

Figure 5.12. Road Load Measurements with Section Averages

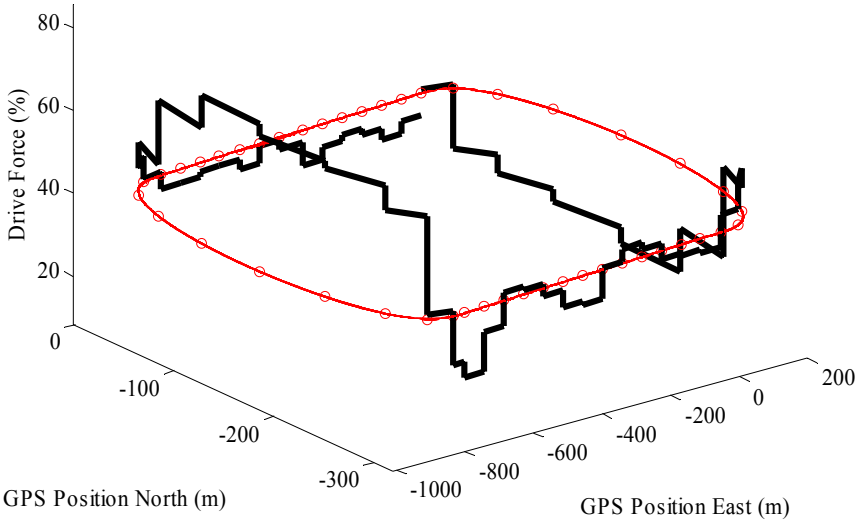

Figure 5.13. Road Load Averages by Section

Road load is impacted by the road slope as discussed in Section 2.6. As the vehicle travels the track the cruise controller varies the engine's torque, or drive force in an attempt to maintain a constant vehicle speed. Using the track elevation data presented in

Section 2.6, a road grade for each section is computed, and a corresponding longitudinal force is calculated based on the known vehicle mass during the experiments. Figure 5.14 shows the average longitudinal load per asphalt section after the force due to the road grade is removed. As is shown, the average loading deviates from the raw measurements, indicating the significance road grade has on the trucks, even at such small amplitudes as the NCAT test track.

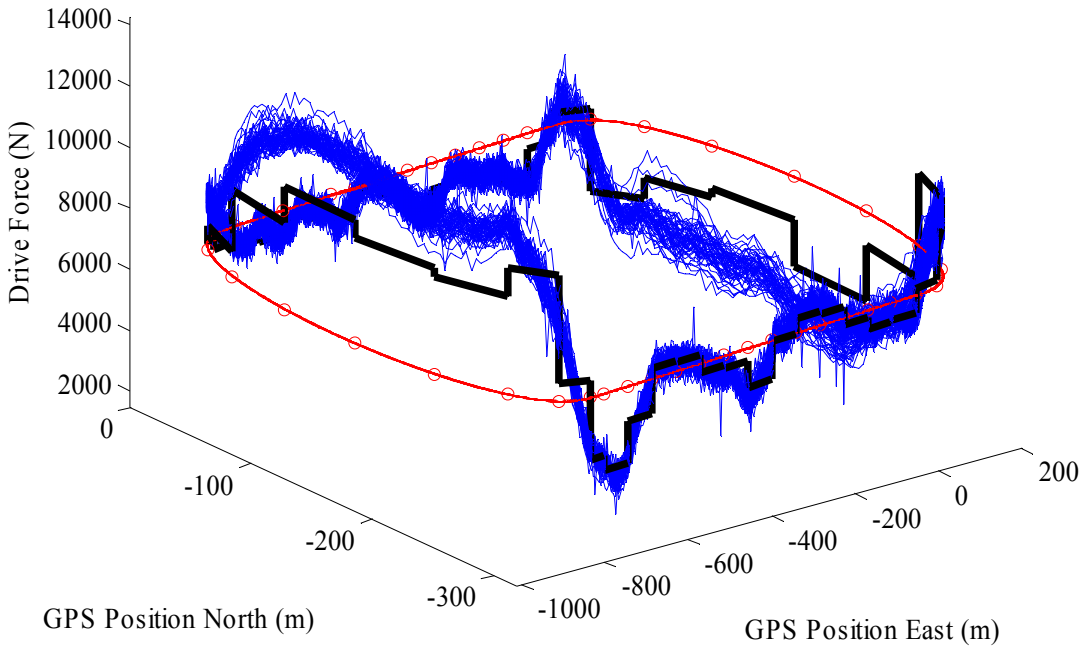

Figure 5.14. Corrected Road Load Measurements and Averages

Figure 5.15 compares the original averaged road load to the road load shown previously in Figure 5.13 where the forces due to slope are removed. The load shows small differences on the track's straight sections, as would be expected with a quite flat surface.

However, the uphill climb through the west end shows reduced loading when the slope is removed. The opposite effect happens in the east end of the track, where the vehicle travels on a downhill slope to the north side of the track. This corrected force represents an estimate of the magnitude of the sum of the losses due to the air drag, rolling resistance, and driveline of the vehicle.

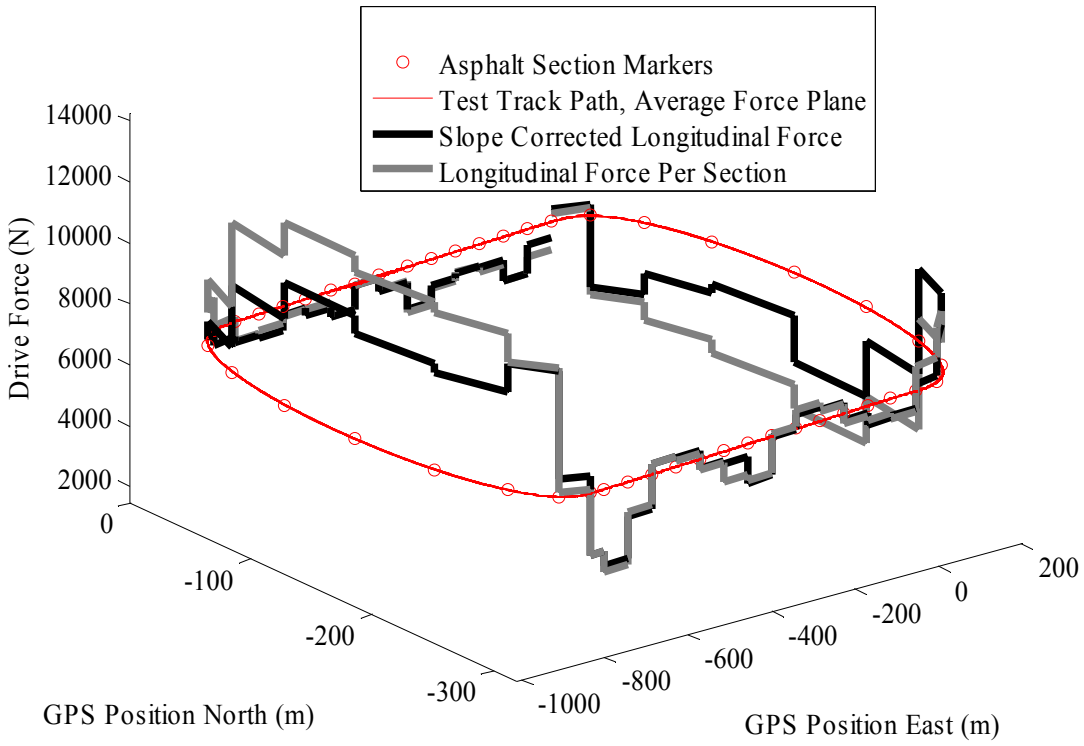

Figure 5.15. Slope Corrected Road Load Comparison

Figure 5.16 shows the magnitudes of both the averaged measurements and the slope corrected measurements as a function of track surface. The force due to the slope of the road is also shown.

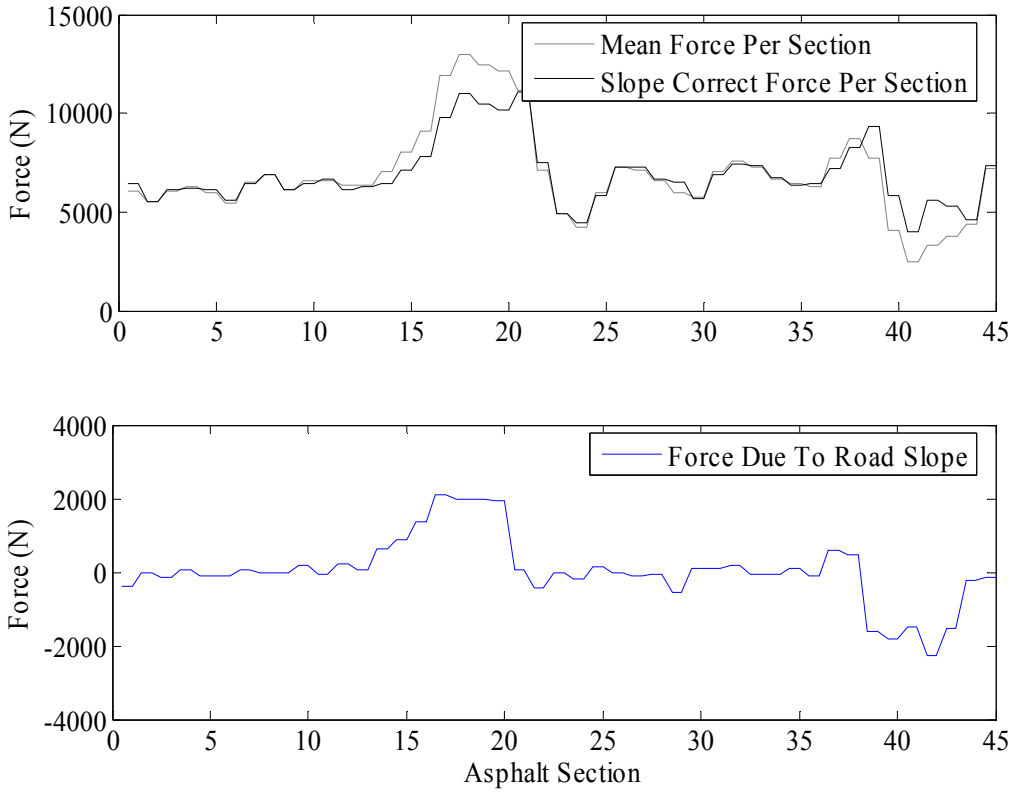

Figure 5.16. Road Load and Asphalt Sections

Analyzing the road load results shows the impact the road grade has on the vehicle loading around the track. Removing the road grade from the force measurement should show the magnitude of the remaining losses in the vehicle. This however does not explain trends seen in the curves, where the correct road load values are increased over the average in the west end turn, and decreased over average in the east curve. In other words, the results show increased losses in the west curve and decreased losses in the east curve. This trend in the plot actually has the behavior that the road grade in the turns was underestimated which would indicate that the accuracy of the survey data is suspect.

However, this is not likely the case, as the average slope based on the elevation change between the north and south ends and the radius of the turn supports the average slope seen in the corners. This data can be verified in the future by taking dedicated GPS vertical measurements as discussed in Section 5.3. The irregularity in the force could also be due to a south wind. To account for the differences seen in the force, which are approximately 2000N, would require a 10.6 m/s (23.7 mph) wind speed. This wind would also have to remain fairly constant due to the repeatability of the data over the 4 hour test session. This is possible and should be considered in future tests and may require additional sensors on the vehicle, such as dynamic pressure sensors. The average force irregularity could also be partially due to the behavior of the truck's electronic fuel and cruise controller behavior and would require adding cruise controller dynamics to better validate the behavior of the truck's controller.

Figure 5.17 shows the road load and asphalt roughness data collected at the test track. The middle plot represnts asphalt roughness, starting at section N1, in the Internation Roughness Index (IRI) scale. The IRI value is representative of large scale irregularities which are typically described as those felt in the vehicle. The bottom plot represents the Mean Texture Depth (MTD), which is shorter wavelength irregularities more commonly heard in the vehicle. When comparing the roughness data with the road force data no distinct relation can be shown with either macro or micro texture, which also doesn't account for the large road force trends seen in the trucks.

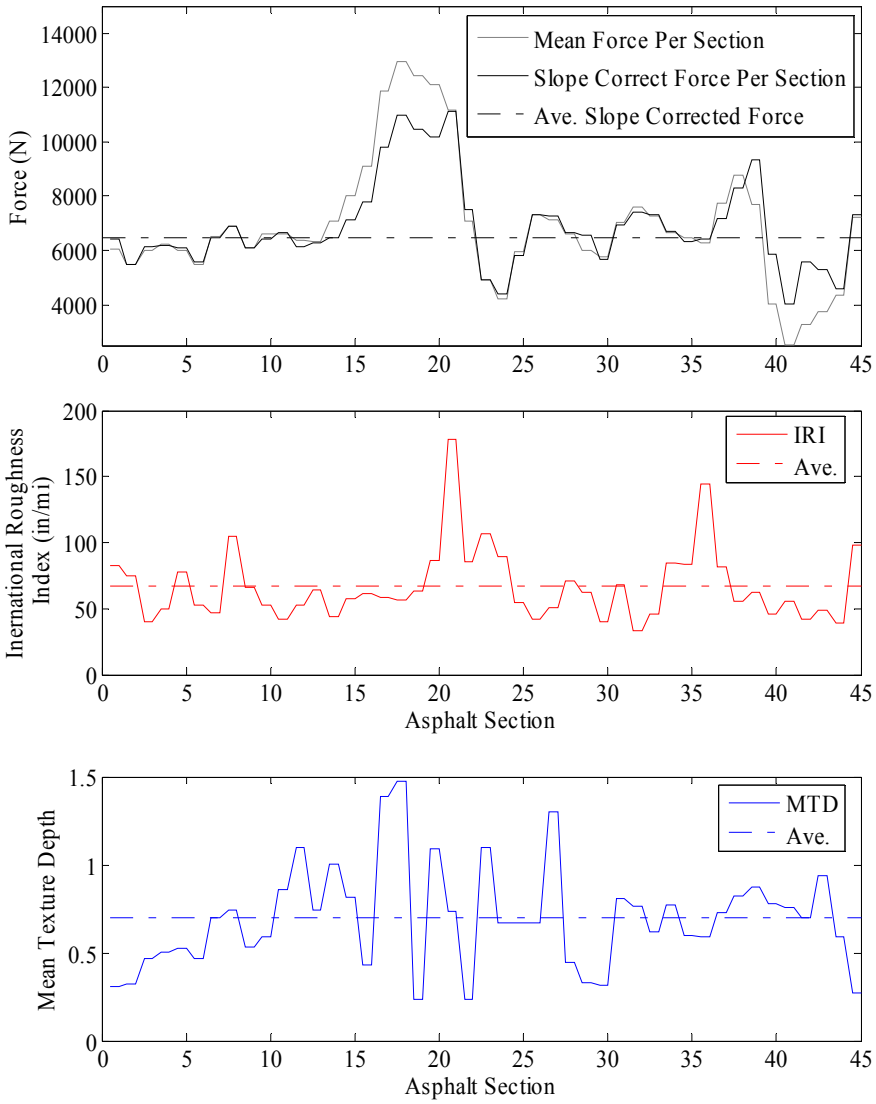

Figure 5.17. Road Load and Asphalt Roughness

5.8 Conclusions

This chapter has presented an overview of the test bed and experimental testing of the methods proposed in this thesis. A new estimation technique was presented and used

to verify unknown measurements available on the trucks. This measurement was then used in combination with others to measure the trucks vehicle dynamics under various tests. This data was used to estimate heavy truck parameters and a discussion of the results is given. Much inaccuracy in the estimation results was seen due to various reasons, including lack of dynamic excitation and sensor noise and accuracy.

The estimation results provided poor estimates in the experimental data, except when applying the simplest of fits. Recall that Chapter 4 showed under adequate excitation, the accuracy of estimating parameters in the presence of sensor noise. In the estimation performed in this chapter, the excitation levels were consistently low. In the case of the acceleration and deceleration experiments, the amount of data points available were not adequate to provide accurate results. This shows the necessity of a direct study on excitation in the presence of sensor noise, which is inherently described by the signal to noise ratio.

CHAPTER 6

CONCLUSIONS

6.1 Summary

An investigation of vehicle longitudinal dynamics in simulation and experimental tests has been presented. A vehicle model was developed and validated for studying longitudinal vehicle dynamics and the losses therein. The vehicle dynamics model was used to studying the effects and magnitudes of the various losses with in the moving vehicle with the intention of quantifying the energy losses and therefore fuel economy effects. Estimation techniques were used on the vehicle models in a unique test bed that involved performing estimation in a non-typical environment. A sensitivity analysis was performed in simulation showing the effects various sensor noise statistics have on estimation accuracy. A heavy truck test bed was instrumented and data was used for performing estimation results. Long term test longitudinal force data was also analyzed for evaluating road load around a test track to deduce the losses involved with the asphalt sections.

The following paragraphs summarize the information provided in the chapters of this thesis. Chapter 2 presented a simple vehicle model that is widely used to describe the longitudinal vehicle motion on forces on the vehicle. The model was simulated with

results showing vehicle behavior and performance. The individual losses were simulated for their magnitudes on losses and in depth discussions of each are given.

Chapter 3 presented a more advanced derivation of longitudinal vehicle dynamics that includes inertial effects of the driveline. More advanced simulations were performed, which included acceleration, deceleration, and constant speed driving in varying parameters as would be expected and the NCAT test track. Sensor modeling is also presented and used in the vehicle simulations to produce results to mimics those that would be measured in a real world test.

Using the models and simulations developed in Chapter 3, Chapter 4 gave a background on parameter estimation techniques using least squares, and presents models for estimating the major vehicle parameters involved in longitudinal vehicle dynamics. These estimation models were used with the results from simulating various vehicle maneuvers to perform parameter estimates in simulation. The simulated sensor outputs were used to perform parameter estimates and a sensitivity analysis was performed to see the effects of sensor noise on estimation accuracy.

Chapter 5 then described the vehicle test facility and shows real world tests on the work shown in the previous chapters. Road grade around the track and its influences discussed in previous chapters is backed up with real world measurements. An alternative estimation technique utilizing a Kalman Filter is presented and applied to verify the accuracy of the load measurement available from the vehicle on board electronics. Estimation is then performed on various experiments and the results show the feasibility of identifying mass and difficulty distinguishing the various longitudinal losses. Test data

is also analyzed for road load behavior for the direct comparison of road load to asphalt section, or track position.

6.2 Recommendations for Future Work

Ultimately, the work in this thesis should be extended to include vehicle estimation results in test environments other than that of the test track. As shown in Chapter 4, the amount of data and the quality of data has a very large effect on the estimation algorithms' performance. Having access to more high quality data will improve the quality of the results presented in this thesis.

System excitation, or the magnitude of dynamic excitation, is also essential to providing accurate estimation results. This effect is amplified by the inclusion of sensor process and measurement noise. Direct studies on system excitation will yield more comprehensive sensitivity to noise analysis. This will add more dimensions to understating the estimation algorithms performance.

Much work has been done on correlating asphalt roughness to fuel economy effects [duPlessis, 1990; Bester, 1984; Descornet, 1990]. However, this work is somewhat limited in the amount of surfaces tested, and doesn't always have a means to validate the measurements taken. The NCAT test facility is an excellent resource for continuing the work started in this thesis. However, some simple recommendations can be made for improving the existing test bed. Because road grade has such a large effect on the longitudinal loading of the vehicle, a GPS system capable of very accurate vertical measurements should be used to estimate the road grade. This could be inserted into more

advanced estimation schemes that will allow the varying rolling resistance estimates to be performed. Higher accuracy GPS will also be capable of providing more accurate acceleration measurements and position for averaging data over a test section.

To fully understand and simulate fuel economy benefits, a more accurate engine map should also be considered. This can be done by measuring various engine parameters while driving under significant excitation. A fuel consumption map can be generated using measurements of brake mean effective pressure (fuel flow as a function of output), engine load, and engine rpm. This allows the individual engine's characteristics to be analyzed as part of the complex vehicle system and true fuel efficiency benefits estimated. Understanding the engine control system also involves characterizing the vehicle's cruise controller. It is important to understand its control behavior as this will effect fuel use outside of road loading. Appendix C shows a sample cruise control and the effect it can have on the vehicle.

Another option for continuing the research is the construction of a dedicated rolling resistance test rig. Typically rolling resistance measurements are made using a towed implement with a force measuring device. The current estimation schemes could be adapted to estimate rolling resistance in a fully instrumented test rig that could be towed around the track on a regular basis. This device could also be made to measure the rod irregularities directly, and therefore provide a direct rolling resistance versus surface quality measurement.

REFERENCES

[1] Anderson, R., and Bevly, D.M., *Estimation of Slip Angles using a Model Based Estimator and GPS*, Proceedings of the American Control Conference, 2004, pp. 2122-2127.

[2] Ardalan, V, Anna Stefanopoulou, Huei Peng, *Recursive Least Squares with Forgetting for Online Estimation of Vehicle Mass and Road Grade: Theory and Experiments*, Vehicle System Dynamics, Jan 16, 2003.

[3] Bae, H.S., and Gerdes, J.C., *Parameter Estimation and Command Modification for Longitudinal Control of Heavy Vehicles*, AVEC 2000, Ann Arbor, Michigan, August 2000.

[4] Bae, H.S., Ryu, J., and Gerdes, J.C., *Road Grade and Vehicle Parameter Estimation for Longitudinal Control Using GPS*, IEE ITS 2001, Oakland CA, August 2001.

[5] Bester, C.J., "Effect of Pavement Type and Condition on the Fuel Consumption of Vehicles," *Transportation Research Record 1000*, National Research Council, Washington D.C., 1984, pp.28-32.

[6] Bevly, D.M., Gerdes, J. C., Wilson, C., and Zhang, G., *The Use of GPS Based Velocity Measurements for Improved Vehicle State Estimation*, Proceedings of the American Control Conference, 2000, pp. 2538-2542.

[7] Bevly, D. M., Ryu, J., Sheridan, R., Gerdes, J. C, "Integrating INS Sensors with GPS Velocity Measurements for Continuous Estimation of Vehicle Side-Slip and Tire Cornering Stiffness," Proceedings of the 2001 American Control Conference, Vol.1, June 2001, pp.25-30.

[8] Demoz, G.E., "Design and Performance Analysis of a Low-Cost Aided Dead Reckoning Navigator." A Dissertation submitted to the Department of Aeronautics and Astronautics and the committee on graduate studies of Stanford University, Stanford University 2003.

[9] DeRaad, L.W., "The Influence of Road Surface Texture on Tire Rolling Resistance," SAE Paper No. 780257, 1978.

[10] Descornet, G., "Road-Surface Influence on Tire Rolling Resistance," *Surface Characteristics of Roadways: International Research and Technologies*, American Society for Testing and Materials, Philadelphia, 1990, pp. 401-415.

[11] Dixon, J. C., "Tires, Suspension and Handling" Society of Automotive Engineers. Warrendale, PA. ISBN: 1-56091-831-4, 1996.

[12] duPlessis, H.W., Visser, A.T., and Curtayne, P.C., "Fuel Consumption of Vehicles as Affected by Road-Surface Characteristics," *Surface Characteristics of Roadways: International Research and Technologies*, American Society for Testing and Materials, Philadelphia, 1990, pp. 480-496.

[13] EIA, "2004 Annual Energy Review," 2004, The Energy Information Administration: U.S. Dept of Energy, http://www.eia.doe.gov/emeu/aer/.

[14] Flenniken, W.S. IV., "Characterization of Various IMU Error Sources and the Effect on Navigation Performance," Proceedings of The Institute of Navigation's GNSS Meeting, Long Beach, CA, September 2005.

[15] Gillespie, T. D. 1992. "*Fundamentals of Vehicle Dynamics*." Society of Automotive Engineers. Warrendale, PA. ISBN: 1-56091-199-9.

[16] Glemming, D.A., Bowers, P.A., "Tire Testing for Rolling Resistance and Fuel Economy," SAE Paper No. 750457, 1975.

[17] Grover, P.S., Bordelon, S.H., "New Parameters for Comparing Tire Rolling Resistance," SAE Paper No. 1999-01-0787, 1999.

[18] Knight, R.E., "Correlation of Truck Tire Rolling Resistance as Derived From Fuel Economy and Laboratory Tests," SAE Paper No. 821266, 1982.

[19] Knight, R.E., "Tire Parameter Effects on Truck Fuel Economy," SAE Paper No. 791043, 1979.

[20] LaClair, T.J., "Rolling Resistance," *The Pneumatic Tire*, National Highway Traffic Safety Administration, Washington D.C., 2005, pp. 475-532.

[21] LaClair, T.J., Truemner, R., "Modeling of Fuel Consumption for Heavy-Duty Trucks and the Impact of Tire Rolling Resistance," SAE Paper No. 2005-01-3550, 2005.

[22] Milliken, D. L. and Milliken, W. F. 1995. *Race Car Vehicle Dynamics*. Society of Automotive Engineers. Warrendale, PA. ISBN: 1-56091-526-9.

[23] Nielsen, L., Sandberg, T., "A New Model For Rolling Resistance of Pneumatic Tires," SAE Paper No. 2002-01-1200, 2002.

[24] Petersen, E., Neuhaus, D., Glabe, K., Koschorek, R., and Reich, T., "Vehicle Stability Control for Trucks and Busses," SAE Paper No. 982782, 1998.

[25] Schuring, D.J., Redfield, J.S., "Effect of Tire Rolling Loss on Fuel Consumption of Trucks," SAE Paper No. 821267, 1982.

[26] Song, T.S, et. Al, "Rolling Resistance of Tires- An Analysis of Heat Generation," SAE Paper No. 980255, 1998.

[27] Stengel, Robert F, Optimal Control and Estimation, Dover Publications, New York, 1994.

[28] Vahidi, A, Stefanopoulou, A., and Peng, H., "Experiments for Online Estimation of Heavy Vehicle's Mass and Time-Varying Road Grade", in Proceedings of ASME World Congress, Washington, D.C, 2003.

[29] Wood, R., and Bauer, S., "Simple and Low-Cost Aerodynamic Drag Reduction Devices for Tractor-Trailer Trucks," SAE Paper No. 2003-01-3377, 2003.

APPENDICES

APPENDIX A

VEHICLE PROPERTIES

A.1 Introduction

Appendix A contains a list and description of the vehicle properties used in the vehicle model developed in Chapter 2 and 3.

A.2 Simulation Vehicle Properties

Table A.1 contains a list and value of the vehicle properties used in this thesis, unless otherwise stated.

Table A.1: Vehicle Parameters		
Description	Value	Units
Total Vehicle Mass	68000	kg
Air Drag Coefficient	0.6	unitless
Rolling Resistance Coefficient (ave.)	0.0058	unitless
Front Area	10.3	m^2
Tire Rolling Radius	0.504	m
Gear Ratios (Low; 1-8)	10.5	unitless
	7.37	
	5.21	
	3.78	
	2.76	
	1.95	
	1.38	
	1.0	
	0.73	
Final Drive Reduction	3.70	unitless
Inertias:		
Engine Inertia	0.35	$kg\text{-}m^2=N\text{-}m\text{-}s^2$
Clutch	0.15	$kg\text{-}m^2$
Transmission (each gear, 1 side)	0.005	$kg\text{-}m^2$
Rear Axle and Input Gear	0.015	$kg\text{-}m^2$
Differential	0.005	$kg\text{-}m^2$
Tire & Wheel	11.1	$kg\text{-}m^2$
Efficiencies:		
Driveline Overall	0.85	unitless
Driveline Each Stage (Transmission, final drive, brake losses, ea.)	0.95	unitless
Engine Torque Approximation	tq = -1.81*10^-3*RPM^4 +1.56*10^-7*RPM^3 -1.217*10^-3*RPM^2 +2.571*RPM	lbf-ft

APPENDIX B

NCAT FACILITY: EXPERIMENTAL SETUP AND DATA ACQUISITION

B.1 Introduction

Appendix B contains information about the National Center for Asphalt Technology, the hardware, and the experimental setup.

B.2 Experimental Setup & Data Acquisition

Using the National Center for Asphalt Technology's test track and the Freightliner vehicles as a test bed, instrumentation was setup to do real world estimations and fuel economy studies.

For the data collection, a PC/104 computer based data acquisition system was developed. This small form factor computer provides a robust solution to on-board data acquisition. The computer is housed in an extruded aluminum case that serves to isolate the computer hardware from harsh environments, while allowing quick access to computer functions and connections. The operating system used is real-time Unix based QNX, primarily chosen for its stability, low memory and processing requirements, and real-time functionality. Software was written using C++ to interface and data log the various sensors in the system, shown in Figure B.1.

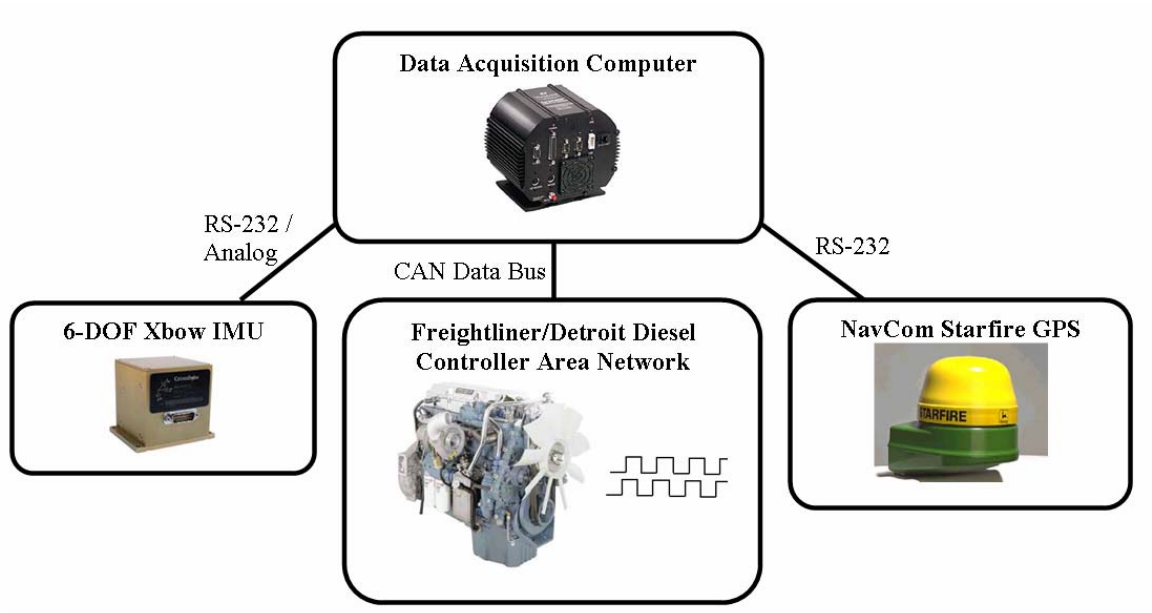

Figure B.1. Data Acquisition Layout

Sensors include a 6 DOF inertial measurement unit, “Starfire” GPS, and CAN data from the Freightliner’s engine computer. The PC, corresponding hardware, and inertial sensors were mounted in the vehicle’s cab under the passenger seat, as shown in Figure B.2.

Figure B.2. Data Acquisition and Sensors Inside Vehicle Cab

The NavComm manufactured Starfire GPS unit was mounted by attaching a bracket to the vehicle structure just rear of the cab out of necessity for adequate satellite view. This placed the receiver high enough to clear obstructions and placed the unit on the vehicle’s centerline as shown in Figure B.3.

Figure B.3. NCAT Test Truck with Starfire GPS Unit Indicated

To solve issues of powering the complete data acquisition unit, without draining the trucks battery when the truck is not running, a unique switching solid state power management device was used. All the sensors are powered directly from switched (key) power on the vehicle, but the computer needed to stay on at all times.

A power management device, made up of rectifier diodes, is used to switch between the backup battery when the engine is off and the vehicle charging system when the engine is on. It is also capable of recharging the separate backup battery using a recharging circuit when the vehicles charging system is functional. This allowed the data

acquisition unit to be left unattended to take data, without requiring any user input or necessity for restarting the computer. The total power system is outlined in Figure B.4.

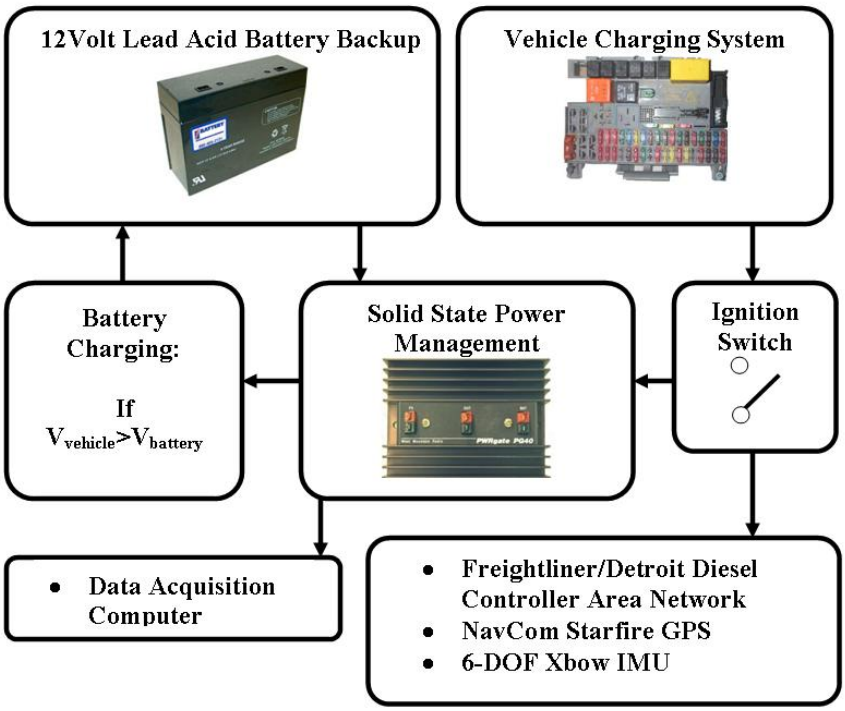

Figure B.4. Data Acquisition Power Schematic

B.3 Hardware Manufacturer Summary

The following table, B.1, outlines the hardware used in data acquisition and the corresponding manufactures.

Table B.1: Hardware Summary	
Device	*Manufacturer*
Bobcat Data Aq Computer w/Enclosure	Versalogic Corp
Computer LCD/keyboard	Earth Computer Technologies, Inc
DC to AC Power Inverter	Sima
Data Aq Computer Power Supply	Tri-M
IMU-400CD	Crossbow Technology Inc.
Starfire GPS Receiver	Navcomm
CAN Controller	Lawicel
12 Volt Lead Acid Battery	PowerSource
Solid State Power Management	West Mountain Radio

B.4 Measurement Capability Summary

The following table shown below outlines the measurement capability of the data acquisition system.

Table B.2: Measurement Summary		
Measurement	Source	Data Format
Longitudinal Acceleration	Xbow IMU	Serial RS-232 Data Packets
Lateral Acceleration	Xbow IMU	Serial RS-232 Data Packets
Vertical Acceleration	Xbow IMU	Serial RS-232 Data Packets
Pitch Rotation Rate	Xbow IMU	Serial RS-232 Data Packets
Yaw Rotation Rate	Xbow IMU	Serial RS-232 Data Packets
Roll Rotation Rate	Xbow IMU	Serial RS-232 Data Packets
Latitude	Starfire GPS	NMEA-RMC Serial GPS Message
Longitude	Starfire GPS	NMEA-RMC Serial GPS Message
Ground Speed	Starfire GPS	NMEA-RMC Serial GPS Message
Heading	Starfire GPS	NMEA-RMC Serial GPS Message
Time	Starfire GPS	NMEA-RMC Serial GPS Message
Electronic Engine Controller 3	Freightliner Engine Computer	SAEJ1939 CAN Specification: Parameter Group Number 61247
Electronic Engine Controller 2	Freightliner Engine Computer	SAEJ1939 CAN Specification: Parameter Group Number 61443
Electronic Engine Controller 1	Freightliner Engine Computer	SAEJ1939 CAN Specification: Parameter Group Number 61444
Cruise Control/Vehicle Speed	Freightliner Engine Computer	SAEJ1939 CAN Specification: Parameter Group Number 65265
Fuel Economy	Freightliner Engine Computer	SAEJ1939 CAN Specification: Parameter Group Number 65266

The information in Table B.3 shown below represents the measurements contained in the data packets logged in this research. The Society of Automotive Engineers publishes and maintains the SAE J1939, Truck and Bus Control and Communications Network Standards Manual. This manual describes the controller area

network (CAN) protocol used in many heavy vehicle systems and provides a standard format and communications protocol for the manufactures if the choose to utilize them. On the Freightliner trucks at the NCAT facility the CAN protocol has been unlocked and made available to us for this research. Within the SAE specification are different Parameter Group Numbers (PGNs) which describe the data packets being sent and received and are functionally organized. Not all available PGNs on the vehicle were used but the following data shown below outlines the PGNs which were used in this research.

Table B.3: SAEJ1939 Measurement Summary		
Parameter Group Number	Name	Data Available
65247	Electronic Engine Controller 3	Nominal Friction % Torque
		Engine's Desired Operating Speed
61443	Electronic Engine Controller 2	Selected Gear
		Actual Gear Ratio
		Current Gear
		Transmission Requested Range
		Transmission Current Range
61444	Electronic Engine Controller 1	Driver's Demand Engine % Torque
		Actual Engine % Torque
		Engine Speed
65265	Cruise Control/Vehicle Speed	Wheel based Vehicle Speed
		Cruise Control Set Speed
65266	Fuel Economy	Fuel Rate
		Instantaneous Fuel Economy
		Average Fuel Economy
		Throttle Position

APPENDIX C

GPS&INS Heavy Truck Cruise Control

C.1 Introduction

Appendix C contains a model derivation and simulation of a state-space vehicle velocity (cruise) controller. This has applications to the Freightliner National Center for Asphalt Technology Trucks because they travel the track under the action of the Freightliner cruise control system. It has been shown previously in this thesis that is important to understand the behavior of the control system and how it effects fuel consumption.

This appendix investigates a cruise control that uses GPS and inertial sensors as the inputs instead of the traditional wheel speed sensors. The system to be controlled is the trucks longitudinal dynamics while rolling over asphalts of varying rolling resistance.

C.2 Cruise Control Model and Simulation

Typical cruise control systems are fairly simple in that their only input is usually a wheel speed sensor. Their control variable is throttle position up to certain limits, usually utilizing a proportional-integral-derivative controller. This simulation however, will use a state feedback control. Longitudinal load variations from surface variations, turns scrubbing off speed, and bank angle on the track, necessitate cruise control to vary the throttle (or the engine control unit's engine load calculation in this case, due to the diesel engines lack of engine air flow throttle mechanisms). A GPS unit's velocity measurement and longitudinal acceleration are the inputs. Combining the sensors creates an essentially cleaner, faster, and more accurate input to control the longitudinal dynamics.

The system dynamics for this simulation are described as follows:

$$\sum F = F_{Drive} - F_{Rolling\ \mathrm{Re}sis\tan ce} - F_{AirDrag} = m\ddot{x} \qquad \text{C.1}$$

where:

F_{Drive} =Drive force provided by engine

$F_{Rolling\ \mathrm{Re}sis\tan ce}$ = Rolling resistance force

$F_{AirDrag}$ = Force due to air drag

m = Vehicle mass

$\ddot{x}$ = Longitudinal Acceleration

It is generally assumed that air drag is related to velocity squared via an air drag coefficient, labeled as follows in Equation C.2.

$$F_{AirDrag} = C_1 V^2 \tag{C.2}$$

Rolling resistance is related to mass with a linear coefficient as shown in Equation C.3.

$$F_{Rolling\ \mathrm{Re}sis\tan ce} = C_2 m g_c \tag{C.3}$$

This simplifies the assumed model to:

$$F_{Drive} - C_2 m g_c - C_1 V^2 = m\ddot{x} \tag{C.4}$$

Note that this system includes nonlinear dynamics. In order to put this plant into state space format we'll have to linearize about some reference point. This is also necessary to calculate the state feedback control gains. In the case of our cruise control system we'll linearize about the target velocity and F_{Drive}. This assumes prior knowledge of the rolling resistance and air drag coefficients as shown below:

$$C_1 = 2 \tag{C.5}$$

$$C_2 = 0.01 \tag{C.6}$$

Which results in:

$$\ddot{x} = \frac{F_d}{M} - 0.01 g_c - \frac{2V^2}{M} \tag{C.7}$$

Using the Jacobian to linearize Equation C.7:

$$\dot{x} = f(x,u) \qquad \text{C.7}$$
$$A = \nabla_x f\Big|_{\frac{xlin}{ulin}}$$
$$B = \nabla_u f\Big|_{\frac{xlin}{ulin}}$$

Looking at u indicated in Equation C.7 at steady state $\ddot{x} = \dot{V} = 0$:

$$\therefore 0 = \frac{F_d}{M} - 0.01g_c - \frac{2V^2}{M} \qquad \text{C.8}$$
$$u_{s.s.} = 2x_{ss}{}^2 + 0.01gM$$
$$\therefore u_{ref} = 2x_{ref}{}^2 + 0.01gM$$

Taking:

$$f = \frac{u}{M} - \frac{2x^2}{M} - 0.01g \qquad \text{C.9}$$

Results in:

$$A = \frac{-4x_{ref}}{M} \qquad \text{C.10}$$
$$B = \frac{1}{M}$$

Arranging the plant into state space format results in the following:

$$\dot{x} = Ax + Bu \qquad \text{C.11}$$
$$y = Cx + Du$$
$$where:$$
$$\dot{x} = \frac{-4V}{M}V + \frac{1}{M}F_d$$
$$y = V$$

Therefore our plant matrices are:

$$A = \left[\frac{-4V_{ref}}{M} \right] \qquad \text{C.12}$$

$$B = \left[\frac{1}{M} \right]$$

$$C = [1]$$

$$D = 0$$

$$where:$$

$$V_{ref} = 45mph$$

Using the Matlab "place" command, the system poles can be placed to be however fast we like. The state-space control poles were placed such that the system had a response resembling the longitudinal dynamics of a ground vehicle (settling time of 10 seconds) and a limit was put on the Fdrive command to a value of force equating to 0.5g's of longitudinal acceleration. Also, to make the system more accurate, the plant model in the simulation is that of the second order system, where the linearized system was only used to pick the feedback gains. The following is the block diagram for the simple state feedback cruise control with noise added to the system output.

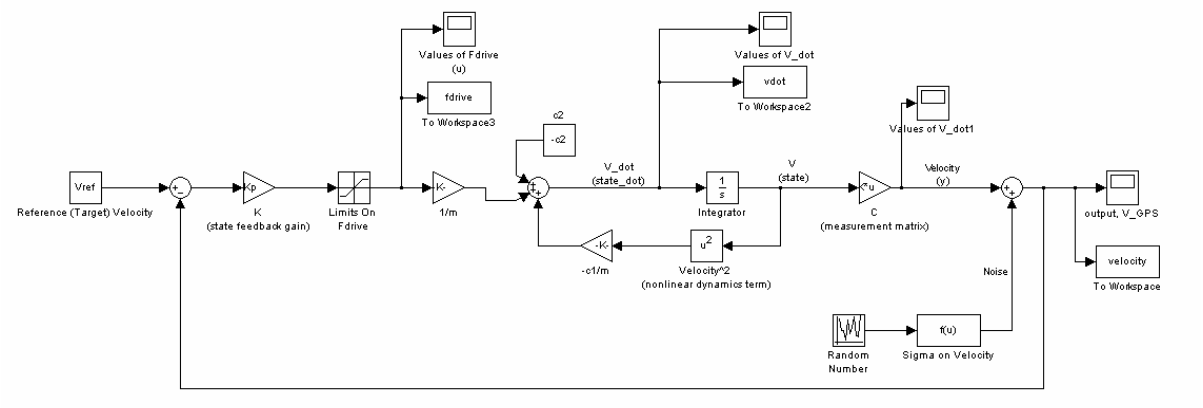

Figure C.1. Block Diagram of State Feedback Cruise Control

The next step is to add an observer to the system, which will allow the use of both GPS and a longitudinal accelerometer to estimate a cleaner velocity to serve as the input to the controller. The typical form a state space controller and estimator is as follows in Figure C.2.

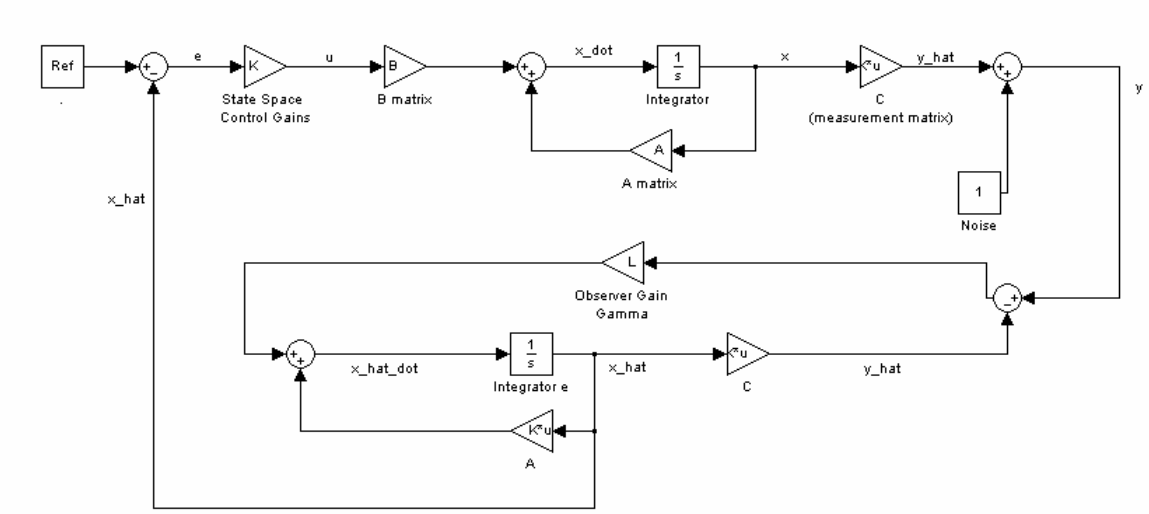

Figure C.2. Block Diagram of Typical State Space Controller and Estimator

For the system studied in this thesis, the truck plant and estimator plant are different and therefore the standard estimator model will not function, as the state matrix varies between the two. The first option is to create two separate systems, a plant and estimator and feed the estimator output to the input of the truck plant. However, this can be simplified to the following system, which will be used for the GPS/INS cruise control.

For the estimator:

$$\dot{x} = Ax + Bu \qquad \text{C.13}$$
$$y = Cx + Du$$
$$where:$$
$$\dot{x} = \begin{bmatrix} 0 & -1 \\ 0 & 0 \end{bmatrix} \begin{bmatrix} V \\ b_{ax} \end{bmatrix} + \begin{bmatrix} 1 \\ 0 \end{bmatrix} \begin{bmatrix} a_x \end{bmatrix}$$
$$y = \begin{bmatrix} 1 & 0 \end{bmatrix} \begin{bmatrix} V \\ b_{ax} \end{bmatrix}$$

With the following system matrices:

$$A = \begin{bmatrix} 0 & -1 \\ 0 & 0 \end{bmatrix} \qquad \text{C.14}$$
$$B = \begin{bmatrix} 1 \\ 0 \end{bmatrix}$$
$$C = \begin{bmatrix} 1 & 0 \end{bmatrix}$$
$$D = 0$$

The estimator gains are found similarly to the state feedback gains with the matlab pole placement function, but settle time is chosen to be about 10 times faster than that of the plant. The estimator above is essentially taking an acceleration input, subtracting the accelerometer bias and integrating to add a correction to the GPS velocity measurement. Both the accelerometer and velocity have random noise added to them, with specs obtained from sensor data sheets. The accelerometer also has a constant turn on bias modeled. The system block diagram is shown in Figure C.3.

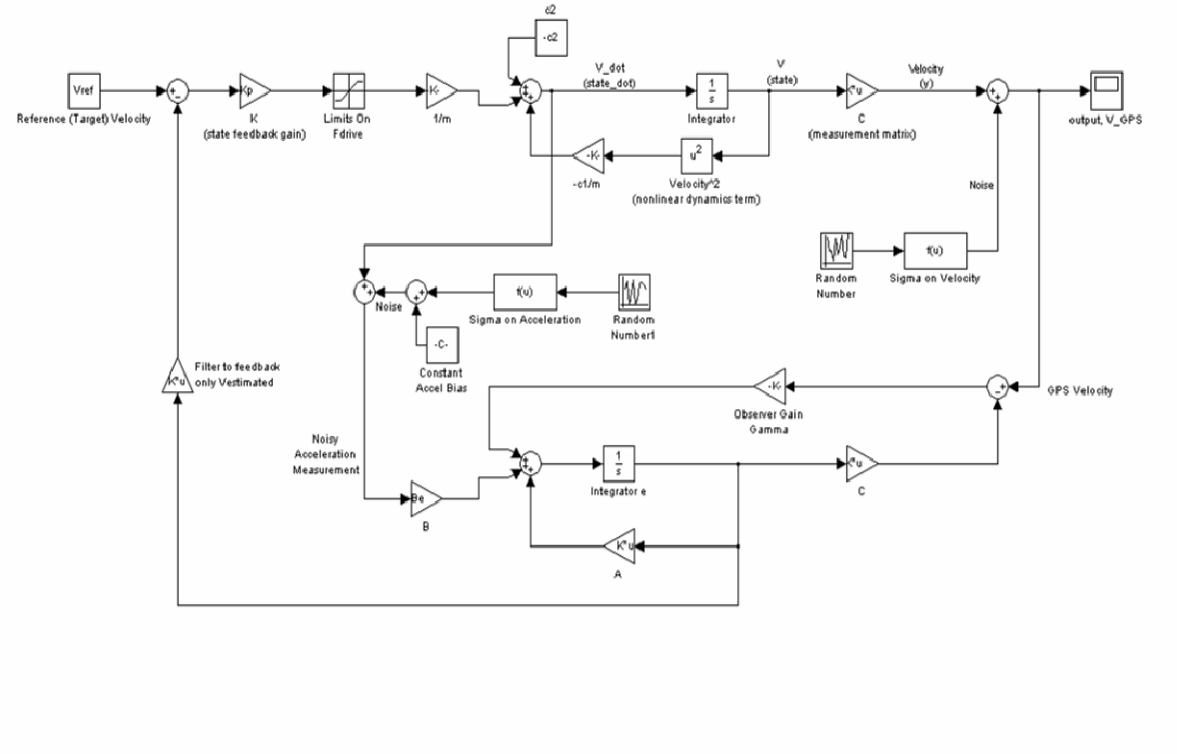

Figure C.3. Block Diagram of State Space Controller and Estimator

Simulations were run to verify the performance of the cruise controller and to assure that the estimator was providing some measurement benefits and removing the sensor bias.

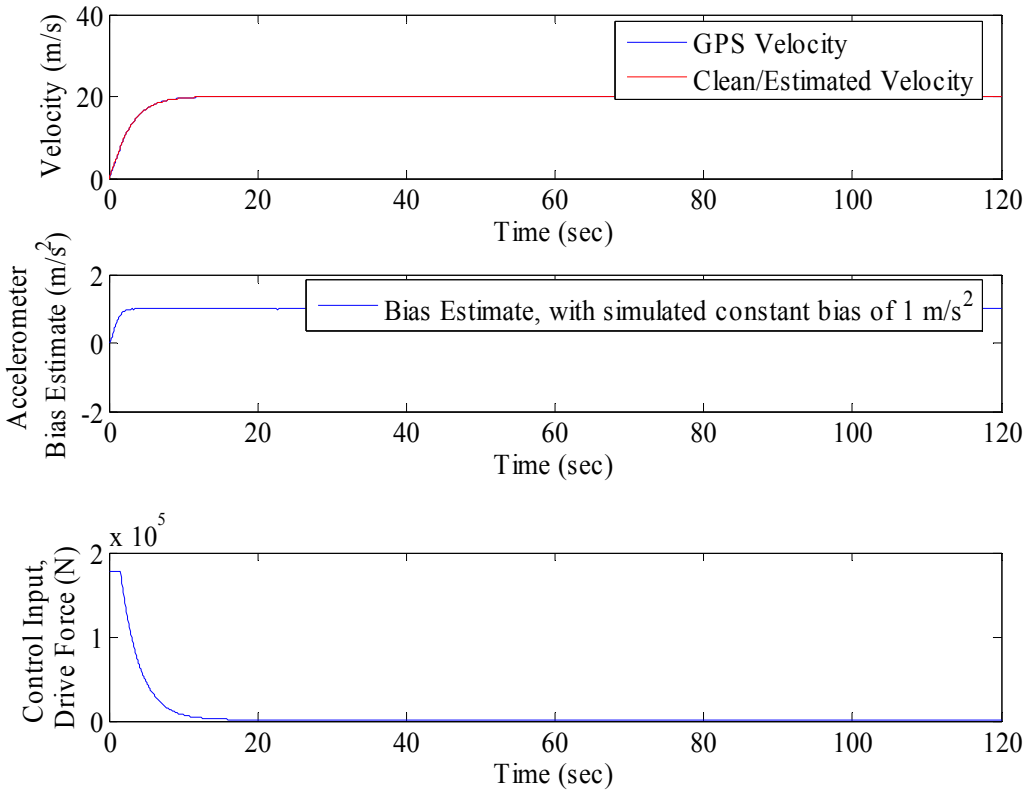

Figure C.4. State Space Controller and Estimator Results

The controller also seems to be giving very good response with no overshoot and zero steady state error, discounting the noise. The following plots provide a closer look at the raw velocity measurement and the estimated velocity.

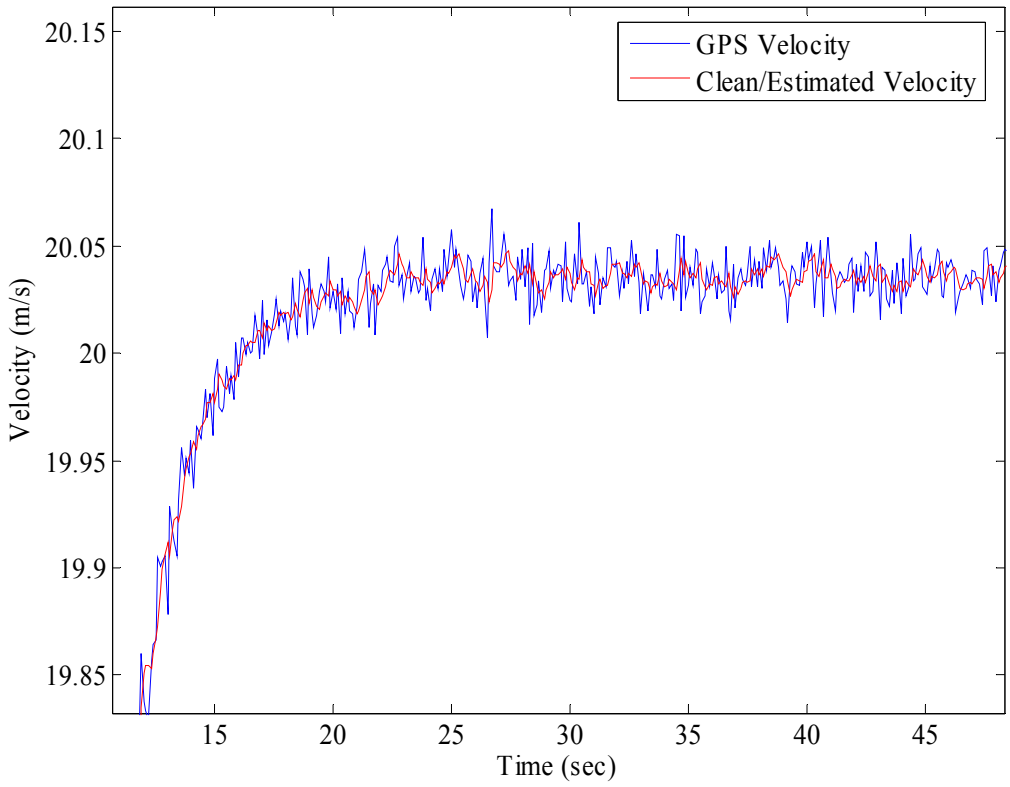

Figure C.5. State Space Estimator Velocity Results

Next, random rolling resistance variation was added to the system. This will serve as a disturbance much like the NCAT trucks experience on their test track as they pass over various asphalts and small slope changes. The technique for this was essentially generating different random calculations of rolling resistance that each lasted for 20 seconds. The system block diagram is in the following figure.

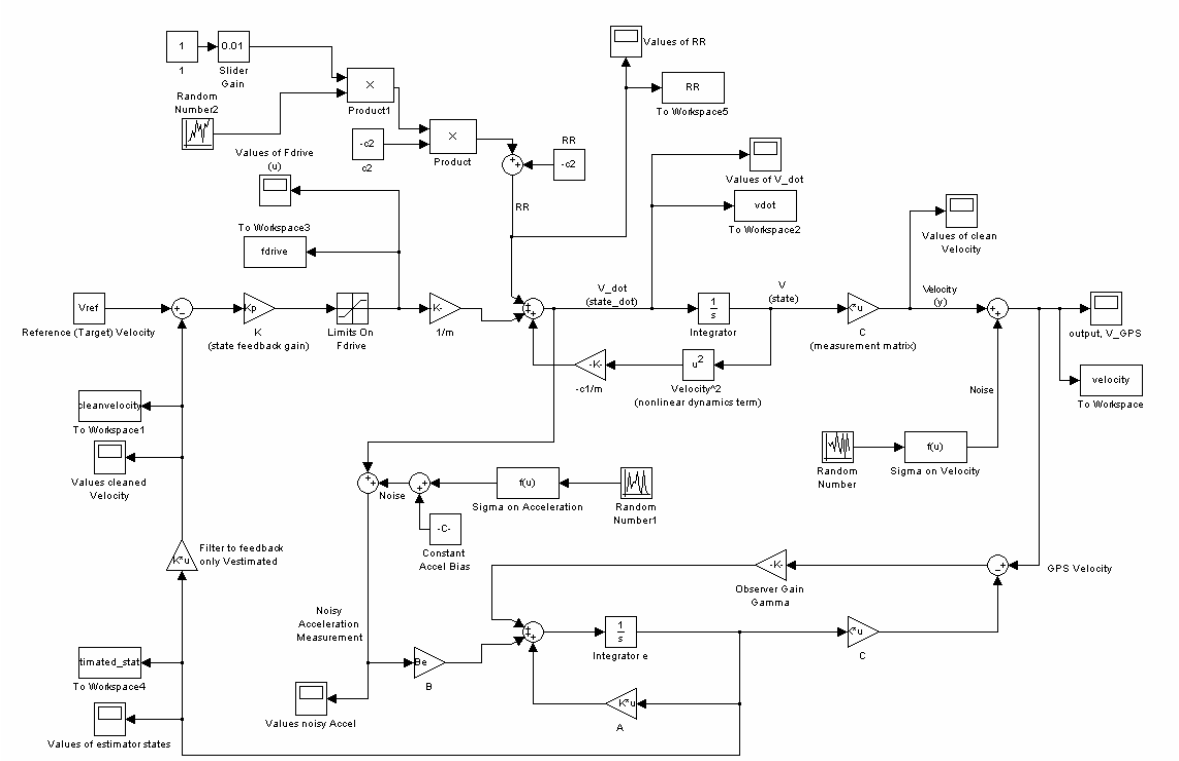

Figure C.6. Block Diagram of State Space Controller and Estimator with Rolling Resistance Disturbance

Figure C.7 shows a simulation of very small changes in rolling resistance and the velocity response.

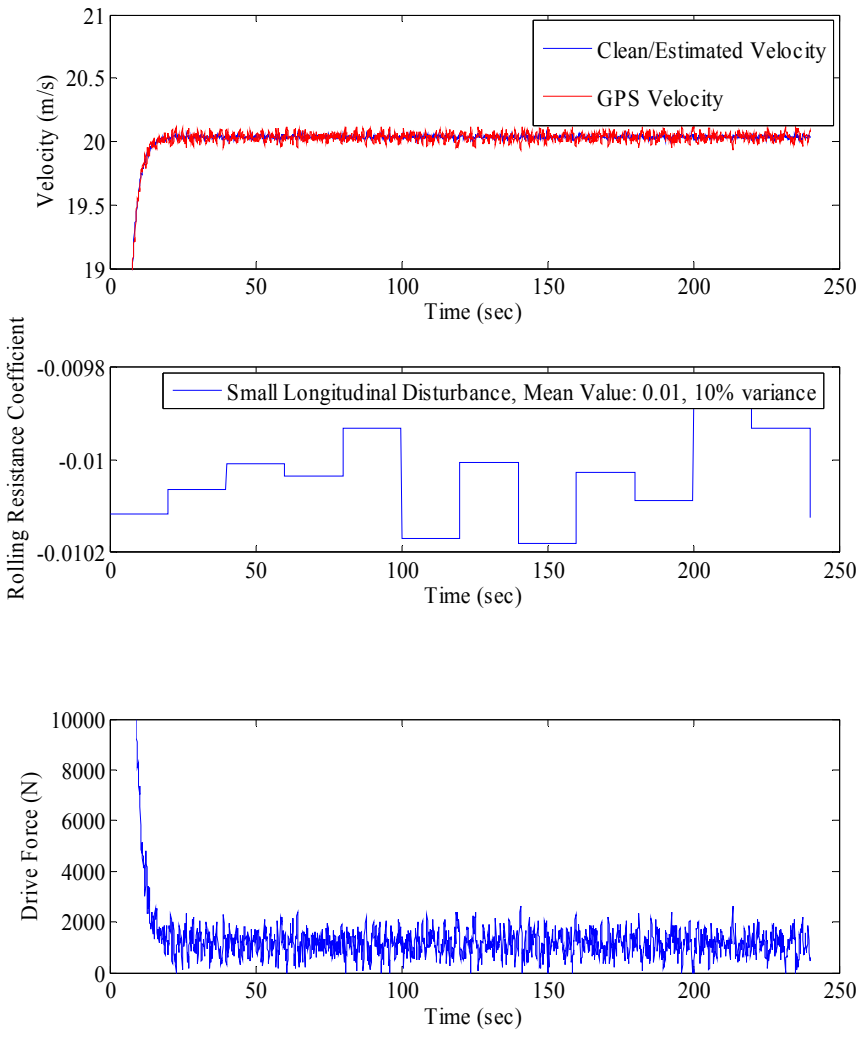

Figure C.7. State Space Controller and Estimator Results with Small Rolling Resistance Disturbance

Figure C.8 shows a much larger disturbance in the rolling resistance parameter. This causes the controller to command larger force variations to try to maintain the target speed. It's also interesting to note, that due to the large variance of rolling resistance coefficients, some actually went to positive values, indicating that the loss was actually a gain, or a force propelling the vehicle. An example would be a down-hill situation. In this case, the controller obeyed its limits, commanding zero drive force.

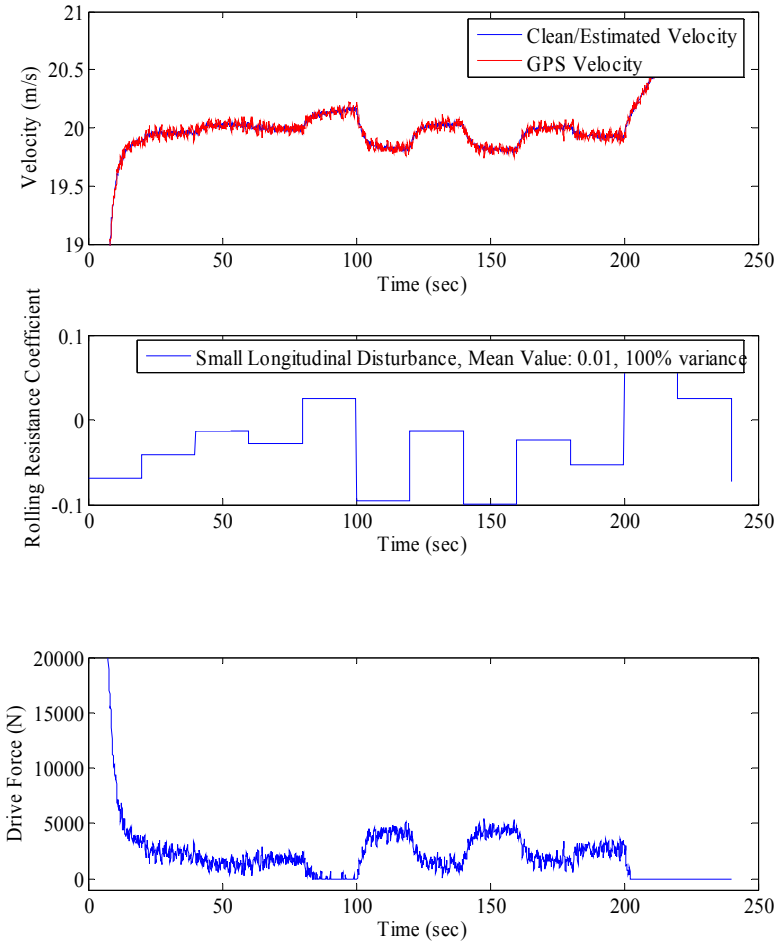

Figure C.8. State Space Controller and Estimator Results with Large Rolling Resistance Disturbance

This cruise control is an interesting study on the state feed back/state space control techniques and gives the opportunity to use sensor fusion in a common application. The controller/estimator implemented performs very well. The controller tracked disturbances well within the realm of vehicle longitudinal dynamics. The linearization to design the feedback gains didn't seem to have any measurable effect on the controller's performance. The estimator improved the GPS reading as well as quickly

estimated out the accelerometer bias, within the time frame of what's necessary upon initializing a cruise control.

There exists opportunities to verify the drive force commands and estimated velocity measurements accuracy on the trucks to make this cruise control's behavior match that of the real trucks to further other research. It is important to understand the controller properties and behaviors if looking at the vehicle dynamics. Certain under and overshoot of the controller may skew results for fuel economy studies.